The Dissertation Committee for Kwanoh Kim Certifies that this is the approved version of the following dissertation:

Innovative Design, Assembling and Actuation of Arrays of Nanoelectromechanical System (NEMS) Devices Using Nanoscale Building Blocks

Committee:

Donglei Fan, Supervisor

David L. Bourell

Ray Chen

Arumugam Manthiram

Charles Buddie Mullins

Innovative Design, Assembling and Actuation of Arrays of Nanoelectromechanical System (NEMS) Devices Using Nanoscale Building Blocks

by

Kwanoh Kim, B.S.E.; M.S.E.

Dissertation

Presented to the Faculty of the Graduate School of

The University of Texas at Austin

in Partial Fulfillment

of the Requirements

for the Degree of

Doctor of Philosophy

The University of Texas at Austin

May 2015

Dedication

I dedicate this dissertation to my beloved wife, Hae Yeon Lee,
my parents, Jungoh Kim and Myunsook Son, and my brother, Hyunje Kim
for their constant support and unconditional love.

Acknowledgements

Foremost, I wish to express my sincere gratitude and appreciation to my supervisor Dr. Donglei Fan. The guidance, mentorship, inspiration, and support she has provided throughout the Ph.D. program have made my graduate experience productive and motivating. Above all, she, as a scientist and researcher I admire, has been a great role model for me. It has truly been an honor to be one of her first Ph.D. students.

I would like to express great thanks to my graduate advisory committee: Dr. David L. Bourell, Dr. Arumugam Manthiram, Dr. C. Buddie Mullins, and Dr. Ray Chen for sharing their valuable time to serve on my dissertation committee.

I would also like to thank my colleagues in Nanomaterial Innovation Lab: Xiaobin Xu, Chao Liu, Jianhe Guo, Ki-pyo Hong, Jing Ning, Wesker Lei, and Weigu Li, for their helpful discussions and advice.

The infinite love and confidence my parents and brother have shown me cannot be described by simple words of thanks. It was their presence that helped me to reach my goals with patience. And, I would like to thank my wife, who has been with me all these years. It would have never been possible to complete my graduate study without her considerate support and encouragement.

Lastly, I would like to thank God for His extended love and guidance for His unfaithful humble servant.

Innovative Design, Assembling and Actuation of Arrays of Nanoelectromechanical System (NEMS) Devices Using Nanoscale Building Blocks

Kwanoh Kim, Ph.D.

The University of Texas at Austin, 2015

Supervisor: Donglei Fan

Rotary nanomotors, a type of nanoelectromechanical system (NEMS) device that converts electric energy into mechanical motions, are critical for advancing NEMS technology in various fields but have been difficult to obtain using traditional techniques. As a consequence, it is highly desirable to investigate new mechanisms to develop large arrays of rotary NEMS devices with high efficiency, small size, and reliable performance at a low cost.

In this dissertation, we report innovative designs and mechanisms for assembling and actuating arrays of rotary NEMS devices based on the electric tweezers and unique magnetic interactions among components. NEMS oscillators and motors were assembled from nanoscale building blocks including nanowires working as rotors, patterned nanomagnets as bearings, and quadrupole electrodes as stators. Multiple devices could be assembled in an ordered array and rotated either between two designated angles reciprocally or the full cycles continuously with controlled angle, speed (over 18,000 rpm) and chirality. Their fundamental electric, magnetic, and mechanical interactions were investigated, which provided an understanding of nanoscale dynamics critical to designing and actuating various metallic NEMS devices. We could reduce the size of the

device with all its characteristic dimensions below 1 micron and continuously rotate a nanomotor for up to 15 hours, which is equivalent to more than 240,000 cycles in total. As an application, NEMS devices were used for controlled biochemical release and demonstrated the releasing rate of biochemical from the devices could be precisely tuned by mechanical rotation.

Various magnetic configurations were purposely designed and successfully implemented, which resulted in distinct rotation behaviors including repeatable wobbling and self-rolling in addition to in-plane rotation. With the understandings of these rotation characteristics, high-performance micromotors have been rationally designed and successfully achieved, where the micromotors rotate at uniform speeds and position at desired angles, resembling step motors.

Bioinspired micromotors comprised of three-dimensional porous diatom frustule rotors and patterned micromagnets were assembled and rotated in a microfluidic channel. Simulation results showed that they could stir and agitate liquid in a microchannel more efficiently than simple one-dimensional nanoentities and would be promising for microfluidic actuators.

The innovations reported here, including concept, design, fabrication, actuation mechanisms, and applications, are expected to inspire various research areas including NEMS, nanorobotics, biomedical applications, microfluidics and lab-on-a-chip architectures.

Table of Contents

List of Tables

List of Figures

Chapter 1: Introduction

1.1. Man-Made Nanomachines

Nanomachines are nanoscale mechanical devices that can convert optical, electromagnetic, acoustic, or chemical energy into controlled mechanical motions. Since Richard Feynman introduced the concept of miniaturized machines that could be swallowed and work like a surgeon to repair inadequately functioning organs in human body in his groundbreaking talk "There's plenty of room at the bottom" in 1950s,[1] nanomachines have been long desired but extremely difficult to realize. In the recent decades, owing to the vigorous progress in nanoscience and technology, remarkable advances have been made in the development and application of nanoscale mechanical devices, such as nanomotors, nanoocillators, and nano-grippers. The success in creating highly controllable nanomachines represents a critical step towards the future intelligent nanorobots and nanofactories.

Nanomachines can be categorized into three types according to the nature of materials that they are made from: first, the molecular machines, such as deoxyribonucleic acid (DNA),[2-4] ribonucleic acid (RNA),[5] and stereo organic molecules.[6] They are generally several to tens of nanometers in size and can be made of either naturally existing biomolecules or synthetic biochemicals.[3,4,7] Upon receiving external stimulus, the molecular machines can perform various mechanical motions. However, it is extremely difficult to synchronize the motions of large numbers of molecules for practical applications due to their 3-D random positioning and thermally induced Brownian motion.[8] The second type of nanomachines is the bio-inorganic hybrid nanomachine, where the bio-components of this kind of nanomechanical device, such as

rotary proteins[9] and cardiomyocytes,[10] serve as powering engines that drive the inorganic components of the devices and generate reproducible motions. The size of these devices ranges from a few micrometers to a few millimeters. The third type is made from inorganic nanoparticles of hundreds of nanometers to a few micrometers in size. They can be driven to transport, rotate, roll, drill, and wobble in a highly controllable fashion by the stimulation of physical fields[11-22] or chemical reactions.[23-29] Although bionanomachines such as molecular motors are highly efficient and commonly found in nature, their applications are limited. It is arduous to control their motion. The lifetimes of such nanomachines are usually short. Besides, they only work in biocompatible fuel solutions, which can support specific reactions to power the motions of the biomolecular components.[30] Man-made inorganic nanomachines can be the solution to the aforementioned issues and have attracted immerse research interest recently.

1.2. NANOMACHINES FABRICATED BY TOP-DOWN LITHOGRAPHY

Traditionally, miniaturized mechanical devices, such as microscale motors,[31-37] resonators,[38] and accelerometers,[39,40] are developed by using top-down lithographical techniques, such as photolithography and micromachining, inherited from microelectronics industry. However, the fabrication of rotary micromotors through the traditional lithographical technique required hundreds of processing steps due to the complex design of the devices with integrated components of rotors, bearings, hubs, and stators.[34-37] Because of the arduous fabrication processes, only a few of micromotors can be made on a wafer and the lifetimes are from seconds to a few hours.[35,36] The structural complexity also limits the size of the motors ranging from millimeters to hundreds of

micrometers.[34-36,41] It is extremely difficult to further reduce the size of motors to a few micrometers to sub-micrometers.

The top-down fabrication approach is advantageous in realizing micro/nanomachines with sophisticated structures, multiple functionalities, and precisely controlled dimensions. However, in most cases, the fabrication procedure is complex, which requires advanced instruments and operation skills of personnel. It is also arduous to make mechanical devices to the truly nanoscale regions via this approach.

1.3. Bottom-up Assembled Micro/Nanomachines from Inorganic Nanoscale Building Blocks

Recently, assembling miniaturized electromechanical devices using nanoentities as components, or building blocks, has attracted attention from researchers. Nanoentities have obvious advantages for use in building NEMS devices. Their small footprint and unique chemical, mechanical, electromagnetic properties can significantly downsize devices and effectively improve performance. Besides, owing to the recent progress in nanotechnology and nanomaterial synthesis processes, nanoentities with desired chemical, mechanical, and electromagnetic properties as well as dimensions and geometry can be easily synthesized at low cost[42] through well-established fabrication processes including template-assisted electrodeposition,[24,43,44] catalytic assisted chemical vapor deposition,[45] and hydrothermal synthesis.[46] Moreover, in general, the bottom-up synthetic approach does not require sophisticated instrumentation and could be scaled up for mass production at low cost. It is highly desirable that nanomachines can be directly assembled from these synthesized nanoparticles. However, due to the lack of methods for efficient nanomanipulation, assembling, and actuation, in the earlier stage, nanomachines were mostly obtained by the top-down fabrication approach. Recently, significant efforts

have been focused on the investigation into innovative mechanisms to assemble and manipulate nanomachines made of nanoscale building blocks.

In the following chapters, different rotary NEMS devices bottom-up assembled from micro/nanoentities will be introduced, including their designs, working mechanisms, and assembling techniques, which are based on the electric tweezers[11,12,47] and the unique magnetic interactions among the components. Their mechanical, electromagnetic, optical, and chemical characteristics were also investigated and will be discussed along with their biomedical and microfluidic applications.

Chapter 2: Precision Assembly and Actuation of Nanowire Oscillators

2.1. INTRODUCTION

Nanotechnology has intrigued the research community for over a decade, not just due to the rich fundamental science when materials are made on the nanoscale, but also due to the high potential of making revolutionary impact on critical technologies.[48] Recently, intensive research efforts have focused on using nanoentities as actuation components for Micro/Nano Electromechanical System (MEMS/NEMS) devices owning to the unique advantages that nanotechnology can provide: (1) the size of the MEMS devices can be significantly shrunk with nanoscale building blocks;[47,49] (2) the unique physical/chemical/electrical properties of nanoparticles can improve the performance of miniaturized mechanical devices.[50,51] Various nanomechanical devices with nanoentities as building blocks have been demonstrated including biochemical delivery nanovehicles,[13] chemical and biological sensors,[52-54] mechanical logic gates,[55] nanooscillators,[12,56] nanoswitches,[57,58] mechanical nanorelays,[59] and nanoactuators.[60,61] However, the application of NEMS has been greatly hindered by the arduous nature of top-down lithographical fabrication methods which require advanced skills and elaborate instrumentation, as well as the limited strategies to actuate NEMS.

In this chapter, we report innovative mechanisms for precision assembly and actuation of arrays of nanowire NEMS devices that can synchronously toggle between two designated positions for over 4000 cycles. The assembling and actuation mechanisms are based on unique magnetic interactions between nanoentities with perpendicular magnetic anisotropy (PMA) and electric-tweezer manipulation—our recent invention. These new mechanisms may be applied to efficient bottom-up assembly of various

NEMS devices such as nanomechanical switches for turning on/off nanocircuits and nanoresonators for biochemical sensors and radio-frequency communication and are significant improvements in terms of efficiency and facility over the commonly used.

Even though substantial advances have been made in the synthesis and characterization of nanowires, it is dreadful to use existing bottom-up assembly technique including contact printing,[62] bubble-blown assembling,[63] flow assisted assembling,[64,65] dielectrophoresis,[66-73] or magnetic manipulation,[74-76] to accurately assemble, align, or actuate functional NEMS at desirable locations without substantial post-processing.

Here, we leverage an unique magnetic interaction between nanowires and nanomagnets with perpendicular anisotropy as well as electric-tweezer technique[12,47] to achieve precisely controlled assembly and actuation of nanowire oscillators. Multisegment Au/Ni/Au nanowires have been transported and assembled on prepatterned arrays of nanomagnets by the electric tweezers— a recently invented nanomanipulation technique based on combined electrophoretic and dielectrophoretic forces.[12,47] The magnetic attraction between the Ni segments in the nanowires and Ni layers inside the nanomagnets plays two roles: first, it precisely anchors nanowires on the patterned magnets (also called magnetic nanoanchors); second it aligns the nanowires in the initialization magnetic treatment direction (idle direction). By applying an AC electric field (**E**-field) along another designated direction, the orientation of nanowires can be toggled between the idle direction and actuation direction of the AC **E**-field. We have observed that ordered arrays of nanowires can synchronously toggle between the two positions on the magnetic nanoanchors for 4000 times, demonstrating the robustness of the assembling and operation mechanism.

2.2. METHODS

The rotary beams made of three-segment Au/Ni/Au nanowires were fabricated by electrodeposition in anodized aluminum oxide (AAO) template as reported elsewhere.[12,43] In brief, a 500-nm-thick Cu film was evaporated on the backside of an AAO template (nominal pore diameter of 300 nm) and used as a working electrode. Au, Ni, and Au segments were sequentially electroplated into the nanopores. The length of each segment was controlled by the amount of charges passing through the circuit. As a result, arrays of nanowires with 1-μm-long Ni segments sandwiched between two 4.5-μm-long Au segments were synthesized. After the template was dissolved in a 2 M sodium hydroxide (NaOH) solution, the nanowires were dispersed and centrifuged for at least twice in de-ionized (DI) water before resuspended in DI water. The backscattered Scanning Electron Microscopic (SEM) image shows the "bamboo" like three-segment nanowires in Fig. 2.1(a). Due to the large aspect ratio of the Ni segment, the magnetic easy axis of each Au/Ni/Au nanowire is along the long axis.[77]

The electric tweezers can controllably manipulate nanowires suspended in liquids with a fine degree of control. The working principles of the electric tweezers have been described in details elsewhere.[12,47] With the electric tweezers, nanoentities can be compelled to transport and align independently in the directions of the DC and AC **E**-field, respectively. The transport speed, depending on the surface charge on the nanowires and DC **E**-field strength, can be as high as 80 μm/s.[78] By applying the **E**-fields in both the X and Y directions with suitable duration, nanowires can be manipulated along prescribed trajectories in two dimensions with a precision of at least 150 nm.

2.3. RESULTS AND DISCUSSION

By combining the magnetic assembly using site specifically patterned nanomagnets and the aforediscussed electric-tweezer manipulation, we have successfully assembled and integrated nanowires [Fig. 2.1(a)] with predefined structures and patterns. A schematic diagram of the device is shown in Fig. 2.1(b). The critical design is an array of nanoanchors with tri-layer Cr/Ni/Au films fabricated in the center of a 500-μm-gap quadrupole microelectrode via which **E**-fields can be applied. The tri-layer anchoring nanomagnets consist of Cr (6 nm) for adherence to the substrate, Ni (100 nm) for providing magnetic forces, and Au (100 nm) for tuning the magnitude of the magnetic forces [Fig. 2.1(c)]. The magnetic nanoanchors were made into various geometries such as circles (1 μm in diameter), bars (1×3 μm), and equilateral triangles (2 μm in each side) [Fig. 2.1(c)]. The magnetic state of the anchoring nanomagnets were controlled by demagnetization with a gradually reducing oscillating magnetic field of ±10 kG followed by re-magnetization with a constant magnetic field of 10 kG applied for 5 seconds along desirable angles, i.e., 0°, 45°, and 90°. With the electric tweezers, nanowires can be transported in the center of the quadrupole electrodes along prescribed trajectories, parallel (AC//DC) or perpendicular (AC⊥DC) to the transport orientation. When nanowires were positioned in the vicinity of a nanoanchor, they were swiftly attracted to and assembled atop of the nanoanchors as shown in Fig. 2.1(d). Once attached to a nanoanchor, a nanowire cannot be transported by the **E**-fields any longer due to the magnetic attraction. As a result, an array of nanowire assembly can be achieved.

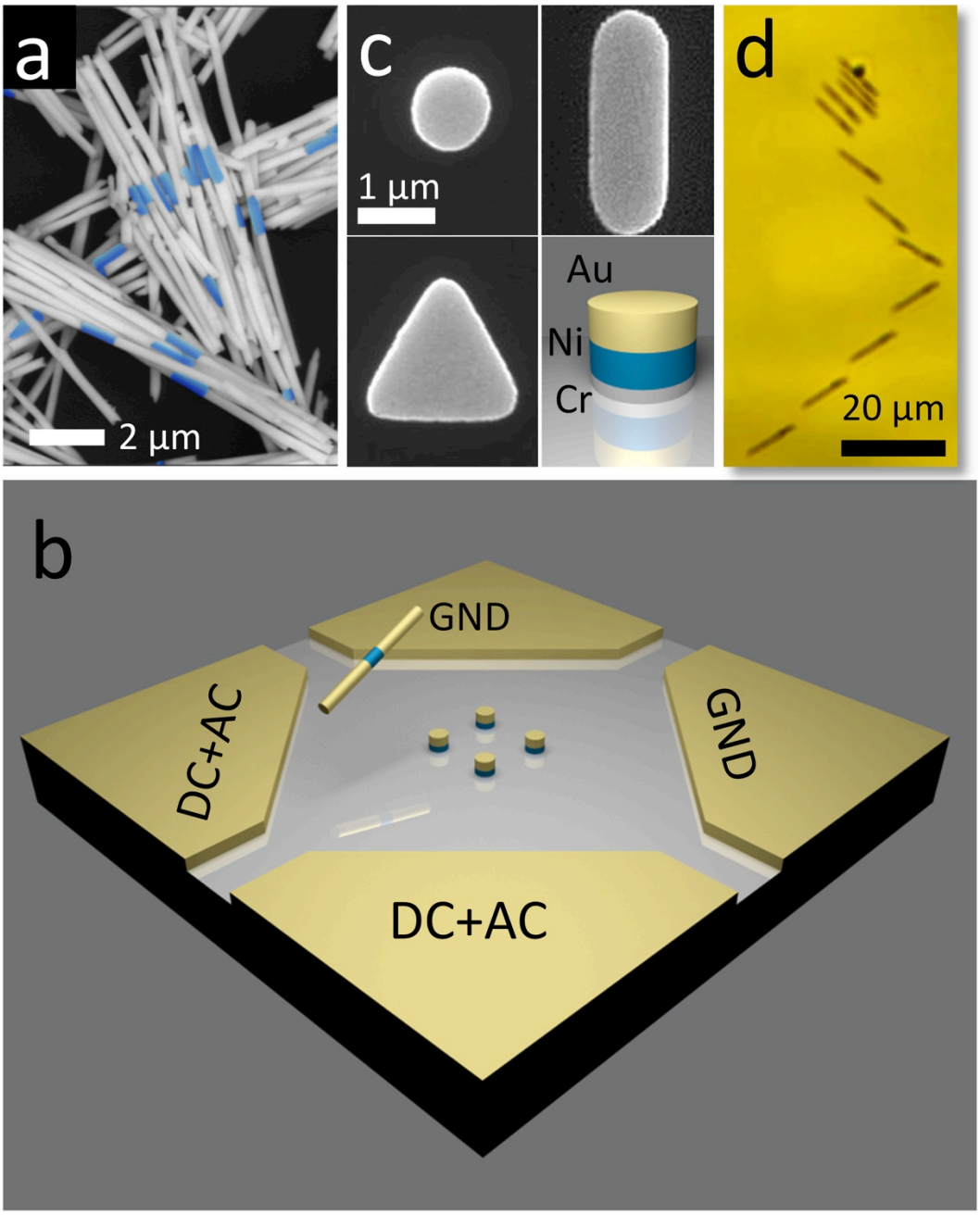

Figure 2.1: (a) Multisegment Au/Ni/Au nanowires with 1-µm Ni segment in green. (b) Schematic diagram of electric-tweezer setup consists of Au quadrupole electrodes with a magnetic nanoanchor array at the center. (c) Structure of a Cr/Ni/Au trilayer magnetic nanoanchor and the Scanning Electron Microscopy (SEM) images of the patterned magnetic nanoanchors in shapes of circles, triangles and rectangles. (d) Overlapped snap shots of a nanowire manipulated by the electric tweezers along prescribed trajectories.

It was also observed that after assembly on the anchors, most of the nanowires aligned in the direction of initial re-magnetization of nanoanchors, because the magnetic torque between the nanowires and nanoanchors caused spontaneous rotation of nanowires to the antiparallel magnetic configuration [Fig. 2.2(a)]. Moreover, regardless how a nanowire approaches a nanoanchor or the geometry of a nanoanchor (circle, bar, or triangle), a nanowire always aligns in the initial re-magnetization direction as shown in Fig. 2.2(b). Such a phenomenon cannot be easily explained by the properties of commonly used magnetic materials with a fixed direction of in-plane anisotropy, such as cobalt, iron, or low-rate evaporated nickel. Our investigation shows that the Cr/Ni/Au anchoring nanomagnets have PMA with a small in-plane component that is set along the re-magnetization direction. As a result, the magnetic state of Au/Ni/Cr anchoring nanomagnets is controllable and tunable for nanowire assembly along any direction. Characterization with Vibrating Sampling Microscope (VSM) of the Cr/Ni/Au film before patterning showed that its magnetic anisotropy is perpendicular to the film plane as shown in Fig. 2.3(a). Magnetic Force Microscopy (MFM) images further revealed highly ordered magnetic domain structures in Ni nanopatterns [Fig. 2.2(c)] after demagnetization in a defined direction. The alternating dark and bright stripes with 120 – 140 nm periodicity are the magnetic domains with up/down polarities. The line pattern aligns with the direction of in-plane demagnetization field [Fig. 2.2(c)]. This phenomenon is the same as in continuous Ni film. MFM images of continuous Ni film show maze-type domains after perpendicular demagnetization [Fig. 2.3(b)] and parallel line domain structures after in-plane demagnetization field [Fig. 2.3(c)]. Magneto-restriction due to the high interfacial stresses between Ni and the substrate causes PMA for Ni thin films (evaporated at a high rate >1 Å/s).[79] Different from other magnetic materials with PMA, the PMA of Ni consists of not only a large perpendicular

component but also a small in-plane component [Fig. 2.2(d)], which has been detected by VSM measurement [Fig. 2.3(a)]. The small in-plane magnetic component interacts with Au/Ni/Au nanowire and causes spontaneous alignment of nanowires on the nanoanchor. As shown in Fig. 2.4(e), most of the nanowires on nanoanchors align with the magnetic domain direction, regardless of the geometry of the nanomagnet patterns. It indicates that although the perpendicular polarities of each domain are alternating, which result in an essentially zero net-force on nanowires, the in-plane components have a net moment along one direction, which can attract and align nanowires. Here, via the nanowire assembly technique, we directly proved the existence of an in-plane magnetic component in the PMA system of evaporated Ni film, which is often arduous to be determined by using traditional magnetic characterization techniques such as VSM and AFM.[80]

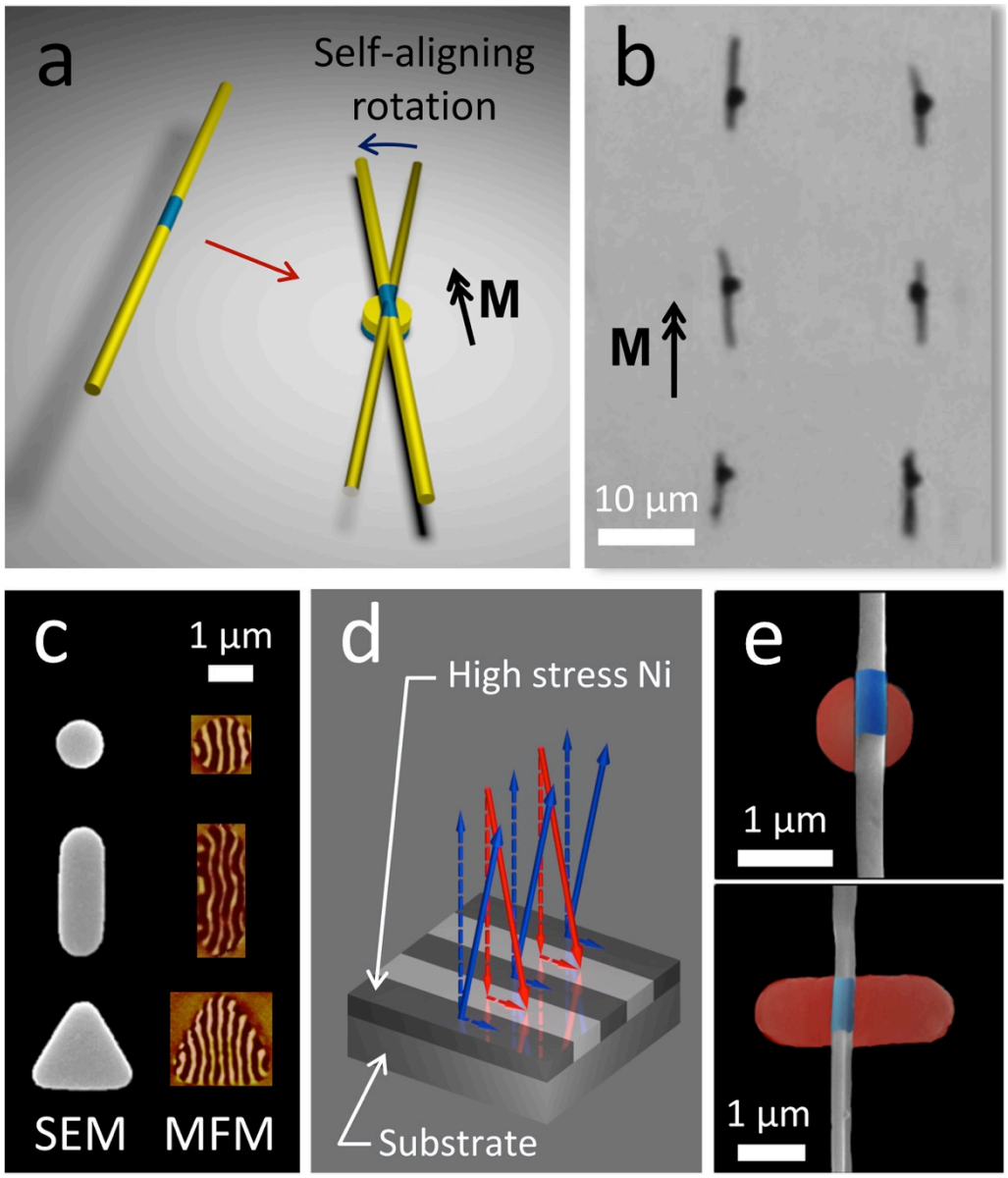

Figure 2.2: (a) Schematics of self-aligning nanowires. A nanowire approaching at a random angle rotates to the position antiparallel to the magnetization of a magnetic nanoanchor in the direction of M. (b) Au/Ni/Au nanowires assembled on an array of triangle magnetic nanoanchors and aligned parallel to the magnetic orientation. (c) SEM and Magnetic Force Microscopy (MFM) images of magnetic domain structures of magnetic nanoanchors made of stressed Ni thin films. (d) The magnetic orientation of such a unique magnetic material is illustrated. (e) SEM images show precision assembly of nanowires on the magnetic anchors, where the edges of the Ni segments (in blue) flush with the edges of magnetic dots (in red).

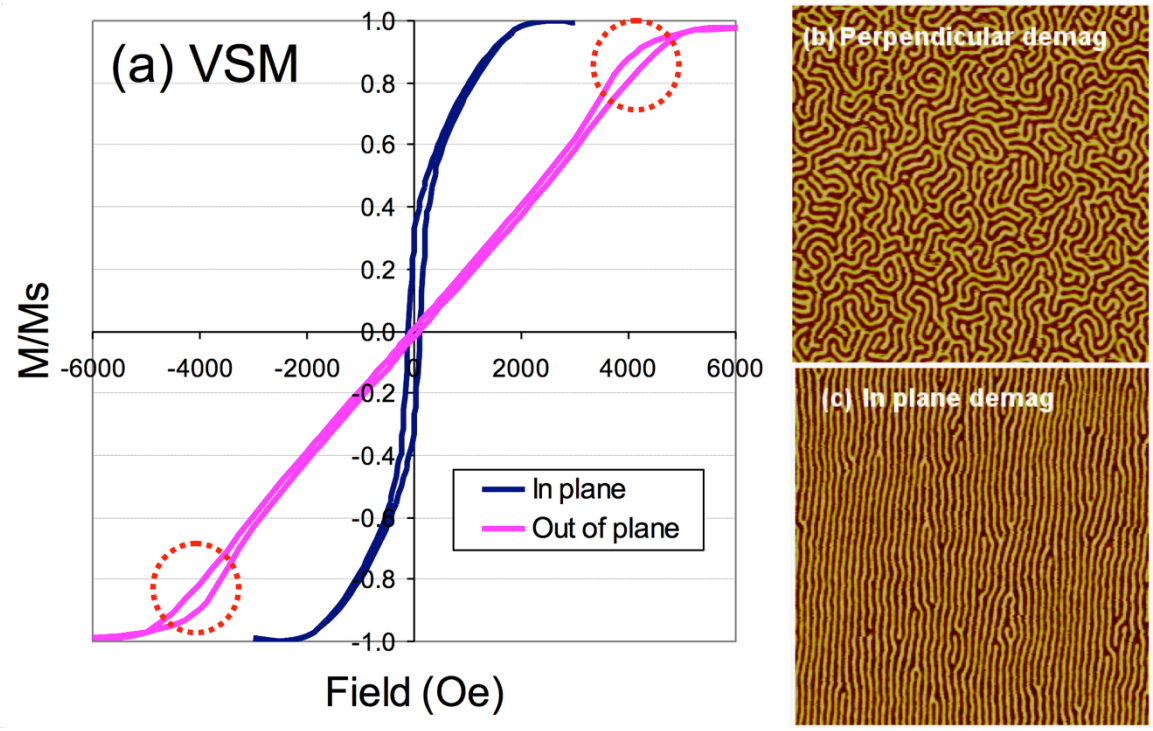

Figure 2.3: (a) VSM magnetic hysteresis loops of 300 nm thick Ni film measured with in-plane and out-of-plane magnetic fields. Red circles remark the tell-tale sign of perpendicular anisotropy because of the formation of maze domain patterns.[79] (b) MFM image of Ni film after perpendicular demagnetization reveals maze-type magnetic domain pattern, and (c) parallel-line domain pattern after in-plane demagnetization. The direction of line domains in (c) is the same as magnetic field direction. The images shown in (b) and (c) are both 10×10 μm^2 in size.

The assembly of nanowires with the PMA nanoanchors is so precise that the edges of the Ni segments in the nanowires are flush with the edges of the magnetic nanoanchors. The accuracy of assembly and alignment can be retained even after water evaporation as shown in Fig. 2.2(e). Moreover, we found that the domain alignment of PMA Ni can be readily altered to arbitrary directions and thus the alignment of nanowires can be tailored. Fig. 2.4(a) – (d) show the optical images of assembled nanowires on disk-shaped and bar-shaped magnetic nanoanchors in 2×2 or 2×3 arrays with the re-magnetizing field applied at 0° (a, b) and 45° (c, d). The majority of the nanowires

oriented according to the re-magnetization direction regardless of the geometry of the nanoanchors. The tunable assembly is achievable via facile reorientation of magnetic domain structures by demagnetization + re-magnetization along any direction as shown by MFM images in Fig. 2.4(e). As a result, by leveraging the PMA of the nanoanchors, we can accurately and tunably assemble nanowire arrays along desired directions.

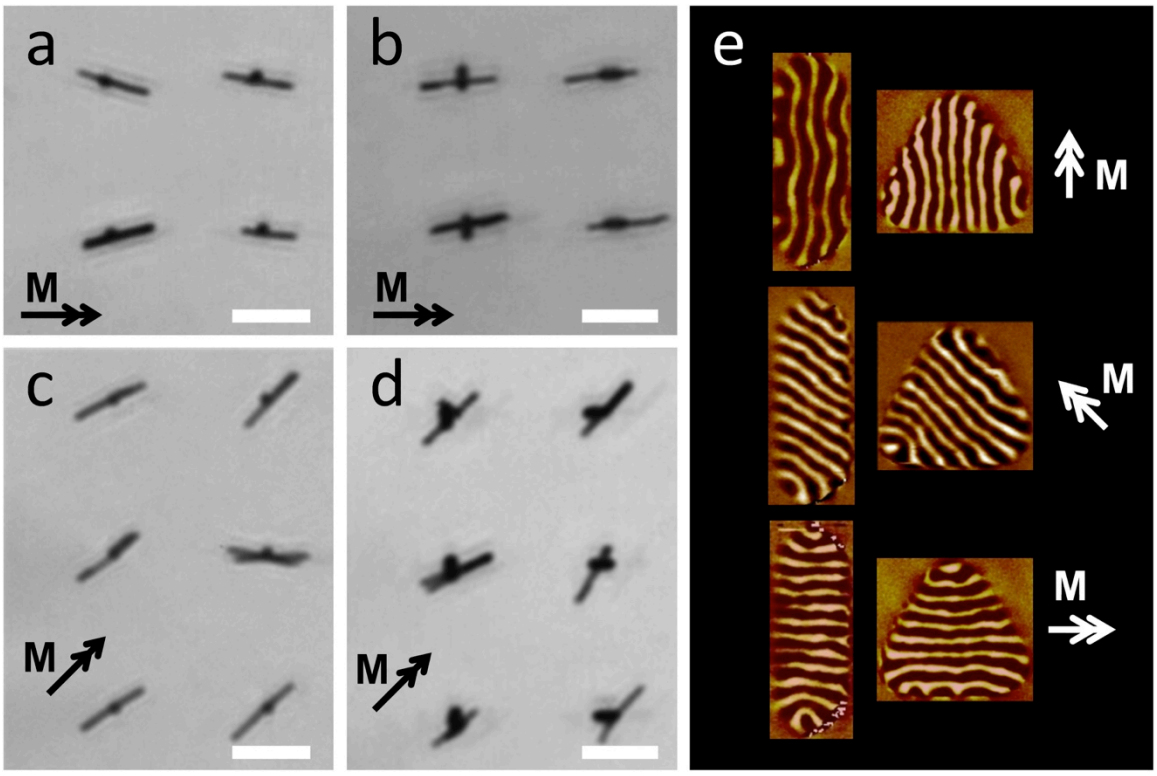

Figure 2.4: (a) – (d) Nanowires assembled and aligned on (a, c) disk and (b, d) bar nanoanchors demagnetized along (a, b) 0° and (c, d) 45° (Scale bars: 10 μm). (e) Domain wall structures of the bar and triangle nanoanchors demagnetized at 0°, 45°, and 90°.

The new nanowire assembly strategy by using combined PMA magnetic interaction and electric-tweezer manipulation has great advantages for bottom-up assembly of nanomechanical devices from nanoscale building blocks. For demonstration

purpose, we assembled and actuated a 2×2 array of nanowire oscillators, where nanowires synchronously rotate between two states: aligned in the magnetization direction (**M**) or aligned in the AC **E**-field direction applied at an angle of 90° or 45° relative to **M** [Fig. 2.5(a) and (b)]. The oscillation is achievable by periodically turning the AC **E**-field on and off, so that the nanowires align to the AC **E**-field when it is on and restore to the magnetic orientation when it is off. The frequency of oscillation can be controlled by the toggling frequency of the AC **E**-field [Fig. 2.5(b)]. The operation of the nanooscillators is robust and precise. We have recorded 4000 cycles of synchronous rotation before the increased friction at the wire-anchor interface finally stopped the rotation of nanowires [Fig. 2.5(c)]. The contact surface of the nanoanchor endures abrasion when a nanowire oscillates on the nanoanchor. The abrasion of the Au spacer layer reduces the distance x between the magnetic layer in the nanoanchor and the magnetic segment of the nanowire. As a result, the magnetic torque τ_M and the friction torque $\tau_{f,M}$ increase, as they are inversely proportional to x^3 and x^4, given by $\tau_M = (\mu_0 m_1 m_2 \sin \Theta)/(4\pi x^3)$ and $\tau_{f,M} = (3\mu\mu_0 m_1 m_2 \cos \Theta)/(4\pi x^4)$, respectively. μ, μ_0, m_1, m_2, and Θ are the coefficient of friction between the nanowire and the nanoanchor, the magnetic constant, the magnetic dipole moments of the nanowire and the nanoanchor, and the angle between the magnetizations of the nanowire and the nanoanchor, respectively. The increment in the torques impedes the motion of nanowire including oscillation amplitudes and speeds under the same external AC **E**-field and this phenomenon ultimately determines the lifetime of the nanowire oscillator. It was found that the oscillation amplitude significantly reduced after 4000 cycles and finally the nanowire was immobilized when the Au layer became too thin and the friction was too high. Currently, we are working on the critical issues of lifetime and frictions in NEMS using innovative lubricants and spacer with much higher hardness.

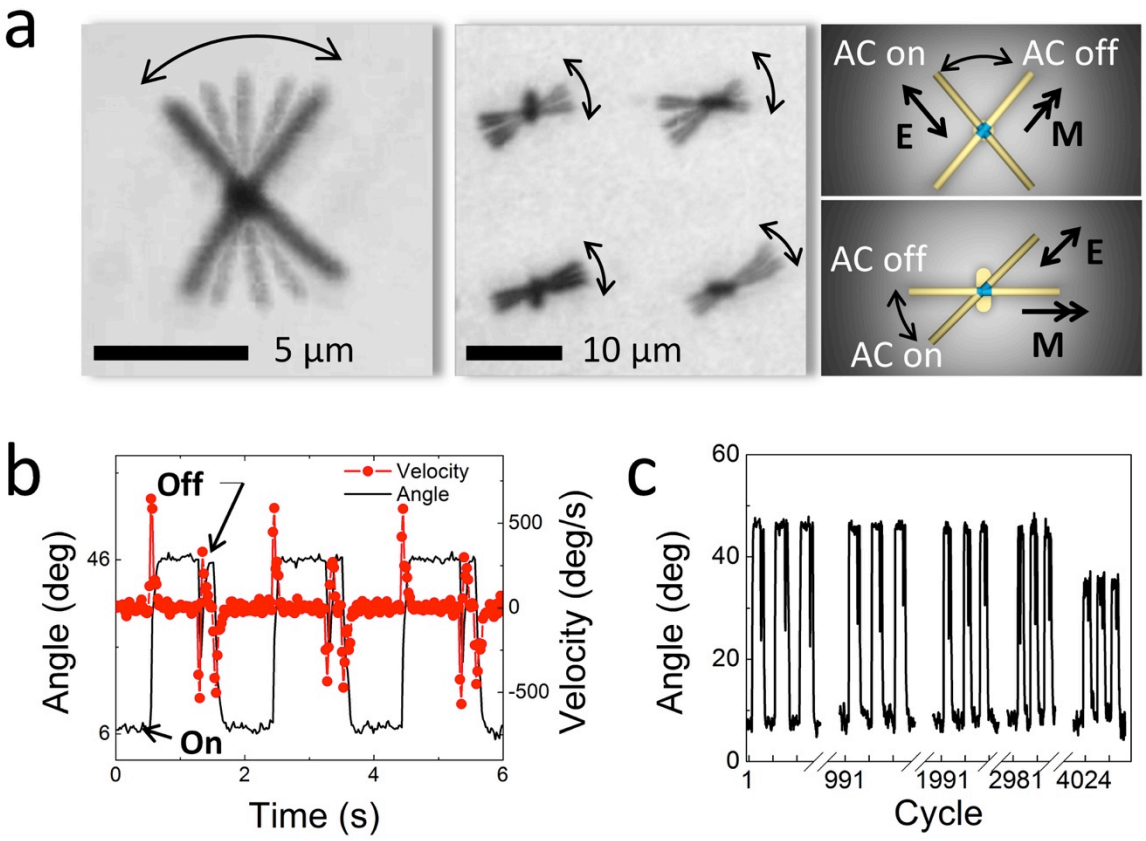

Figure 2.5: (a) Overlapped snapshots and schematic diagrams of oscillating nanowires assembled on a single disk magnetic nanoanchor and a 2×2 array of bar-shaped magnetic anchors. Nanowires rotate between the positions aligning with the external AC **E**-field and aligning with the magnetic orientation of the nanoanchors (M). (b) Angle and angular velocity with respect to time for an oscillating nanowire on a nanoanchor. (c) Robust oscillation of the assembled nanowires for over 4000 cycles.

We have quantitatively calculated the torques exerted on an oscillating nanowire by combining a model and numerical analysis of time dependent frames captured by a CCD camera. Torques on an oscillating nanowire can be expressed as $\tau_\eta + \tau_e + \tau_M + \tau_{e'} + \tau_f = 0$, where τ_η, τ_e, τ_M, $\tau_{e'}$, and τ_f are liquid drag torque, electrical torque due to external AC **E**-field, magnetic torque, electrical torque due to induced electric polarization of magnetic nanoanchors under external AC **E**-field, and frictional torque, respectively. All

the torques are angle dependent, which makes the calculation complex. But through analysis at extreme angles, when nanowires stop rotation due to balance between the electric (τ_e + $\tau_{e'}$) and the magnetic (τ_M) torques, we can readily get typical values of electric/magnetic torques involved in the nano-oscillators knowing that the viscous drag (τ_η) and frictional torque (τ_f) can be approximated as zero. With detailed modeling, the comprehensive values of electric, magnetic, frictional, and viscous torques as functions of angle and velocity can be readily determined as shown in Fig. 2.6.

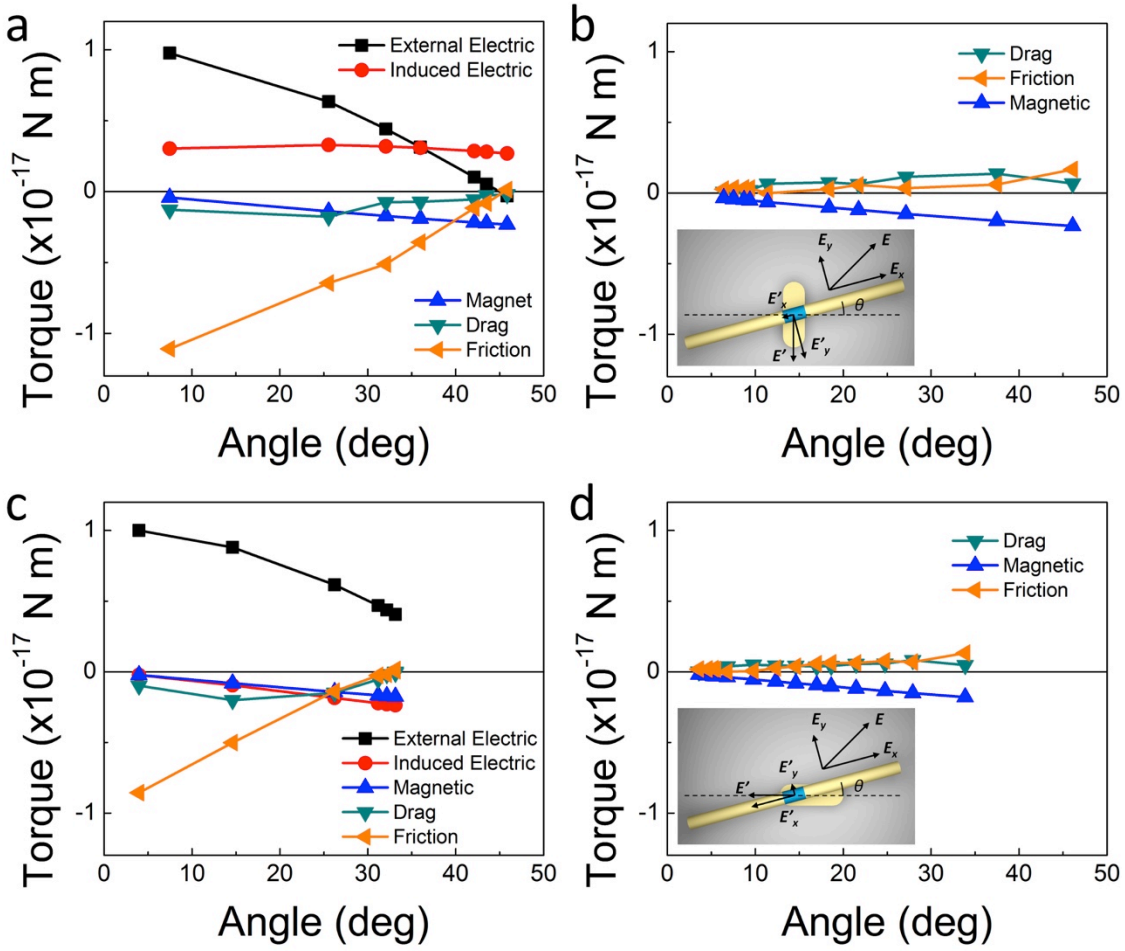

Figure 2.6: Various torques including electric, magnetic, frictional, viscous, and induced electric torques as functions of angle θ [(a), (c)] with and [(b), (d)] without external AC **E**-fields for a rotating nanowire assembled on a bar magnetic anchor, whose geometric long axis is perpendicular [(a), (b)] or parallel [(c), (d)] to their magnetization orientation.

First, the drag torque τ_η = (-1.74×10^{-19}) ω [N m] is estimated as a function of angular velocity ω according to the method proposed by Keshoju, et al., [81]

$$\tau_\eta = \frac{1}{3}\omega\pi\eta l^3 \frac{N^3-N}{N^3\left[\ln\left(\frac{l}{Nr}\right)+0.5\right]} = -1.74\times10^{-19}\omega \quad (2.1)$$

where radius r = 150 nm, length l = 10 μm for the nanowire, η_{water} = 0.89× 10^{-3} Pa, and N = 2.

The electric torque τ_e by external AC **E**-field can be calculated as below:[82]

$$\tau_e = \frac{8\pi l r^2}{3}\varepsilon_m E^2\left(L_y - L_x\right)Re\left[\frac{\left(\underline{\varepsilon}_p-\underline{\varepsilon}_m\right)^2}{[\underline{\varepsilon}_m+(\underline{\varepsilon}_p-\underline{\varepsilon}_m)L_x][\underline{\varepsilon}_m+(\underline{\varepsilon}_p-\underline{\varepsilon}_m)L_y]}\right]\cos 2\theta = B\cos 2\theta \quad (2.2)$$

$\underline{\varepsilon}_m$ and $\underline{\varepsilon}_p$ are the complex permittivities of the medium and nanowire defined as

$$\underline{\varepsilon}_m = \varepsilon_m + \frac{\sigma_m}{j(2\pi f_{AC})} \quad (2.3)$$

$$\underline{\varepsilon}_p = \varepsilon_p + \frac{\sigma_p}{j(2\pi f_{AC})} \quad (2.4)$$

where $j = \sqrt{-1}$, ε_m and ε_p are the permittivities of the medium and nanowire, and f_{AC} is the frequency of the AC **E**-field. L_x and L_y are the depolarization factors in the X and Y directions, known as

$$L_x = \frac{1}{2}l(2r)^2\int_0^\infty \frac{ds}{(s+l^2)\sqrt{(s+l^2)[s+(2r)^2]^2}} \quad (2.5)$$

$$L_y = \frac{1}{2}l(2r)^2\int_0^\infty \frac{ds}{[s+(2r)^2]\sqrt{(s+l^2)[s+(2r)^2]^2}} \quad (2.6)$$

τ_e can be directly obtained from its angular velocity ω since τ_e equals to viscous drag torque τ_η ($\tau_e = \tau_\eta$). [11] As a result, τ_e can be obtained from the drag torque $\tau_\eta = (-1.74\times10^{-19})\ \omega$ [N m]. We plotted the obtained torque τ_e as a function of θ [Fig. 2.7], which fits to $\tau_e = (1.01\times10^{-17})\cos 2\theta$ [N m]. This value is considered to be the same with that of nanowires of the same dimension, material, and fluid medium assembled on nanoanchors.

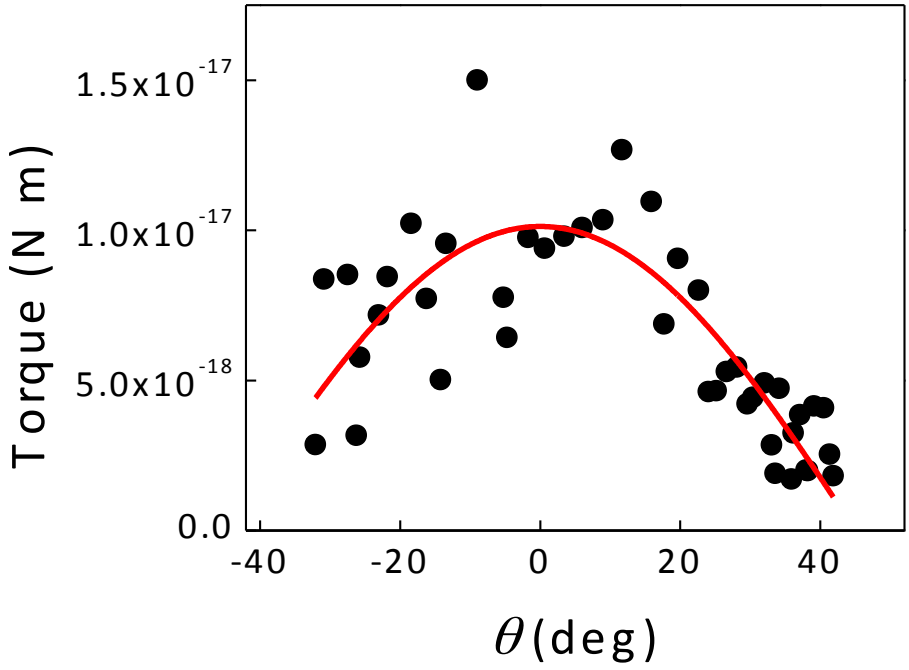

Figure 2.7: Electric torque τ_e exerted on a free rotating nanowire as a function of its angular position θ. The curve-fit to $B\cos 2\theta$ is shown as the red line.

The magnetic torque τ_M is obtained by analyzing the rotation of a nanowire due to the restoring magnetic torque when the external AC **E**-field is turned off. The rotation is governed by only τ_η, τ_M, and τ_f because τ_e and $\tau_{e'}$ are zeros and τ_M is proportional to sin θ.[77] Therefore, we can readily obtain

$$\tau_\eta = \tau_M - \tau_f = d \sin\theta - \tau_f . \tag{2.7}$$

When the angles θ is small, d and τ_f can be approximated as constant. Then, d can be determined from the slope of the τ_η–sin θ curve [Fig. 2.8], which results in τ_M = (-3.24×10^{-18}) sin θ [N m].

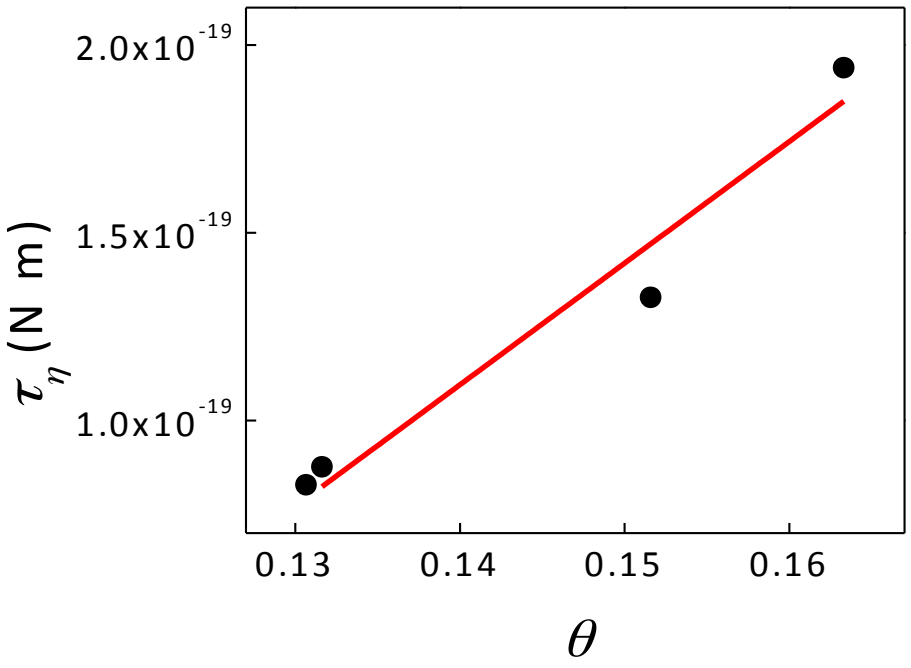

Figure 2.8: τ_η - sin θ curve of a rotating nanowire on a vertical bar magnet when the external AC **E**-field is turned off. The red line indicates the slope of the curve at the small angle.

We note that the bar-shaped magnetic metal anchors also exert electric torques $\tau_{e'}$ on the nanowires due to the **E**-field induced by the polarization of a magnetic metal nanoanchor:[82,83]

$$\boldsymbol{\tau}_{\mathbf{e}'} = \frac{1}{2} Re\left(\underline{\mathbf{p}} \times \underline{\mathbf{E}'}\right) \tag{2.8}$$

where **p** is the complex dipole moment of a nanowire. To understand how the electric torque depends on the angular position of nanowires due to the induced electric polarization of the magnetic nanoanchors, we need to calculate the induced **E**-field **E′** from the nanoanchors**.** To simplify the calculation, we approximate that the bar nanoanchor as a spherical dipole polarized by an external **E**-field. The induced **E**-field **E′** due to the polarization **p′** of the bar nanoanchor is given by[84]

$$\underline{\mathbf{E}'} = \frac{1}{3\varepsilon_0}\underline{\mathbf{p}'} \tag{2.9}$$

Since the induced polarization of the bar nanoanchor is primarily along its long direction x', we denoted it as $p'_{x'}$, which can be approximated as **p′** given by:

$$\underline{\mathbf{p}}' \approx \underline{\mathbf{p}}'_{x'} = 4\pi V_{bar}\varepsilon_m \underline{K}_{x'}\mathbf{E}_{x'} = 4\pi V_{bar}\varepsilon_m \underline{K}_{x'}\mathbf{E}\sin 45° \tag{2.10}$$

where

$$\underline{K}_{x'} = \frac{\underline{\varepsilon}_p - \underline{\varepsilon}_m}{3[\underline{\varepsilon}_m + (\underline{\varepsilon}_p - \underline{\varepsilon}_m)L_{x'}]} \tag{2.11}$$

and

$$L_{x'} = \frac{1}{2}V_{bar}\int_0^\infty \frac{ds}{(s+w^2)\sqrt{(s+w^2)(s+h^2)(s+t^2)}}. \tag{2.12}$$

$\underline{K}_{x'}$ is the complex Clausius-Mossotti factor of the bar nanoanchor, in which the polarization is strongest along x' due to the shape anisotropy, $E_{x'}$ is the external **E**-field

along the long direction of the bar, w, h, t, V_{bar} are the width, height, thickness, and volume of the bar nanoanchor, respectively.

By the same token, we consider that the dipole polarization of a nanowire in the transverse direction $\underline{p}_y$ is weak enough to be ignored. The electric polarization is primarily along the long direction of the nanowire in x-direction. Therefore, from Eq. (2.10), we can obtain:

$$\underline{\mathbf{p}} \approx \underline{\mathbf{p}}_x = 4\pi(2r)^2 l \varepsilon_m \underline{K}_x \mathbf{E} \cos(45° - \theta) \tag{2.13}$$

Where $\underline{K}_x$ is the complex Clausius-Mossotti factor of the nanowire, in which the polarization is primary along the long direction of the nanowire (x).

Take Eq. (2.10) into Eq. (2.9):

$$\underline{\mathbf{E}'} = \frac{4\pi V_{bar}}{3\varepsilon_0} \varepsilon_m \underline{K}_{x'} \mathbf{E} \sin 45° \tag{2.14}$$

Then, the y-component (perpendicular to the long axis of the nanowire) of $\mathbf{E}'$ is

$$\underline{\boldsymbol{E}'}_y = \frac{4\pi V_{bar}}{3\varepsilon_0} \varepsilon_m \underline{K}_{x'} E \sin 45° \sin(90° - \theta) \tag{2.15}$$

Take Eq. (2.15) and Eq. (2.13) into Eq. (2.8), we obtained

$$\tau_{e'} = \frac{1}{2} Re \left\{ \left[4\pi(2r)^2 l \varepsilon_m \underline{K}_x E \cos(45° - \theta) \right] \left[\frac{4\pi V}{3\varepsilon_0} \varepsilon_m \underline{K}_{x'} E \sin 45° \sin(90° - \theta) \right] \right\} \tag{2.16}$$

As a result, $\tau_{e'}$ can be simply expressed as:

$$\tau_{e'} = C\cos(45° - \theta)\cos\theta, \tag{2.17}$$

where

$$C = \frac{1}{2}\mathrm{Re}\left\{\left[4\pi(2r)^2 l\varepsilon_m \underline{K}_x E\right]\left[\frac{4\pi wht}{3\varepsilon_0}\varepsilon_m K_{x'} E\sin 45°\right]\right\}. \tag{2.18}$$

Since the nanowire on the vertical bar nanoanchors (magnetization is along the long direction of the bar) is aligned by the AC **E**-field at 46°, then,

$$\tau_{e'} = -\tau_e - \tau_M, \tag{2.19}$$

$$C\cos(45° - 46°)\cos 46° = -(1.01\times10^{-17})\cos 2(46°) + (3.24\times10^{-18})\sin 46° \tag{2.20}$$

Therefore, we obtained $\tau_{e',vertical}$ = 3.86×10^{-18} cos (45° - θ) cos θ [N m]. Using a similar approach, we have determined the induced electric torque on the horizontal bar anchor [inset of Fig. 2.6(d)]: $\tau_{e',horizontal}$ = (-4.42×10^{-18}) cos (45° - θ) sin θ [N m].

Finally, the frictional torque τ_f is given by:

$$\tau_f = -(\tau_\eta + \tau_e + \tau_M + \tau_{e'}) \tag{2.21}$$

where τ_η, τ_e, τ_M, and $\tau_{e'}$ have been calculated above. The various torques exerted on nanooscillators were plotted as functions of angles in Fig. 2.6 for nanowires rotating on vertical [Fig. 2.6(a) and (b)] or horizontal bar-shaped magnetic anchors [Fig. 2.6(c) and (d)] when the external **E**-field is on [Fig. 2.6(a) and (c)] or off [Fig. 2.6(b) and (d)]. The torques are in the unit of pN μm, and the magnitude of the analyzed torques for

nanowires rotating on horizontal bar anchors agrees very well with those on vertical bar anchors when the **E**-field is either on or off. We note that the frictional torques τ_f have noticeable increment when the AC **E**-field is on [Fig. 2.6(a) and (c)] than when it is off [Fig. 2.6(b) and (d)] in both of the cases of rotating nanowires on a horizontal and a vertical bar. It can be attributed to the increased normal force due to the non-negligible electrostatic attraction between the nanowires and the magnetic anchors under external AC **E**-fields.

Through the analysis of torques involved in the nanooscillators, we quantitatively determined that the induced electrostatic interaction between metallic components in NEMS devices under external AC **E**-field has considerable impact on their mechanical actuation behaviors. The electric torque generated by the induced dipole moment of a magnetic nanoanchor is non-negligible compared to the driving torque of the device — electric torque due to the external AC **E**-field. This is also evidenced by the increased frictional torque due to the strong induced electrostatic interaction between nanowires and nanoanchors when the external AC **E**-field is on. Moreover, the operation angle of the nanooscillator depends on the relative orientation of the nanowires and bar-shaped nanoanchors as shown in the insets of Fig. 2.6(b) and (d). As a result, the important effects of the induced electric torques in metallic NEMS devices have been revealed in this work, which is important to consider in making future bottom-up assembled NEMS devices.

2.4. CONCLUSION

In summary, we have investigated an innovative scheme for precision assembly and actuation of nanowire nanomechanical devices with combined magnetic interactions

and the electric tweezers. We studied how the interaction between the PMA nanomagnet anchors and Ni-embedded nanowires resulted in precision assembly, alignment, and actuation of nanowire NEMS devices. The assembly and actuation mechanisms are facile and robust. An array of nano-oscillators has been constructed and synchronously rotated between two defined angular positions up to 4000 cycles. The various complex torques involved in such a system have been analyzed and show excellent consistence between different rotating devices. The important effects of induced electrostatic torques in metallic NEMS were qualitatively revealed. The new approach of *in situ* fabrication and operation of NEMS devices can replace many mechanical fixation structures (such as screws and hinges), and motion recovery parts (such as springs). This research may inspire facile assembling of various NEMS, such as nanoresonators and nanomechanical relays, which is relevant to biochemical sensing and computation, and impact NEMS and nanoelectronics in large.

Chapter 3: Nanomotors Assembled from Nanoscale Buiiding Blocks

3.1. INTRODUCTION

Nanoelectromechanical System (NEMS) devices, consisting of both electronic and mechanical components are emerging as the next-generation technology that can significantly impact people's lives. It has intrigued the research community for over a decade, not only due to the rich fundamental science where devices are made on the nanoscale,[11,48] but also due to the high potential of making technical breakthroughs in various areas including robotics,[85] biomedical research,[86-88] and optoelectronics.[13,89,90]

Rotary nanomotors, a type of NEMS devices, are particularly critical for advancing NEMS technology in converting electric energy into nanoscale mechanical motions for nanomachines and nano-factories.[13,30,91] Traditional fabrication of miniature motors requires complex design and arduous processes.[9,35,37,60] For instance, a simple rotary microelectromechanical systems (MEMS) device requires fabrication and integration of multiple components including rotors, bearings, hubs, and stators all on miniaturized scales.[31,35,37,91] Using traditional MEMS technologies— photolithography and micromachining borrowed from the microelectronics industry, hundreds of fabrication steps are required. The devices suffer from low yield and short lifetime.[92] Only several rotary MEMS were made on each wafer and most of them just operated from a few seconds to a few hours.[35,36] Therefore, it is extremely difficult to apply techniques learned in MEMS to the fabrication of even smaller NEMS devices. This is also evidenced by the restricted sizes of MEMS motors of millimeters to hundreds of micrometers.[34,36,41] Few can reach tens of micrometers and very few can make truly nanoscale motors even using the best available techniques.[9,60,93] It is highly desirable to

investigate new mechanisms to realize large arrays of rotary NEMS devices with high efficiency, nanoscale dimensions, reliable performance, and at a low cost.

Recently, intensive research efforts have been focused on using nanoentities as actuation components for MEMS/NEMS devices due to the unique advantages provided by nanotechnology: (1) large arrays of nanoentities with controlled geometry, chemistry, physical and mechanical properties can be routinely synthesized at low cost.[42] (2) The size of the MEMS devices can be significantly shrunk by using synthesized nanoentities as building blocks.[48] (3) The unique physical/chemical/electrical properties of nanoparticles improve the performance of miniaturized mechanical devices.[50,51]

A group at UC Berkeley fabricated nanomotors with top-down multi-step electron-beam (E-beam) lithography.[60] In such a device, a nanoscale metal pad was attached to a piece of suspended multiwall carbon nanotube (MWCNT) via E-beam lithography. With high electric voltages, the metal pad rotated around the MWCNT with the inner walls of carbon nanotubes serving as bearings. The excellent demonstration of nanoentities for rotary NEMS, however, required complex fabrication procedure. Recently, a group at Cornell University made another type of nanomotors based on inorganic and organic hybrid structures.[9] Molecular motors, a type of rotary protein, were used as the driving component of the nanomotors. Lithographically patterned inorganic nanorods attached to the molecular motors were used as rotors. When hydrolyzing adenosine triphosphate (ATP), the molecular motors can make the inorganic nanorods rotate. Due to the complexity of the conjugation of inorganic nanorods to molecular motors, only a few nanorods out of hundreds had been rotated. Also, limited by the characteristics of natural molecular motors, the devices could not alter either their rotation or speed. Catalytic nanomotors have emerged as a new type of nano-mechanical devices that convert chemical energy to mechanical motions.[30,94,95] Most of the catalytic

motors have been actuated to transport biomolecules, such as proteins or bacteria.[96] Recently, it was demonstrated that asymmetrical and one-end fixed nanorods could rotate,[24,97] nevertheless, with random speed, orientation, and locations.

In this chapter, we report innovative design and mechanisms for assembling and operating arrays of rotary NEMS devices made from nanoscale building blocks. The nanomotors consist of multisegment nanowires, patterned nanomagnets, and quadrupole microelectrodes as rotors, bearings, and stators, respectively. Arrays of nanomotors can be assembled and rotated with controlled angle, speed (to at least 18,000 revolutions per minute (rpm)), and chirality. The fundamental electric, magnetic, and mechanical interactions involved in the components of the nanomotor systems were investigated, which provide understanding for designing and actuating various metallic NEMS devices. The nanomotors, with all the dimensions smaller than 1 μm, can robustly rotate for 15 hours for more than 240,000 cycles and were demonstrated for controllable biochemical release. The innovation in this research may inspire multiple research fields including MEMS/NEMS, bio-NEMS, micro/nanofluidics, and lab-on-a-chip architecture.

3.2. Results and Discussion

3.2.1. Design of Nanomotors

We investigated a unique type of nanomotors made of strategically assembled nanoentities, such as nanowires and nanodisks, as shown in Fig. 3.1(a) and (b). The nanomotors consist of multisegment Au/Ni/Au nanowires (150 – 400 nm in diameter and ~800 nm – 10 μm in length) acting as rotors, patterned nanomagnets (200 nm – 2 μm in diameter) acting as bearings, and simple quadruple microelectrodes acting as stators. The patterned nanomagnets are the core components for the anchorage of the rotary parts. The

nanomagnets consist of tri-layer thin-film stacks of Au/M/Cr, where M representing magnetic materials such as Ni and Co. Each layer in the nanomagnets serves a purpose: the bottom Cr layer adheres to the substrate, the middle magnetic layer provides the magnetic field, and the top Au layer is used for adjusting the spacing between the magnetic layer and the nanowires in order to tune the magnetic attraction. The magnetic attraction can be adjusted so precisely that it can anchor the nanowires to the bearings, but not too tightly to prevent the nanowires from rotating.

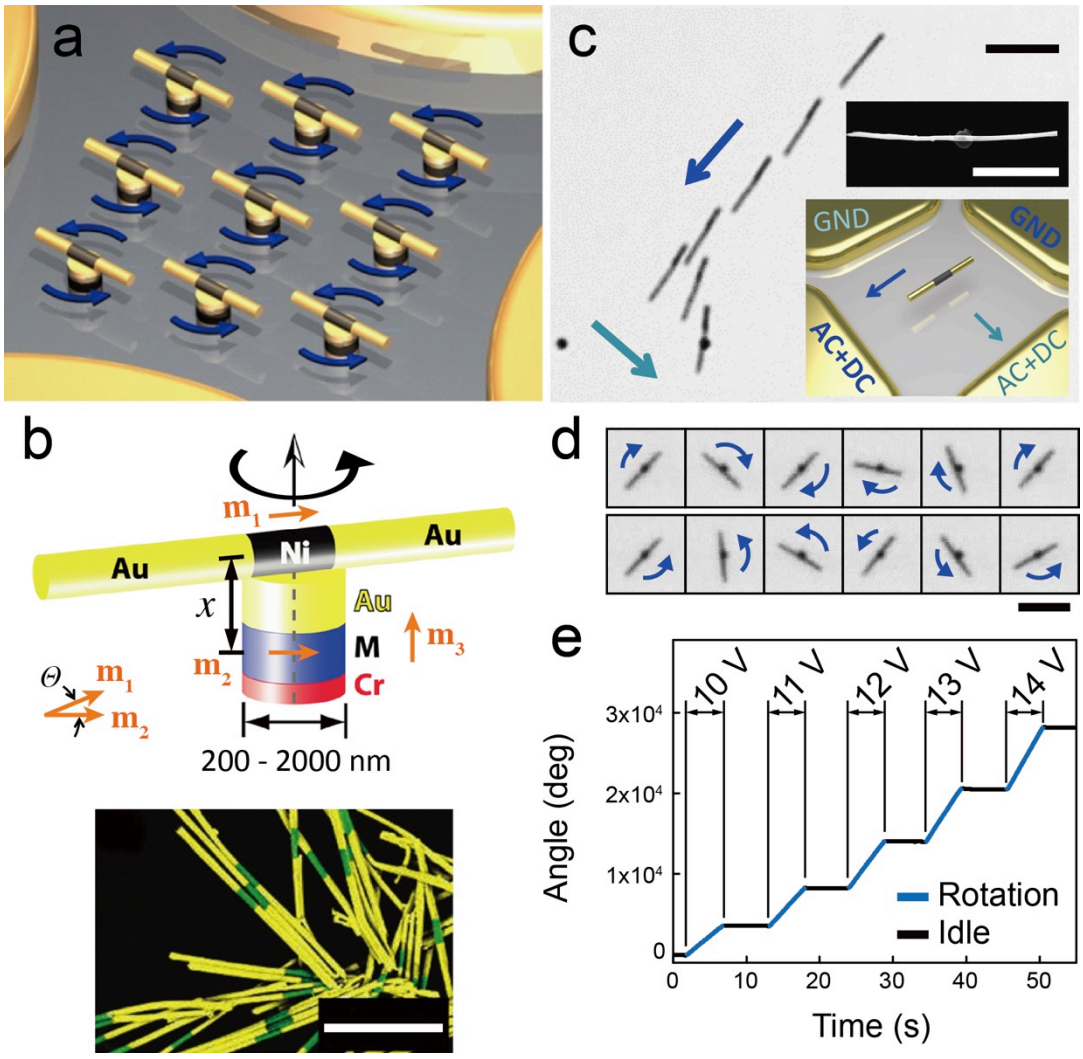

Figure 3.1: Design, assembly and actuation of nanomotors (a) Schematic diagram of an array of nanomotors assembled from nanoscale building blocks with multi-segment Au/Ni/Au nanowires as rotators, tri-layer Au/Ni/Cr magnets as bearings, and microelectrodes as stators. (b) Schematic diagram of a nanomotor and a SEM image of Au/Ni/Au nanowires highlighted in false colors (yellow: Au; green: Ni). Scale bar: 5 μm. (c) Overlapped images of an Au/Ni/Au nanowire transported and assembled on a nanobearing by the electric tweezers. Scale bar: 10 μm. (Inset) SEM image of an assembled nanomotor (scale bar: 5 μm) and a schematic diagram of the electric tweezers manipulating a nanowire. (d) Snapshots of a nanowire rotating on a nanobearing CW and CCW every 71 ms. Scale bar: 10 μm. (e) Angular position θ of an assembled nanowire in AC **E**-fields of 10 – 14 V [rotor: Au(4.5 μm)/Ni(1 μm)/Au(4.5 μm); bearing: a thin film stack made of Au(100 nm)/Ni(80 nm)/Cr(6 nm) and 1 μm in diameter].

3.2.2. Assembly and Actuation of Nanomotors

To realize such nanomotors, there are two fundamental problems to be addressed: (1) *how to precisely assemble nanomotors with nanowires anchoring on the patterned nanomagnets?* (2) *How to rotate the nanomotors?* Here, we exploited the use of "the electric tweezers" to resolve these problems. Electric tweezers are our recently invented nano-manipulation technique, which can transport nanoentities, such as nanowires and nanotubes, along arbitrary trajectories to designated positions with a precision of 150 nm[12,47,78] and rotate them with prescribed angle, speed, and chirality.[49]

The nanowire rotors, vital components of the rotrary nanomotors, were designed with a three-segment Au/Ni/Au structure, where the Ni segment serves to anchor the nanowires on the patterned magnetic bearings. Here, Au/Ni/Au nanowires were fabricated by electrodeposition into nanoporous templates in a three-electrode cell setup as detailed in the experimental session.[12,43] In a three-electrode setup, Cu layer on the back of nanoporous anodized aluminium oxide (AAO) template, Pt mesh, and a Ag/AgCl electrode serve as a working electrode, a counter electrode, and a reference electrode, respectivly. The growth of the nanowires commences at the bottom of nanopores at the working electrode. The amount of electric charges passing through the circuit controls the length of each segment. As a result, arrays of nanowires, with a structure of 100 – 1000-nm-long Ni segment sandwiched between two 350 – 500-nm-long Au segments, were synthesized and suspended in DI water.

4 μl of nanowire suspension in deionized (DI) water was introduced into a reservoir of volume of ~4 μl that was made of polydimethylsiloxane (PDMS) elastomers assembled on top of the microelectrodes. Then the reservoir was sealed with a glass cover slip. By using the electric tweezers, the nanowires can be transported by the DC **E**-field and aligned either parallel (AC//DC) or perpendicular (AC⊥DC) to their transport

directions by the AC **E**-field. By controlling the durations of the combined AC and DC **E**-fields in both the X and Y directions, the nanowires can be precisely manipulated in two dimensions along prescribed trajectories to the patterned magnetic bearings as shown in Fig. 3.1(c). When positioned in the vicinity of a nanobearing, the nanowire is swiftly attracted and assembled atop of the nanobearing by the magnetic force between the nanowire and nanobearing. Once anchored on the nanobearing, the nanowire cannot be moved by the **E**-fields any more. In such a manner, we can readily form ordered arrays of nanomotors by transporting and assembling nanowires in series. Due to the efficient manipulation by the electric tweezers, each assembling event only takes a few seconds.

The nanobearings (200 nm – 2 μm in diameter), anchoring nanowire rotors, have an embedded Ni film with a gently tilted perpendicular magnetic anisotropy (PMA) to provide magnetic anchoring force [Fig. 3.2].[79] The in-plane magnetic orientation of the nanobearings is controlled by demagnetization with a gradually reducing oscillating magnetic field of ±10 kG followed by re-magnetization at 10 kG along a desired direction for 5 seconds.

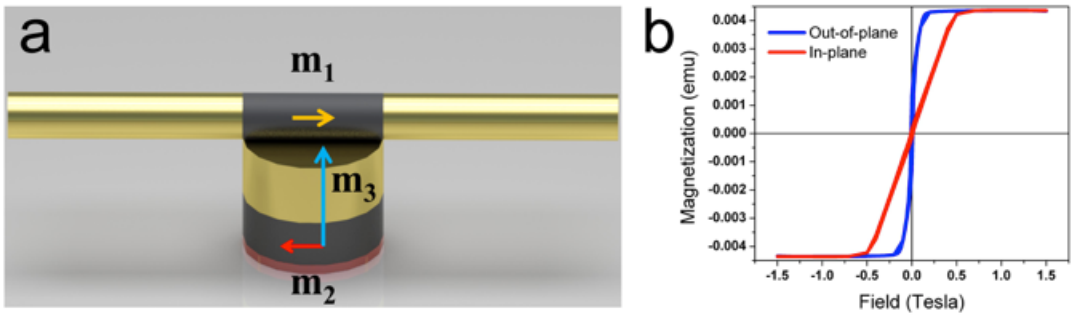

Figure 3.2: Perpendicular magnetic anisotropy (PMA) of Ni. (a) A Au/Ni/Au nanowire with a magnetic moment (m_1) is assembled on a nanobearing consisting of a thin film stack of Au/Ni/Cr. The Ni layer in the nanobearing has a slanted PMA which consists of a perpendicular component (m_3) and an in-plane component (m_2). After treatment with an in-plane oscillating magnetic field, m_3 can be much smaller. The nanowire spontaneously aligns due to the magnetic interaction between m_1 and m_2 and its orientation is determined by the treatment direction of the external magnetic field. (b) Vibrating sample magnetometer (VSM) magnetic hysteresis loops of a 200 nm Ni thin film show the PMA nature of the Ni magnetic bearing.

Applying four AC voltages (10 kHz – 150 kHz, 8 – 17 V) with sequential phase shifts of 90° on the quadruple microelectrodes, we created a rotating AC **E**-field, which can instantly drive arrays of nanowires to rotate atop of the magnetic bearings.[11] The motions of the rotating nanomotors were captured by an optical microscope equipped with a CCD camera operating at 14 – 200 frames per second (fps). The nanomotors were rotated both clockwise (CW) and counterclockwise (CCW), same as that of the rotating **E**-fields as shown in Fig. 3.1(d). At each AC voltage, the rotation instantly started, reached a terminal velocity, and stopped as soon as the external **E**-field was removed without observable acceleration or deceleration [Fig. 3.1(e)]. The instant rotation response is due to the extremely low Reynolds number of 10^{-5} for nanowires in DI water, where the viscous force overwhelms the motion.[98] Taking a closer look, we noticed that the plot of rotation angle (θ) versus time (t) was not completely linear [Fig. 3.3(a)]. By

taking the first derivative of angle with respect to time, we could obtain rotation speed (ω), which showed a clear sinusoidal dependence on time (t) and angle (θ), oscillating between two states: the high speed (ω_{Max}) and low speed states (ω_{min}) with a periodicity of 360° [Fig. 3.3(b) and (c)]. To understand these phenomena, a thorough investigation of electric, magnetic, and mechanical forces/torques in the nanoscale components of a nanomotor system is highly desirable.

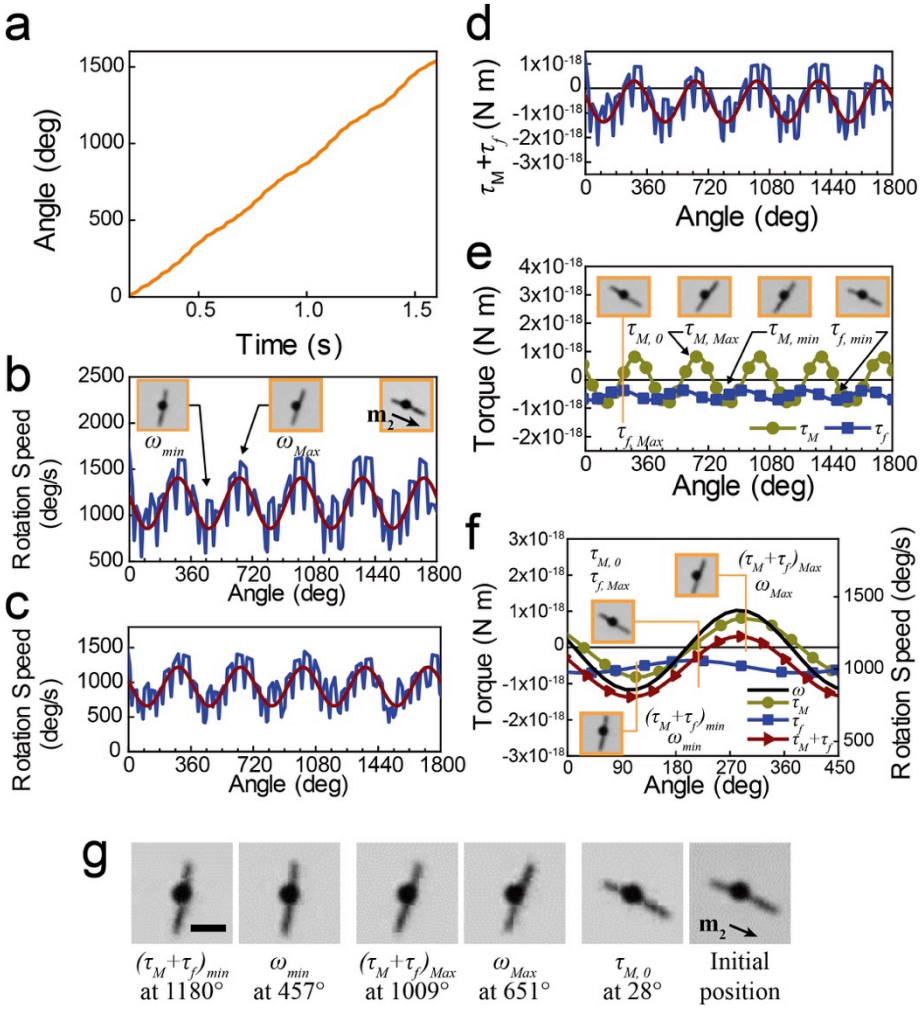

Figure 3.3: Characteristics of rotational dynamics (a) Rotation angle (θ) versus time (t). (b – c) Rotation speed (ω) versus angular position (θ) of the nanomotor at (b) 12V and (c) 11 V, 10 kHz (CW) (d) Sum of the magnetic (τ_M) and friction torques (τ_f): ($\tau_M + \tau_f$) exerted on the motor at 12 V, 10 kHz. (e) Analytic solutions of τ_M and τ_f versus angle with the snapshots illustrating the angular position of the nanomotor for $\tau_{M,0}$, $\tau_{M,Max}$, $\tau_{M,min}$, $\tau_{f,Max}$, and $\tau_{f,min}$, (f) Angle-dependent torques of ($\tau_M + \tau_f$), τ_M, τ_f, and rotation speed ω of the nanorotor at 12 V, 10 kHz. The snapshots showed the angular positions of the nanomotor when the rotation speeds are the maximum (ω_{Max}), minimum (ω_{min}), the combined magnetic and frictional torque of ($\tau_M + \tau_f$) is maximum, $(\tau_M + \tau_f)_{min}$, and $\tau_{M,0}$, respectively. (g) The maximum/minimum rotation speeds of nanomotors occur when the combined torque of ($\tau_M + \tau_f$) is the maximum/minimum in the same direction of **E**-field. The alignment of the rotating nanomotor at $\tau_M = 0$ is the same as the initial alignment of the just-assembled nanowire. Scale bar: 5 μm.

3.2.3. Nanoscale Interactions in the Nanomotors

Similar to the systems discussed in the previous chapter, five torques can be identified in the nanomotor system given by:

$$\tau_e + \tau_{e'} + \tau_\eta + \tau_M + \tau_f = 0 \tag{3.1}$$

where τ_e, $\tau_{e'}$, τ_η, τ_M, and τ_f are the electric torque due to the rotating AC **E**-fields, effective torque due to the induced electric polarization of the nanowire and bearing, viscous drag torque from the water medium, magnetic and frictional torques between the magnetic segment in the nanowire and the magnetic nanobearing, respectively.

The viscous drag torque τ_η on a rotating nanowire in DI water is calculated as:[81]

$$\tau_\eta = \frac{1}{3}\omega\pi\eta l^3 \frac{N^3-N}{N^3\left[\ln\left(\frac{l}{Nr}\right)+0.5\right]} = -1.74\times10^{-19}\omega \text{ [N m]} \tag{3.2}$$

where r and l are the radius and length of the nanowire, respectively, η is the viscous coefficient of suspension medium, and N is the number of nanowire segments used for estimation of the viscous drag torque, which is taken as 2. For a nanowire of 150 nm in radius and 10 μm in length, $\tau_\eta = -1.74\times10^{-19}\ \omega$ [N m].

We note that, in addition to the viscous drag torque as discussed as above, a nanowire rotating close to a substrate also experiences a wall effect. If we consider a rotating nanowire consisting of multiple longitudinal segments moving perpendicular to their long directions, it was shown that the wall-induced drag force (F_W) for a rod moving perpendicular to its long direction between two walls can be approximated as $F_W = 2\pi\eta v l W\varepsilon^2$ by using the Slender body theory,[99] where W, ~O(1), is a complex factor determined by the length (l) and radius (r) of nanowires, the distance of the nanowire to

the wall and so on, v is the velocity, η is the viscous coefficient, and $\varepsilon = [\ln (l/r)]^{-1}$. Approximately, only one wall is located close to the rotating nanowire and the dragging coefficient can be further reduced to $\pi\eta v l\varepsilon^2$. Since the nanowires have high-aspect-ratios ($l>>r$), the wall effect F_W is small, ~6.7% of the viscous force received by the nanowire. The corresponding torque due to the wall effect is estimated as $\sim 10^{-20}$ N m for nanomotors rotating at a speed of 0 – 1500° s^{-1}, while the electric and the viscous torques are in the order of 10^{-18} N m, the magnetic torque is $\sim 1\times 10^{-18}$ N m, and the induced electric torque is in the order of 10^{-19} N m.

The nanowire is placed closer to one wall than to the other so that the difference of the wall effects received by the nanowire could result in a lifting force. The magnitude of the force should be a fraction of the aforementioned dragging force due to the wall. Since the torque due to the wall effect is $\sim 10^{-20}$ N m as calculated above, the lifting force should be in the range of $\sim 10^{-16}$ N for the 10-μm-long nanowire. In comparison, the electric, magnetic, and viscous forces are a few orders of magnitude higher, in the range of 10^{-14} to 10^{-13} N. Overall, the wall effect is much smaller compared to other involved forces or torques and can be safely omitted.

The electric torque is due to the interaction of the polarized nanoparticles with the AC **E**-fields, given by[82]

$$\tau_e = \frac{2\pi}{3} r^2 l \varepsilon_m \mathrm{Im}(K) E^2 = aV^2 \tag{3.3}$$

where ε_m and Im(K) are the permittivity of the suspension medium and the imaginary part of the Clausius-Mossotti factor K of the nanowire, respectively, and V is the applied voltage, as $E \propto V$. Since τ_e solely depends on the suspension medium, Im(K), and the dimension of a nanowire, the value of τ_e for an assembled nanowire rotor should be

identical with that on the same nanowire when it freely rotates in suspension. Note that for a free rotating nanowire, the electric torque balances with the viscous torque ($\tau_e = \tau_\eta$). Therefore, by combining Eq. (3.2) and (3.3), the electric torque (τ_e) for the assembled nanowire rotor can be readily calculated from that of a free rotating nanowire, and the rotation speed $\omega \propto V^2$. Indeed, the linear dependence of ω versus V^2 was experimentally observed, with a slope of $a/(1.74\times10^{-19}$ [N m s]) = 9.91 [° s^{-1} V^{-2}] as shown in Fig. 3.4(a, orange line, for the free rotating nanowire). Therefore, the electric torque can be readily determined as $\tau_e = 3.01\times10^{-20}\ V^2$ [N m]. At a given voltage, e.g., 12 V, the nanowire rotor receives an electric torque of 4.33 pN μm.

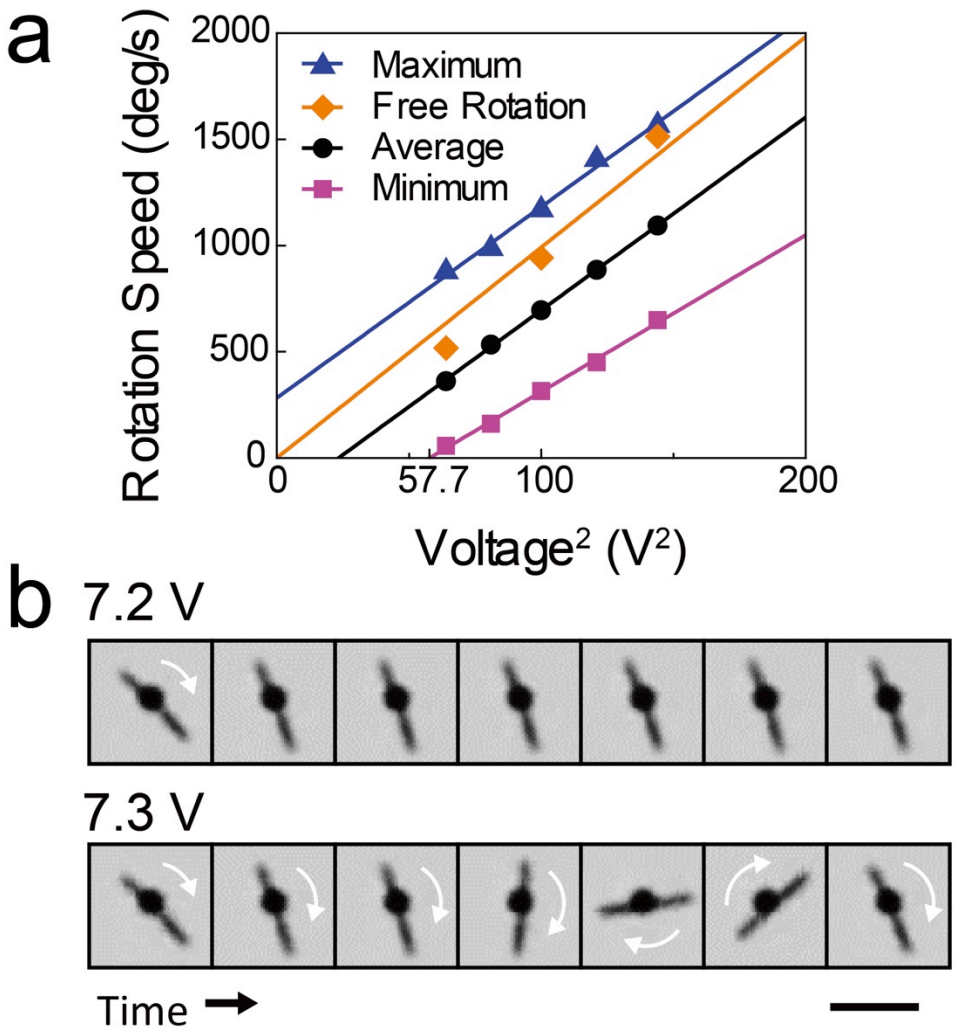

Figure 3.4: Rotation speed at different voltages and the threshold voltage (a) High (blue), low (magenta), and average (black) rotation speeds of a nanomotor (rotor: Au(4.5 μm)/Ni(1 μm)/Au(4.5 μm) nanowires, 2-μm-diameter bearings made of a thin film stack of Au(100 nm)/Ni (80 nm)/Cr (6 nm)) linearly increase with V^2 (the same was observed for nanomotors with bearings of 500 nm – 1 μm in diameter as in the Fig. 3.5). For the same nanowire freely rotating in suspension, the rotation speeds increase with V^2 with a steeper slope (orange). (b) Snapshots of the nanomotor taken every 400 ms at AC voltages of 7.2 and 7.3 V, respectively, show the threshold voltage is 7.3 V. Scale bar: 10 μm.

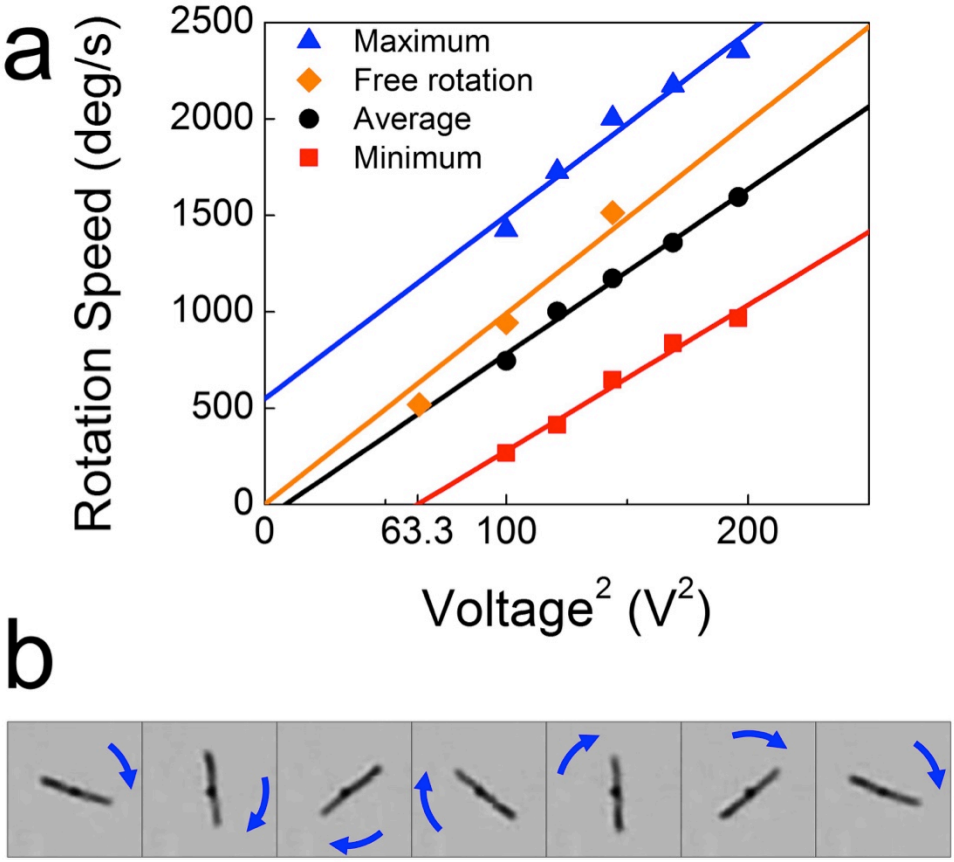

Figure 3.5: Rotation of nanomotors with nanobearings of 1 μm to 500 nm in diameter. (a) The high (blue), low (red), and average (black) speeds of a rotating nanorotor [Au(4.5 μm)/Ni(1 μm)/Au(4.5 μm)] on an 1-μm magnetic bearing (Au(100 nm)/Ni(80 nm)/Cr(6 nm). (b) Snap shots of a nanomotor rotating on a 500-nm magnetic bearing every 67 msec. The feature size of the nanomotors can be further scaled down by reducing the size of nanobearings from 2 μm to 1 μm and 500 nm in diameter. The dynamic characteristics of the nanomotors were analyzed with the same methods discussed in the main text, which shows similar linear relationship of ω-V^2 with that found in nanomotors with bearings of 2 μm in diameter [Fig. 3.4(a)].

The induced torque (τ_e) due to the electrically polarized nanorotor and nanobearing in an external AC **E**-field has a much lower, though non-negligible effect, on the nanomotor than that of the driving electric torque (τ_e). This induced torque played two roles on the rotation of nanomotors, both of which are proportional to E^2 and thus V^2:

first, it directly hinders the rotation of nanorotors; second, it results in an additional frictional torque between the rotor and bearing due to the electrostatic attraction, besides that arisen from the magnetic attraction. These two effects can be known from the slopes of ω–V^2 plots in Fig. 3.4(a), where the rotation slopes of a nanowire motor (blue, black, and magenta) are consistently lower than that of the same nanowires when freely rotating (orange). Note that no other torques, either the magnetic (τ_M) or frictional torques (τ_f), given in Eq. (3.1) depends on the external **E**-fields. Therefore, the reduced slope is a sole result of the induced torques between the electrically polarized nanowire and bearing. Based on this understanding, we can calculate the induced torque as $\tau_{e'} = bV^2$, where b is a constant that equals to -2.52×10^{-21} [N m V^{-2}], from rotation of the free/anchored nanowire in Fig. 3.4(a). The b value is approximately 1/10 of that for the electric torque (τ_e), showing the non-negligible effect of the induced electric torques in components of metallic NEMS devices.

Given the drag (τ_η), electric (τ_e), and induced torques due to **E**-field ($\tau_{e'}$), the sum of the non-**E**-field dependent magnetic (τ_M) and frictional torques (τ_f) exerted on the nanowire rotors can be readily known from Eq. (3.1). The combined torques of ($\tau_M + \tau_f$) exhibit a sinusoidal feature as shown in Fig. 3.3(d), which counts for the angle-dependent periodic rotation of nanomotors in Fig. 3.3(b) and (c) [Fig. 3.6]. To explicitly understand the contributions of the magnetic and frictional torques, we modeled the system using a simplified magnetic dipole-dipole interaction.[77] As shown in Fig. 3.1(b), the angle dependent magnetic torque between the rotor and bearing is determined by the horizontal magnetic moments of the nanowire ($\mathbf{m_1}$) and bearing ($\mathbf{m_2}$), given by $\tau_M(x,\Theta,m_1,m_2) = \mu_0(m_1m_2 \sin \Theta)/(4\pi x^3)$ and the angle-dependent magnetic force is $F_M(x,\Theta,m_1,m_2) = 3\mu_0(m_1m_2 \cos \Theta)/(4\pi x^4) + c$, where μ_0 is the magnetic permittivity of vacuum, Θ is the angle between $\mathbf{m_1}$ and $\mathbf{m_2}$, x is the separation distance between the nanowire and the Ni

layer in the nanobearing, and the constant c is the magnetic force due to the magnetic moments of the nanobearing in the vertical direction ($\mathbf{m_3}$) and the horizontal magnetic moment of the nanowire ($\mathbf{m_1}$). If the friction coefficient at the interface of the nanowire and bearing is μ, the frictional torque $\tau_f = \mu F$, then ($\tau_M + \tau_f$) can be written as:

$$\tau_M + \tau_f = d\sin(\theta - \theta_M) + e\cos(\theta - \theta_M) + f \tag{3.4}$$

where d, e, and f are constants, θ and θ_M are the angular positions of magnetic orientation of the nanowire and nanobearing, respectively, and $\Theta = \theta - \theta_M$. Fitting the experimentally obtained torque of ($\tau_M + \tau_f$) versus θ in Fig. 3.3(d), we readily extracted the angular dependent magnetic torque of $\tau_M = -8.19\times10^{-19}$ sin (θ - 27°) [N m] and frictional torque of $\tau_f = -1.71\times10^{-19}$ cos (θ - 27°) - 5.35×10^{-19} [N m] at 12 V, 10 kHz as shown in Fig. 3.3(e). By using the same approach, the values of d, e, f, and θ_M were also determined for 10 and 11 V, which show excellent consistence with those obtained at 12 V [Table 3.1]. These results provide great support for our modeling, where the magnetic and its resulting frictional torque are independent of the applied **E**-field. We also note that the highest rotation speed (ω_{Max}) occurred neither when the magnetic torque has the highest value ($\tau_{M,Max}$) in the same direction with the driving **E**-field, when the magnetic torque equals to zero ($\tau_{M,0}$) aligning with the magnetic orientation of the bearing, nor when the frictional torque has the lowest value ($\tau_{f,min}$). The highest/lowest speed occurred when the sum of ($\tau_M + \tau_f$) was maximum/minimum in the orientation of the electric torque [inset of Fig. 3.3(f)].

Applied Voltage (V)	τ_M (N m)	τ_f (N m)
12	$-8.19\times10^{-19}\sin\Theta$	$-1.71\times10^{-19}\cos\Theta - 5.35\times10^{-19}$
11	$-8.36\times10^{-19}\sin\Theta$	$-1.39\times10^{-19}\cos\Theta - 4.84\times10^{-19}$
10	$-7.33\times10^{-19}\sin\Theta$	$-1.44\times10^{-19}\cos\Theta - 5.41\times10^{-19}$

Table 3.1: Magnetic (τ_M) and friction torque (τ_f) at different applied voltages.

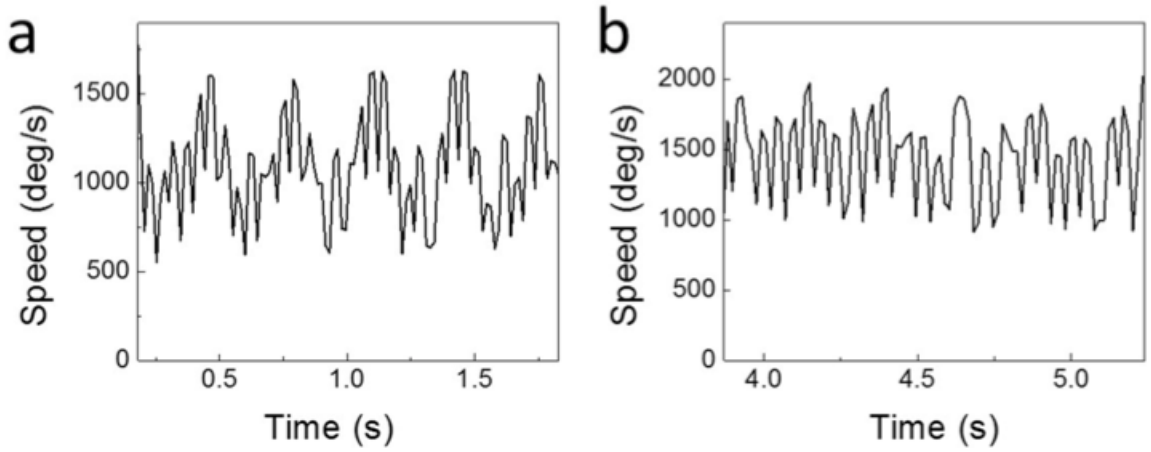

Figure 3.6: Rotation of a nanomotor as a function of time. The oscillation of the speed of a nanomotor results from the magnetic interaction of a nanowire rotor with a magnetic nanobearing. It is further proved by comparing rotation of (a) a nanowire rotor assembled on a nanobearing and (b) a nanowire of a similar dimension freely suspended in a liquid medium, i.e., D.I. water. While the rotation of the nanomotor shows the oscillation with a clear periodicity owing to the angle-dependent magnetic torque and force [(a)], the nanowire rotating freely does not oscillate as a function of either angle or time [(b)].

The feasibility of the modeling and torque analysis can be further confirmed by plotting the experimentally obtained highest (ω_{Max}, blue) and lowest rotation speeds (ω_{min}, magenta) of the nanomotors at each applied voltage (V) as functions of V^2 [Fig. 3.4(a)].

Both ω_{min} and ω_{Max} linearly increase with V^2, parallel to that of the average rotation speed (ω_{AVG}, black) versus V^2, but vertically offset. Combining Eq. (3.1) – (3.4), we obtained

$$\omega = \frac{a+b}{1.74\times10^{-19}}V^2 + \frac{\sqrt{d^2+e^2}\sin(\theta-\theta_M+\delta)+f}{1.74\times10^{-19}} \quad (3.5)$$

where δ = arctan (e/d). ω_{Max} and ω_{min} occur when sin (θ - θ_M + δ) = ±1, respectively. The V^2 dependence in Eq. (3.5) is consistent with the experimentally found V^2 dependence of ω_{min} and ω_{Max} in Fig. 3.4(a). The constant slope (a + b)/(1.74×10^{-19}) of ω–V^2, accounts for the parallel slopes of ω_{Max}–V^2, ω_{min}–V^2, and ω_{AVG}–V^2 in Fig. 3.4(a). Moreover, the x-intercept of ω_{min}–V^2 can be used to estimate the threshold voltage (V_{th}) required to initiate the rotation of nanomotors. It predicts a threshold voltage value of $\sqrt{57.7}$ = 7.6 V for a motor with a 2-μm-diameter bearing. This predicted value is very close to that of experimentally obtained 7.3 V, as the nanomotor failed to rotate a complete cycle up to 7.2 V [Fig. 3.4(b)]. It indicates that the minimum required voltage to initiate the nanomotor rotation should overcome the maximum value of the combined magnetic and frictional torques (τ_M + τ_f) countering the electric torque. In summary, our modeling qualitatively revealed the distinct roles of various nanoscale torques involved in the nanomotor system, which excellently agreed with the experimental results. The new understandings from this investigation can be applied to design of various metallic NEMS devices.

3.2.4. Ordered Arrays of Nanomotors

To practically use the nanomotors for applications, it is important to evaluate the controllability, robustness, and efficiency in assembling and rotating arrays of

nanomotors. We patterned and rotated ordered 2×2 and 1×3 arrays of nanowire motors as shown in Fig. 3.7(a) – (b). The manipulation and assembling of nanomotors do not require advanced skills as the system is interfaced by user-friendly software. It took only ~10 seconds for a user, e.g., a K-12 student, to assemble one motor after training and practicing for several times. It generally took less than 1 minute to assemble a 2×2 array. Although the assembling efficiency is already much higher than those made by traditional lithographical techniques, which require advanced skills, training, and education, we are in the process of developing an intelligent system to automate the nanowire recognition and manipulation for further improving the assembling efficiency of nanomotors. All nanomotors in the array started, stopped, and reversed rotation simultaneously. The speed and chirality were precisely controlled by the voltages and phase shifts of the applied AC **E**-field [Fig. 3.7(c)]. The rotation speeds of individual nanomotors were slightly different, which is due to the variations of dimensions of individual nanowires and bearings, as well as their interfaces.

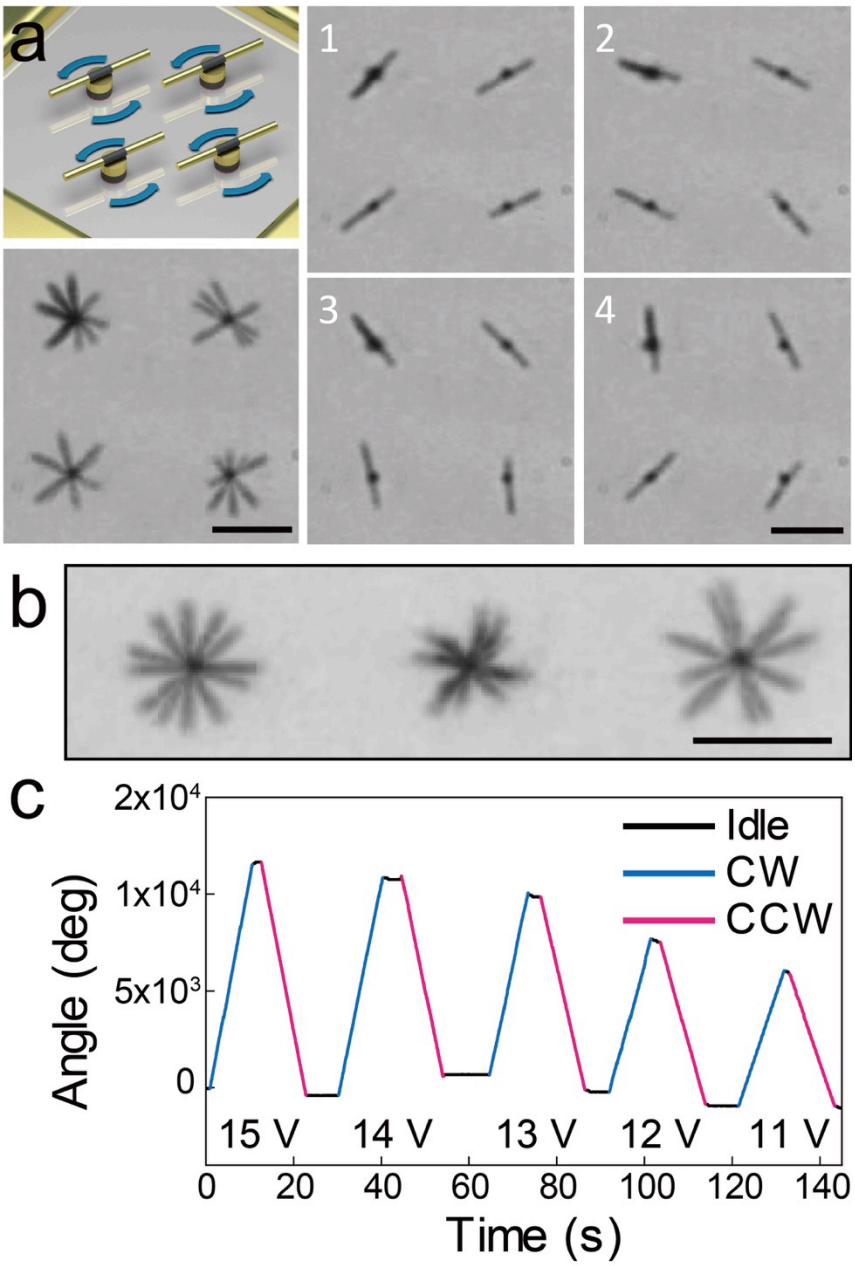

Figure 3.7: Nanomotors assembled in ordered arrays (a) Schematic diagrams and snapshot images of a 2×2 nanomotor array rotating clockwise at 12 V, 10 kHz. (b) Overlapped snapshot image of a 1×3 nanomotor array at 15 V, 10 kHz. Scale bars: 10 μm. (c) The rotation speed of nanomotors can be precisely controlled by AC **E**-fields as shown by rotation angle (θ) versus time at 15 – 11 V, 10 kHz. The nanomotors can instantly rotate in orientations both clockwise (blue) and counterclockwise (magenta) and stop on demand.

3.2.5. Ultrahigh-Speed Rotation of Nanomotors

How fast can the nanomotors ultimately rotate? To test the limit, we optimized the AC **E**-field intensity and frequency. As aforediscussed, the rotation speed of nanomotors increases with E^2. Simply narrowing the quadrupole electrodes from a gap distance of 500 μm to 100 μm, we readily increased E^2 by 25 times. The rotation speed also depends on the applied AC frequency. For 10-μm-long Au/Ni/Au nanowires in DI water, the maximum rotation speed was obtained experimentally at an **E**-field of 30 kHz [Fig. 3.8]. Applying these optimized conditions, we rotated nanomotors to a speed of at least 18,000 rpm at 17 V as shown in the inset of Fig. 3.9(a) – (b). Agreeing with our other results, the rotation speeds (to at least 18,000 rpm) were proportional to E^2 or V^2, which counts for the ultrahigh speed rotation at only 17 V [Fig. 3.9(a)]. As far as we know, such a rotation speed is the highest achieved in natural or man-made motors of the same scale. It is of the same speed level of jet engine, but is still not the limit. In comparison, the highest speed of nanomotors with bearings for position fixed rotation is 44.4 – 498 rpm, obtained from the organic-inorganic hybrid nanomotors.[9]

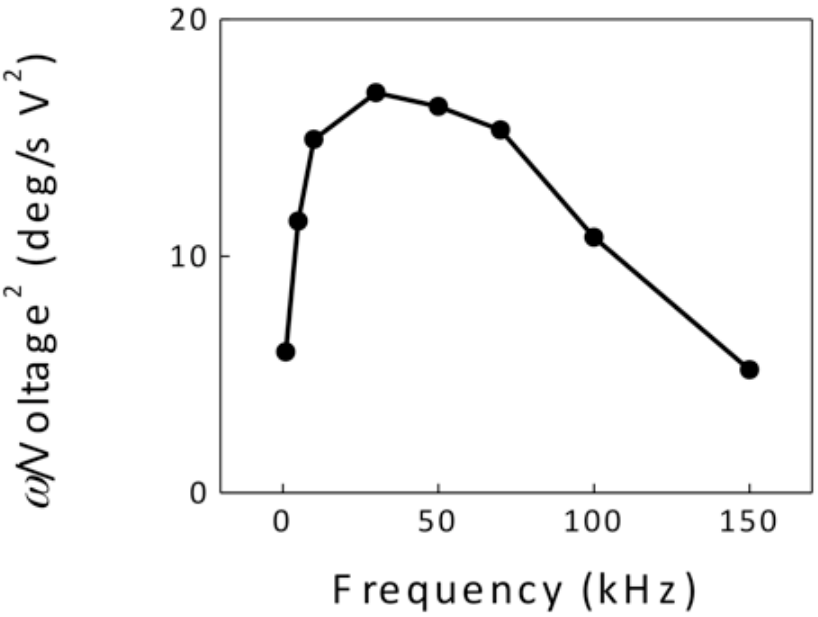

Figure 3.8: ω/V^2 versus AC frequency for free rotation of 10-μm-long Au/Ni/Au nanowires. The rotation of nanowire nanomotors in DI water depends on both the dimensions and materials of the nanowires, as well as the frequency of the AC **E**-fields. Frequency dependent rotation of 10-μm-long Au/Ni/Au nanowire rotors were investigated experimentally from 1 – 150 kHz. The highest rotation speed was obtained at 30 kHz, at which we achieved ultrahigh-speed rotation of nanomotors to 18,000 rpm.

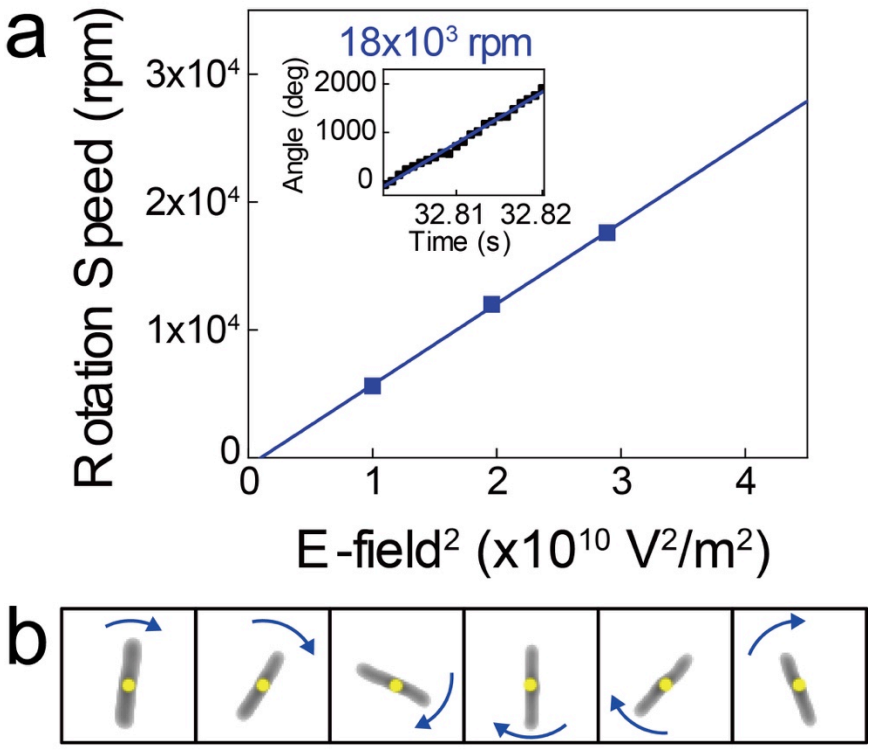

Figure 3.9: Ultrahigh speed rotation (a) Rotation speed (ω) of nanomotors from 10 – 17 V at 30 kHz in a 100-μm-gapped quadruple microelectrode. (Inset) Angle (θ) versus time of the nanomotor rotating clockwise with a speed of ~18,000 rpm. (b) Enhanced snapshot images taken every 0.8 ms of the same nanomotor rotating at ~ 18,000 rpm at 17 V, 30 kHz.

3.2.6. Ultrasmall Nanomotors

One of the biggest advantages of nanomotors is their small footprint. No physical principles prevent rotation of even smaller motors. Employing a microscope equipped with a 100× oil-immersion objective and thin cover slips as substrates, we clearly observed controllable rotation of nanomotors made of three-segment nanowire rotors of 165 nm in diameter and 800 – 900 nm in total length [Au(350 – 400 nm)/Ni(100 nm)/Au(350 – 400 nm)] and magnetic bearings of 200 nm in diameter [made of tri-layer

thin film stack of Au(20 nm)/Ni (80 nm)/Cr(6 nm)] [Fig. 3.10(a) – (c)]. All characteristic dimensions of the nanomotors are below 1 μm, which is at least 10 times smaller than that of the state-of-the-art micromotors fabricated through the top-down approach. The nanomotors are even smaller than the motors made from nanotubes.[60] The nanomotor rotates in both clockwise and counterclockwise directions at 15 V/50 kHz as shown in Fig. 3.10(d) – (e). The rotation speed is not as uniform as those of nanowire motors of a few micrometers in length, which can be attributed to stronger Brownian motions found in smaller objects in suspension. The ultimate size limit of nanomotors should be determined by Brownian motions, which is under investigation. We expect to be able to further decrease the length of the nanomotors, which requires new techniques to characterize their motions with optical microscopes.

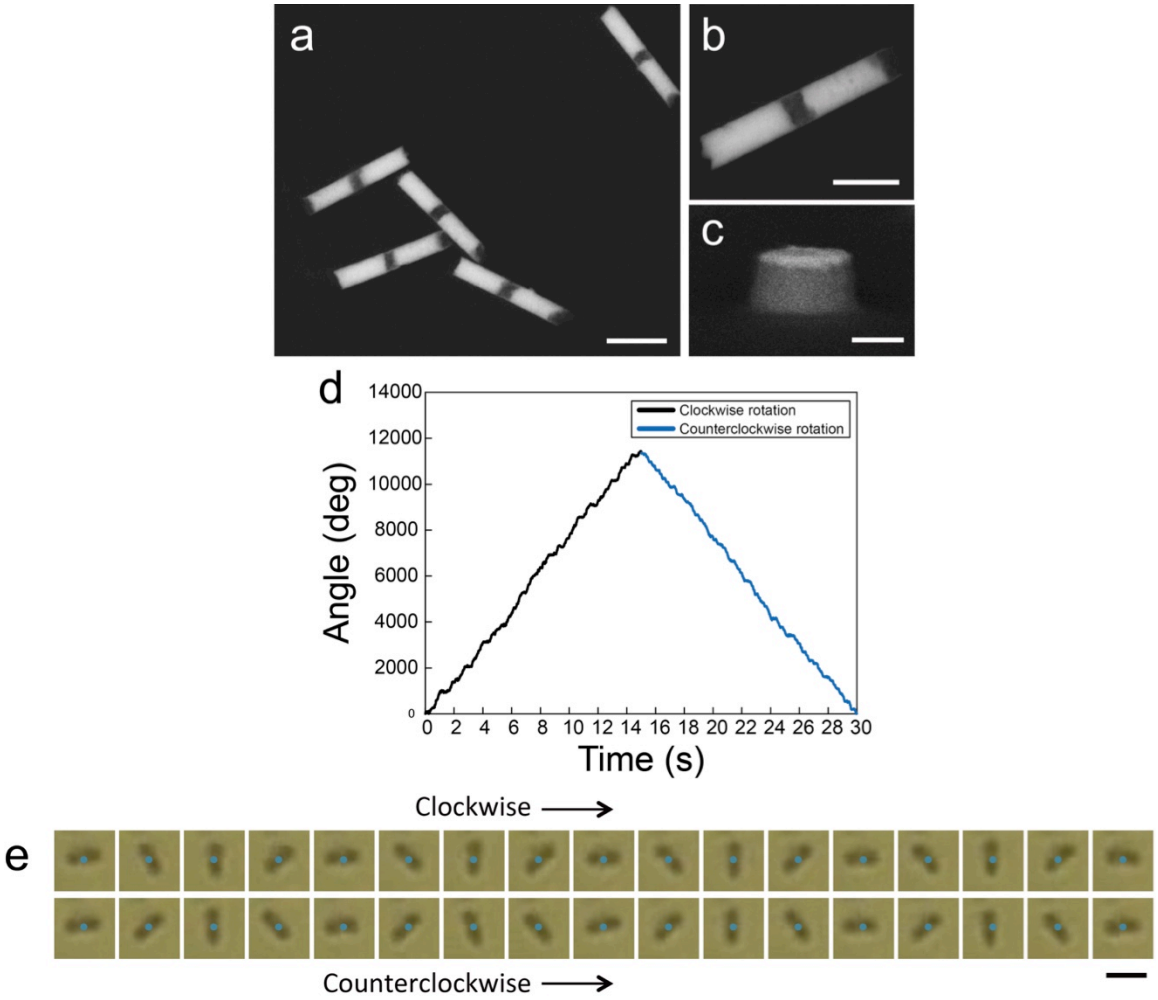

Figure 3.10: Nanomotors with all dimensions < 1 μm (a) SEM images of the as-synthesized Au/Ni/Au nanowires (800-900 nm in length and 165 nm in diameter). The scale bar is 500 nm. The Au (bright) and Ni (dark) segments are 350 – 400 nm and 100 nm, respectively. (b) A close-up image of a single nanowire (scale bar: 300 nm). (c) Magnetic bearings of ~200 nm [Au(20 nm)/Ni(80 nm)/Cr(6 nm) thin-film stacks] in diameter (scale bar: 100 nm). (d) Rotation angle as a function of time for both clockwise and counterclockwise rotation of a nanomotor made of nanowires and magnetic bearings shown in (a – c). (e) Snapshots of a rotating nanomotor taken every 60 ms (the position of the magnetic bearing is highlighted with turquoise and the scale bar is 1 μm).

3.2.7. Durability of Nanomotors

How durable are these nanomotors? We performed a test to let the devices rotate without any interruption, and found these nanomotors can keep rotating for up to 15 hours, which results in more than 240,000 cycles in total [Fig. 3.11(a)]. To our best knowledge, this is a record in both duration time and number of cycles among all reported rotary motors made from synthesized nanoparticles. This performance has surpassed the recent top-down-made Si micromotors,[37] showing the realistic potential of our nanomotors. After 15-hour rotation, the Au cap layer on magnetic bearing was significantly thinned by frictional wearing. The scanning electron microscope (SEM) image in Fig. 3.11(c) reveals the final Au thickness of ~15 nm, reduced from its original thickness of 40 nm [Fig. 3.11(b) and (c)]. No clear wear was found on the nanowire rotor [Fig. 3.11(c)], which can be attributed to the fact that Au (Vickers hardness: 216 MPa) is much softer than that of Ni (Vickers hardness: 638 MPa). The rotation of nanomotors was finally terminated by the increased magnetic attraction force and the consequential larger friction between rotors and bearings due to the reduced thickness of the Au layer resulted from frictional wearing.

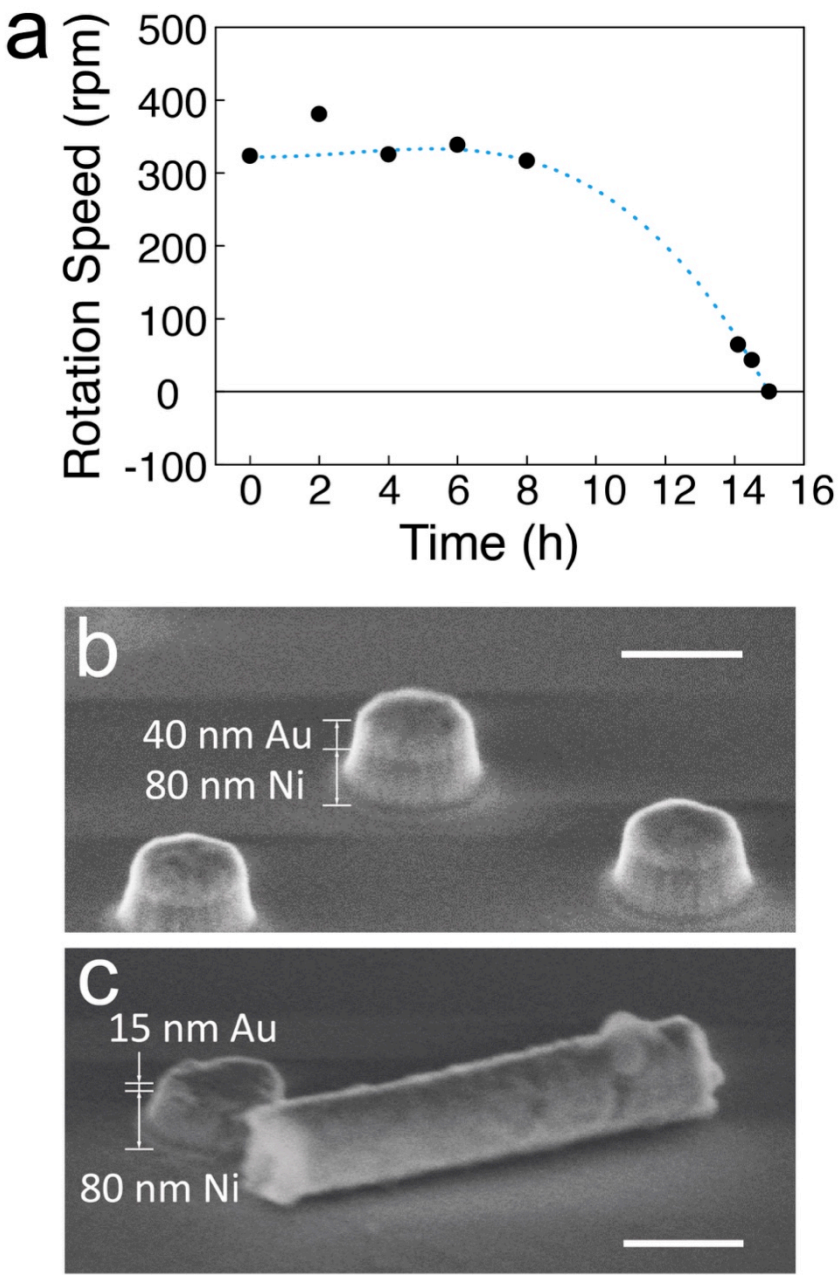

Figure 3.11: 15-hour continuous rotation Nanomotors [rotor: Au(350-400 nm)/Ni(100 nm)/Au(300-400 nm), 165 nm in diameter; bearing: ~200 nm in diameter, thin film stack of Au(40 nm)/Ni(80 nm)/Cr(6 nm)] can be rotated continuously for up to 15 hours. (a) Rotation speed versus time at 15 V, 30 kHz AC **E**-fields. Experimental data is presented as the black dots with the blue dotted trend line. (b) SEM images of the as-fabricated magnetic bearings. (c) SEM images of the magnetic bearing and nanowire rotor after 15-hour rotation. The scale bars are 200 nm.

3.2.8. Controlled Biochemical Release from Nanomotors

Finally, the applications of nanowire motors were demonstrated for rotation-controlled biochemical release as shown in Fig. 3.12(a). In this study, we chose Nile blue molecules to demonstrate controllable molecular release by mechanically rotating nanomotors, considering their large Raman scattering cross-sections for optical characterization and wide usage in tagging biomolecules for biological study. By functionalizing the surface of nanowire rotors with surface-enhanced-Raman-scattering sensitive Ag nanoparticles,[100] we detected time-dependent release of Nile blue molecules from single rotating nanomotors using Raman spectroscopy. The release rate (k) monotonically increases with the rotation speeds of nanomotors [Fig. 3.12(b)]. Biochemical release from nanoparticles can be controlled predictably by mechanical rotation, which is a completely new actuation mechanism for biochemical release.[101] The fundamental principle can be attributed to thickness change of electric-double layers, which will be studied elsewhere. Such molecule release mechanism is applicable not only to Raman-sensitive molecules but also to any biochemicals of interests, such as drugs, cytokine, DNA, antigens, and antibodies.

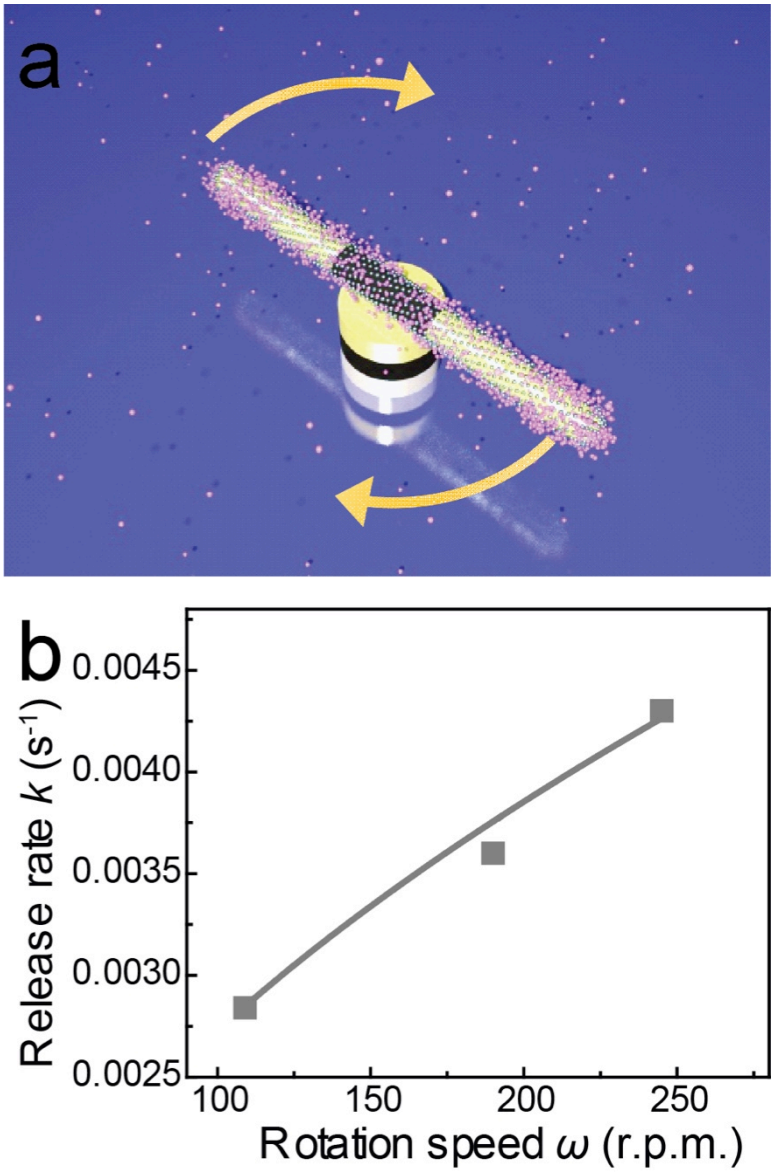

Figure 3.12: Controlled biochemical release by Nanomotors (a) Illustration of rotation controlled release of biochemicals (the motor fixed on the nanomagnet is SERS sensitive, which is a silica shelled Au-Ni-Au nanowire with uniform surface distributed Ag nanoparticles). The nanomotor is functionalized with Nile blue (in pink). (b) The release rate *k* monotonically increases with the rotation speeds of nanomotors.

The demonstration of nanomotors for biochemical release as shown above is still in a non-bioenvironment. More experiments are necessary to study the applications and limitations of nanomotors in a biosetting. It will also be interesting to exam the release characteristics from multiple nanomotors. In our previous work, we successfully employed the electric tweezers to deliver drug-functionalized nanowires to a single live cell amidst many and characterized responses from the cell,[13] which proved the compatibility of the electric tweezers with the actual bioenvironment.[13] Here, the assembling and actuation of nanomotors in a biosetting should be also feasible, as the same electric tweezers technique is employed. We envision the nanomotors as a unique tool for tunable release of biochemicals to a single live cell, which is important for understanding the fundamental signal transduction on single-cell levels.[13] One of the foreseen difficulties is how to position magnetic bearings in the vicinity of selected live cells for assembling nanomotors. This obstacle could be overcome by fabricating magnetic nanobearings on a wafer scale as shown in Fig. 3.13. Growing cells (typically 10 μm) on such substrates and controlling the density of the magnetic bearings, one can always find a few magnetic bearings close to a live cell for nanomotor assembling. We note that more work should be conducted to optimize the conditions, i.e., the amount of chemicals loaded on the nanomotors and the control of distance of the nanomotors to the cell. Various biochemicals of interests apart from Nile blue should be tested. Also note that the nanomotors can release chemicals to the vicinity of cells, while cannot deliver chemicals into cells as shown by other reports. The materials used for nanomotors should be carefully selected. Non-biocompatible materials, such as Ni in nanowires and magnetic bearings, should be replaced with biocompatible magnetic materials, such as iron, or covered with materials innocuous to cells and bio molecules. Also, the method described above is suitable for single/few cell study in an in-vitro setting. It is not

applicable to in-vivo study. In terms of in-vivo applications, in this work, we found that the release rate of biochemicals can be controlled by mechanically rotating nanoparticles. If we want to control the release rate of chemicals delivered into a human body by nanoparticles, we should directly rotate those nanoparticles in-vivo by remotely applied electromagnetic fields. The integration of nanoparticles to a desired organism could be realized by the well-established site-specific bioconjugation technique.[102] A high-frequency AC field could be generated at a specific position by an endoscope-like device. All of these require extensive and careful investigation; especially the biocompatibility of high frequency **E**-fields of tens of kHz with a live organism is unknown. Overall, we demonstrated tunable biochemical release using nanomotors in a simple aqueous environment. Further experiments as discussed above are our next work to explore its usage in actual biosetting. If successful, the tunable release of biochemicals from nanomotors could be potentially pivotal for study of single cell stimulation, cell-cell communication, system biology, and drug delivery.

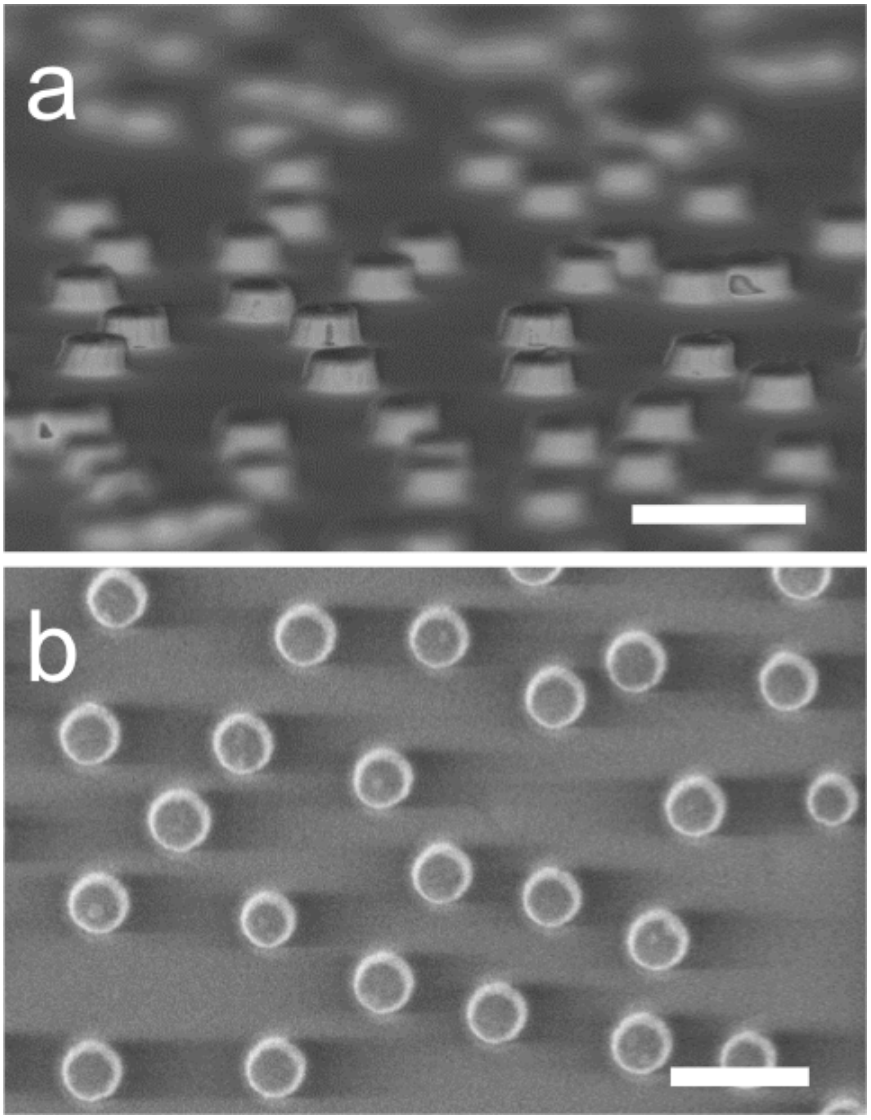

Figure 3.13: Wafer-scale fabrication of nanomagnets. (a) Side and (b) top view of arrays of nanomagnets (200 nm in diameter) for assembling of nanomotors close to any selected live cells cultured on the substrate. Scale bars: 500 nm.

3.3. CONCLUSION

In summary, we demonstrated innovative design, assembling and actuation of rotary NEMS devices utilizing a strategic bottom-up nano-assembly and manipulation

technique— the electric tweezers, which was reported previously. Ordered arrays of nanomotors can be efficiently assembled and synchronously rotated with controlled angle, speed, and chirality. The rotation speed can be at least 18,000 rpm, which is still not the limit. Various complex nanoscale forces and torques involved in the nanomotor system are quantitatively modeled and determined, which is critical for understanding, design, and actuation of various metallic NEMS devices. The nanomotors, with all dimensions smaller than 1 μm, can rotate continuously up to 15 hours for more than 240,000 cycles. They were demonstrated for controlled biochemical release in a simple non-biosetting, and presented a new mechanical approach for tuning releasing rate of biochemicals from nanoparticles. The innovations reported in this research could be of interest for NEMS, bioNEMS, microfluidics, and lab-on-a-chip architectures.

Chapter 4: Micromotors with Step-Motor Chracteristics

4.1. INTRODUCTION

Micro/Nanoelectromechanical systems (MEMS/NEMS) has attracted intense research interest for decades due to its promising applications across various research fields including electronics,[57,103] chemical and biomedical sensing, [100,104-106] and biochemical delivery.[13,85,96,107,108] Rotary nanomotors, a type of rotational NEMS devices, which can convert rotary motion into linear motion for powering and actuation, have attracted intense attention due to its critical role in advancing NEMS technology.[9,11,24,60,93,109]

In the previous chapter, an innovative type of rotary nanomotors have been bottom-up assembled from nanoscale building blocks by using the electric tweezers.[14] The nanomotors were assembled into arrays and rotated with highly controlled angle, speed (to at least 18,000 rpm) and chirality. They could be rotated continuously for 15 hours and applied in tunable biochemical release.[110] Although remarkably controllable and precise, the rotation speed of the nanomotors showed periodic fluctuation. We believe that the rotation speed fluctuation originated from the angle-dependent magnetic interactions between the rotors and bearing, which was used for the anchorage of the nanorotors. Therefore, it is highly desirable to eliminate the fluctuation of the interactions between the assembled components of the nanomotors for high performance in stability, controllability, and reliability.

In this chapter, we investigated the rotation dynamics of bottom-up assembled rotary motors by designing various configurations of magnetic interactions between the assembled sub-components. Magnetic components with desired moment, orientation, and

dimensions are successfully fabricated, which enabled distinct rotation behaviors from wobbling and self-rolling besides in-plane rotation to rotation at uniform speeds and stopping at designated angles, like step motors.

4.2. METHODS

The motors consist of nanowires, patterned nanomagnets, and quadrupole microelectrodes serving as rotors, bearings, and stators, respectively [Fig. 4.1(a)]. An AC **E**-field was applied to compel the motors to rotate *via* four AC electric voltages on a quadruple microelectrode with sequential 90° phase shifts.[11,14] To minimize the effect of Brownian motions on the rotation of motors and clearly understand the effect of magnetic interactions, we used nanowires with a length of ~10 – 7 μm and referred the devices as micromotors in this work, although the devices can be made at a nanoscale with all components less than 1 μm.[14]

Multilayer Au/Ni nanowires were fabricated by electrodeposition into nanoporous templates.[43] The magnetic strength and anisotropy of the nanowires were controlled by the geometry and total volume of the integrated magnetic segments in a blue false color in Fig. 4.1(b) and (c). For instance, the magnetic orientation of a nanowire with a 1-μm-long Ni segment is in the long direction of the nanowire [Fig. 4.1(b)], while that of a nanowire with a 100-nm-long Ni segment is in the transverse direction [Fig. 4.1(c)]. More scanning electron microscopy (SEM) characterizations and analysis of size and composition distributions of nanowires are provided in the supporting information [Fig. 4.2 and Table 4.1]

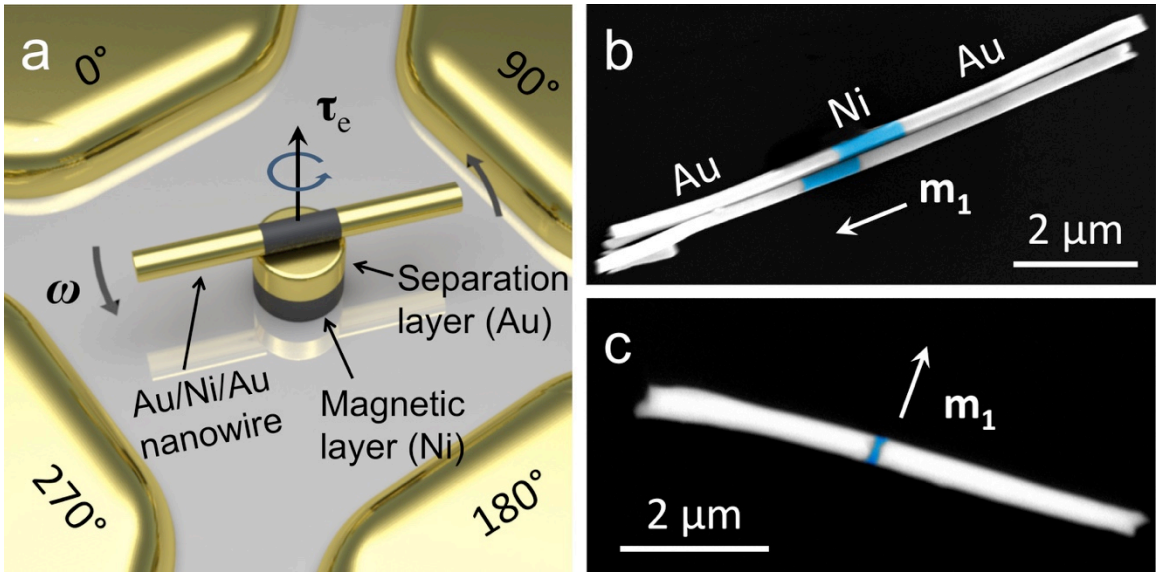

Figure 4.1: Structure of the nanomotor and the nanowire rotors. (a) Schematic diagram of a nanowire motor with a nanowire, magnetic bearing, and quadrupole electrodes as the rotor, bearing, and stator. (b and c) Scanning electron microscopy images of Au/Ni/Au nanowires with a (b) 1-µm- or (c) 100-nm-long Ni segment highlighted in blue. m_1 is the magnetic moment of the Ni segment of the nanowires.

Magnetic bearings with diameters of 200 nm to 2 µm are patterned in the center of the quadrupole microelectrodes by colloidal nanolithography[111] or electron-beam lithography as shown in Fig. 4.3 and Table 4.2. The magnetic bearings consist of a stack of thin films of N/M/Cr (6 nm), where N is a non-magnetic spacer layer for controlling the magnetic forces between the rotors and bearings. They are typically made of pure Au (100 nm) or Au (100 nm) coated with a thin layer of carbon (3 – 4 nm). M is a magnetic layer made of either Ni with in-plane anisotropy (80 nm in thickness, deposition rate < 0.5 Å/sec in electron-beam evaporation) or CoPt alloys with perpendicular magnetic anisotropy (PMA, 20 nm in thickness). In all of our experiments, the magnetic moment of the bearings was first demagnetized with gradually decaying alternating magnetic fields

and then re-magnetized at 1 Tesla for 50 seconds in the direction of magnetic anisotropy to achieve full saturation.

The micromotors were assembled by the electric tweezers.[12,47] In brief, by using the combined AC and DC **E**-fields, nanowires suspended in deionized (DI) water were manipulated in both the X and Y directions to the magnetic bearings. When in the vicinity of the magnetic bearings, they can be swiftly attracted and assembled atop of the bearings.[14,112] Here, the magnetic force between the magnetic elements in the rotors and bearings is controlled by the Au separation layers [Fig. 4.1(a)], thereto anchors the rotors on the bearings while still allowing the rotation. The rotation of the micromotors was captured by a digital camera equipped on an optical microscope operating at 50 – 60 frames per second (fps).

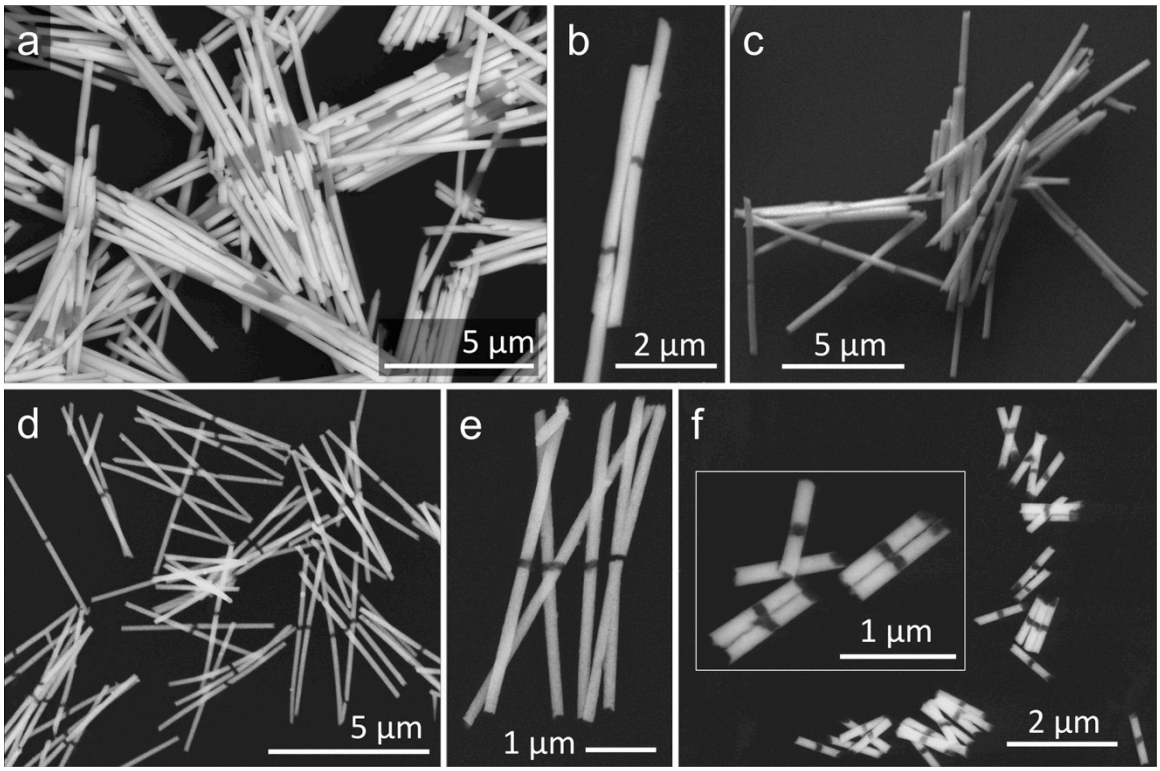

Figure 4.2: Scanning electron microscope (SEM) images of Au/Ni/Au nanowires working as rotors of the micro/nanomotors: (a) 4.5/1.0/4.5 µm in length and 300 nm in diameter, (b and c) 3.0/0.1/3.0 µm in length and 300 nm in diameter, (d and e) 2.5/0.1/2.5 µm in length and 180 nm in diameter, and (f) 400/100/400 nm in length and 180 nm in diameter with a close-up image (inset). Detailed dimensions and compositions are listed in Table 4.1.

Nanowires	**(a)**	**(b) and (c)**	**(d) and (e)**	**(f)**
Total length (µm)	9.627 (±0.761)	6.420 (±0.915)	4.971 (±0.191)	0.936 (±0.096)
Length of Ni segments (nm)	1010 (±79)	116 (±17)	86 (±14)	85 (±3)
Diameter (nm)	297 (±24)	295 (±39)	179 (±12)	159 (±5)

Table 4.1: Average length and diameter of the nanowires and their Ni segments shown in Figure 4.2. The values in parentheses are standard deviations.

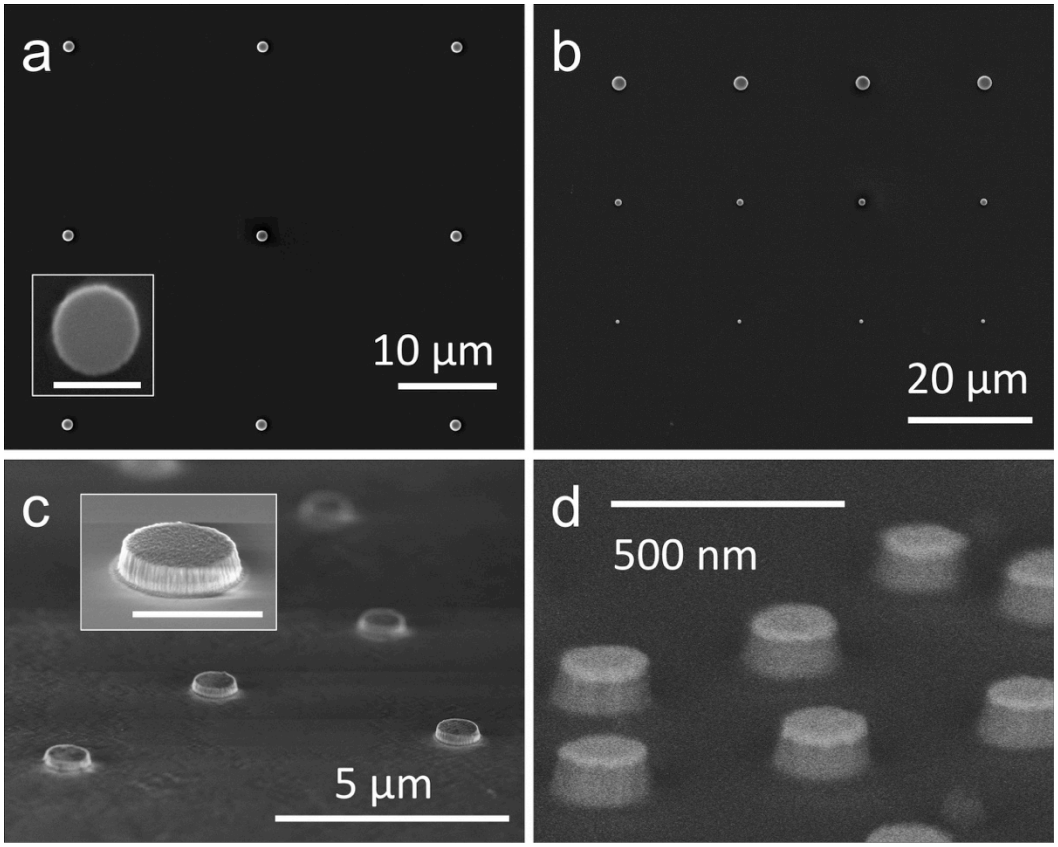

Figure 4.3: SEM images of multilayer Cr/Ni/Au patterned magnets fabricated using (a and b) e-beam lithography and (c and d) colloidal nanolithography: (a and c) 1-µm-diameter magnets with close-up images in the inset (scale bars: 1 µm); (b) 2-µm-, 1-µm-, and 500-nm-diameter magnets; and (d) 200 nm-diameter magnets. Size distribution of the magnets is provided in Table 4.2.

Patterned magnets	**(a) and (b)**			**(c) and (d)**	
Patterning method	E-beam lithography			Colloidal nanolithography	
Designed diameter	2 µm	1 µm	500 nm	1 µm	200 nm
Actual diameter (µm)	2.207 (±0.081)	1.087 (±0.058)	0.558 (±0.047)	0.997 (±0.030)	0.210 (±0.008)

Table 4.2: Average diameter of the multilayer Cr/Ni/Au magnets in Figure 4.3 serving as bearings for the micromotors. The numbers in parentheses are standard deviations.

4.3. RESULTS AND DISCUSSION

To investigate how the rotation dynamics are tuned by the magnetic interactions between the assembled components, we studied three primary configurations: (1) chopstick configuration: both magnetic moments of the nanowire and the bearing are parallel to the plane of rotation; (2) perpendicular configuration: both magnetic moments of the nanowire and the bearing are perpendicular to the plane of rotation; and (3) T configuration: magnetic moment of the nanowire is parallel, while that of the bearing is perpendicular, to the plane of rotation.

For the chopstick configuration [Fig. 4.4(a)], a micromotor made of a 4.5/1/4.5-μm-long Au/Ni/Au nanowire [Fig. 4.1(b)] and a 1-μm-diameter Ni bearing was assembled. Magnetic moment of the Ni segment (m_1) is along the long axis of the nanowire due to the shape anisotropy.[113] The Ni bearing exhibits a strong in-plane magnetic anisotropy [Fig. 4.4(b)] also due to shape anisotropy. In this configuration, the rotation speed of micromotors oscillated as a function of the angular position with a period of 360° [Fig. 4.4(c)]. Although the speed fluctuated periodically, the overall rotation was stable, since the center of the nanowire [Fig. 4.4(d)] and the instant center of rotation [Fig. 4.4(e)] barely moved apart from the center of the bearing. From this, it can be readily known that the nanowire rotated with both ends of the 1-μm-long Ni segment flushed with the edge of the 1-μm-diameter bearing, which resulted in balanced and symmetric rotation without significant lateral motion or wobbling [Fig. 4.4(f)].

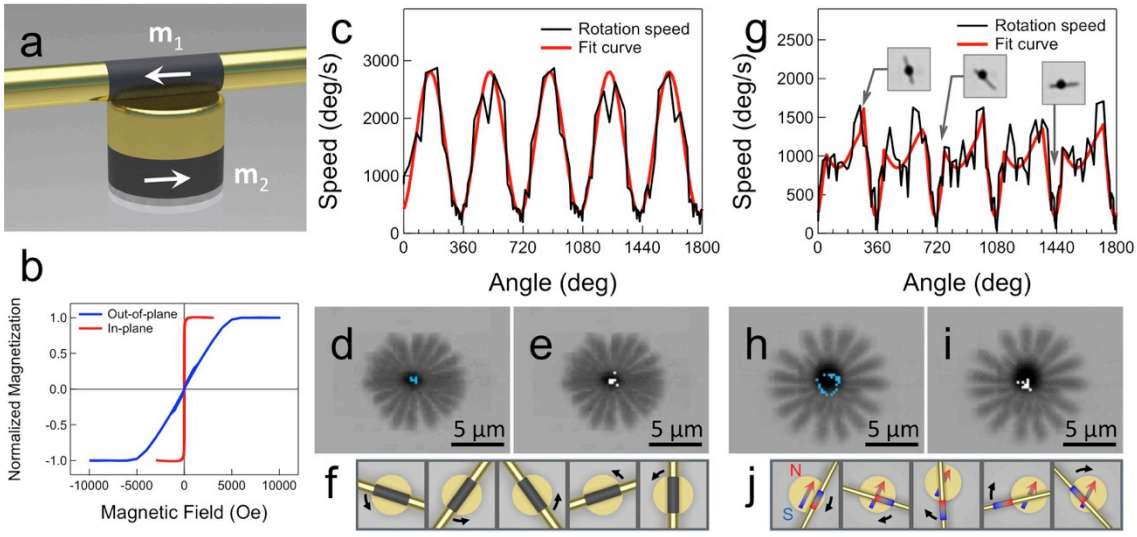

Figure 4.4: Characteristics of micromotors with the chopstick configuration. (a) Schematic diagram of a motor with the magnetic moment of the nanowire and the bearing parallel to the substrate. (b) Vibrating sample magnetometer (VSM) measurement showing the in-plane magnetization of a Ni thin film. (c - f) Rotation of a micromotor with a 1:1 ratio of the length of the Ni segment and diameter of the bearing: (c) rotation speed as a function of the angular position of the nanowire; (d) center of the nanowire rotor; (e) instant center of rotation; and (f) diagram of a nanowire rotating on the bearing. (g – j) Rotation of a micromotor with a 1:2 ratio of the length of the Ni segment and diameter of the bearing: (g) rotation speed as a function of the angular position of the nanowire; (h) center of the nanowire rotor; (i) instant center of rotation; and (j) diagram of a nanowire rotating on the bearing.

The periodic oscillation of rotation speed (ω) can be understood by the torque involved in the micromotors given by[14]

$$\tau_e + \tau_{e'} + \tau_\eta + \tau_M + \tau_f = 0 \tag{4.1}$$

where τ_η, τ_M, and τ_f are viscous drag, magnetic, and friction torques respectively. τ_e and $\tau_{e'}$ are torques due to interaction between the polarized nanowire and the external **E**-field (E) and that between the polarized nanowires and bearings, respectively. The detailed

modeling has been reported elsewhere and discussed here in brief: τ_e and $\tau_{e'}$ are torques both proportional to the square of the AC voltage V^2 and $\tau_\eta \propto \omega$,[81,82] therefore $\tau_e = aV^2$, $\tau_{e'} = bV^2$, and $\tau_\eta = D\omega$, where a, b, and D are constants. The magnetic torque (τ_M) is due to the magnetic interaction between the Ni segment in the nanowire rotor and the patterned magnetic bearing, which depends on the angle (Θ) between the magnetic moment of the nanowire m_1 (θ) and magnetic bearing m_2 (θ_m), given by $\Theta = \theta - \theta_m$. If we simplify the magnetic rotor and bearing as two magnetic dipoles separated at a distance x, the magnetic force (F_M) and torque (τ_M) exerted on the nanowire can be given by $F_M = 3\mu_0(m_1m_2 \cos \Theta)/(4\pi x^4)$ and $\tau_M = \mu_0(m_1m_2 \sin \Theta)/(4\pi x^3)$, respectively, where μ_0 is the magnetic permittivity of vacuum magnetic force. Therefore, it can be known that $\tau_M = d \sin \Theta$ and $\tau_f = e \cos \Theta + f$, where d, e, and f are constants. As a result, Eq. (4.1) can be rewritten as:

$$\omega(\theta) = \frac{d}{-D}\sin(\theta - \theta_m) + \frac{e}{-D}\cos(\theta - \theta_m) + \frac{(a+b)E^2+f}{-D} \qquad (4.2)$$

It is clear that the torques due to the magnetic interaction, such as τ_M and τ_f, induced the oscillation of the rotation speed. The observed angular dependence of rotation speed can be well fitted by Eq. (4.2) [red curve in Fig. 4.4(c)], which suggests the validity of our modeling.

Even at the simple chopstick configuration, it is interesting to know how the relative strength and dimensions of the assembled magnetic components can be used to tune the rotation dynamics of micromotors. In addition to the first case with the 1:1 dimension ratio, the magnetic components in the nanomotor were designed to have a 1:2 ratio, i.e., a 1-μm-long Ni segment in the rotor and 2-μm-diameter for the bearing. The same rotation periodicity of 360° can be observed as that of the motors discussed above

(dimension ratio 1:1), but a local minimum at ~180° with two asymmetric peaks emerged evidently [Fig. 4.4(g)]. It is also noticed that the center of the nanowire moved around forming a circle of ~ 2 μm in diameter [Fig. 4.4(h)], while the trajectory of the instant center of rotation is closely packed in a small area, both located at the lower half of the bearing [Fig. 4.4(i)]. After careful frame-by-frame image analysis, we found that the nanowire rotated with the edge of the Ni segment flushing with that of the magnetic bearing, but alternately staying atop and hanging over the side of the bearing [Fig. 4.4(j)]. This rotation behavior is a result of the minimization of the magnetic repulsive energy by having antiparallel magnetic configurations in a side-by-side or stacked configuration as shown in Fig. 4.4(j) (south and north poles (i) overlap; (ii) next to each other). Since the magnetic forces for these two antiparallel configurations are in opposite directions and distinct in strength, a rotation periodicity of ~180° and two asymmetric peaks can be observed. With the above understanding, we fitted the rotation speed using two sine waves with different amplitudes and phases (red and blue in Fig. 4.4(g)]. A much better fitting curve that matches the experiments can be obtained compared to that with a single sine wave.

Next, we further reduced the aspect ratio of the Ni segments inside the nanowires to form thin Ni disks (300 nm in diameter and 100 nm in thickness) and rotated them on 1-μm-diameter Ni bearings. Now the magnetic moments of the rotors are transverse to their long direction [Fig. 4.1(c)]. Different from the two aforediscussed parallel-configured micromotors in Fig. 4.4, a strong rotation periodicity of 180° was found [Fig. 4.5(a)]. Here none of the model introduced above can be used to fully understand the rotation behaviors of this configuration. Moreover, although the nanowire rotors wobbled on the bearings [Fig. 4.5(b) and (c)], it is difficult to conclude that the magnetic segment of the rotors hung over the side of the magnetic bearings as that in Fig. 4.4(j). With

careful analysis, we suggest that the 180° periodic oscillation originates from the self-rolling of the nanowires along the long direction of the nanowire during its in-plane rotation, which effectively changed the unstable repulsive magnetic configuration to a stable attractive magnetic configuration every 180° as shown in the schematic diagram of Fig. 4.5(d). It is also found that the rotation speed dropped abruptly [dotted line in Fig. 4.5(a)], while increased gradually [red line in Fig. 4.5(a)], which could be an evidence of the abrupt change in magnetic configuration induced by the self-rolling. Besides, the rotation speed fits well to the half of a sine wave from the negative peak to the positive peak, i.e., $\omega = A \sin(\theta - \phi)$ at $-\pi/2 + \phi \leq \theta \leq \pi/2 + \phi$, repeating every 180° [red curve in Fig. 4.5(a)]. It can also support the self-rolling mechanism by which the magnetic orientation of the Ni segment of the nanowire is flipped and set to 0 relative to that of the bearing every 180°. As a result, this kind of motors has two syngenetic periodic rotations, one is along the direction of nanowires and the other is in the horizontal plane.

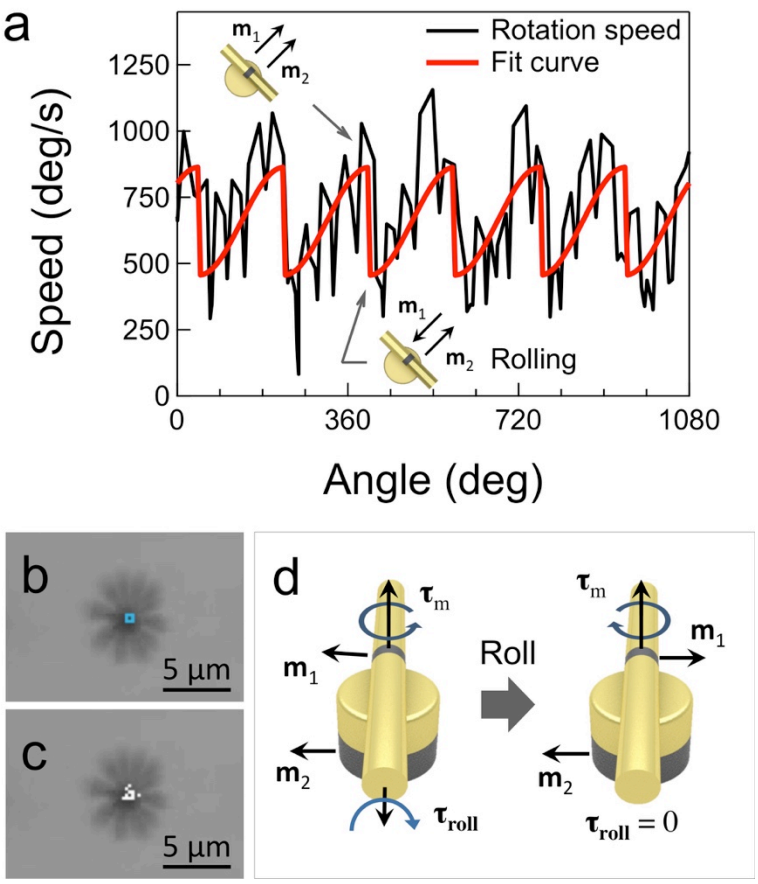

Figure 4.5: Rotation dynamics of a micromotor with a thin Ni segment of 100 nm in thickness anchoring on a Ni bearing of 1 μm in diameter. (A) Rotation speed as a function of angle. (B) The center of the nanowire rotor and (C) the instant center of rotation. (D) Schematic diagrams showing the rolling of the nanowire rotor along the long axis, which results in antiparallel alignment of the magnetic moments of the rotor and bearing.

Note that the fit-curves in Fig. 4.4(g) and Fig. 4.5(a) have certain deviation from the experimental curves. It can be attributed to the more complex rotation dynamics of the nanomotors, whose motion trajectories could slightly change in each cycle and result in noises and deviations among different cycles. It can be also because the fitted curves are based on a simple magnetic dipole-dipole model, without consideration of the position dependent magnetic force at different locations on the bearings when the rotors

are rotating atop of the bearings for both cases in Fig. 4.4(g) and 4.5(a). Also, we used an effective distance between the magnetic dipoles in the model for Fig. 4.4(g) when the magnetic segment of the rotor was hanging over the side of the bearing, without further considering the complex temporal distance change. Nevertheless, the fit-curves match the data for both cases in large, which supports the feasibility of our analysis and understanding of the behavior of the motors.

The most interesting magnetic configuration we examined is the perpendicular configuration, where both the magnetic moments of the nanowires and bearings are perpendicular to the plane of rotation [Fig. 4.6(a)]. To construct such micromotors, we used nanowires with transverse magnetic anisotropy [Fig. 4.1(c)] and bearings made of PMA alloys with strong perpendicular magnetic anisotropy as shown in the polar Kerr measurement [Fig. 4.6(b), 1 μm to 200 nm in diameter]. Since m_1 and m_2 are parallel to each other and both of them are perpendicular to the rotation plane, the magnetic force, given by $F_M = 3\mu_0(m_1m_2)/(2\pi x^4)$, as well as the resulting frictional torque remain constant regardless of the angular position of the nanowire. Also the angle-dependent magnetic torque vanishes from Eq. (4.1), which is distinctly different from that of the parallel configuration. As a result, the motors can rotate with uniform speed without observable periodic oscillation [Fig. 4.6(c)], even at high voltages [Fig. 4.6(d)]. They can be compelled to rotate and stop at designated angles, very much like step motors, by simply controlling the intensity and pulse duration of the applied **E**-field [Fig. 4.6(e) and Table 4.3]. This type of micromotors could be more advantageous for applications due to the uniform rotation speeds, controlled angular positions, and high stability, compared to those with chopstick configurations. Note that the chopstick-configured micromotors always restore to align with the magnetic moment of the bearing after removal of the **E**-

field, regardless of the angular position set by the **E**-field, even for those motors whose dimensions are all smaller than 1 μm.

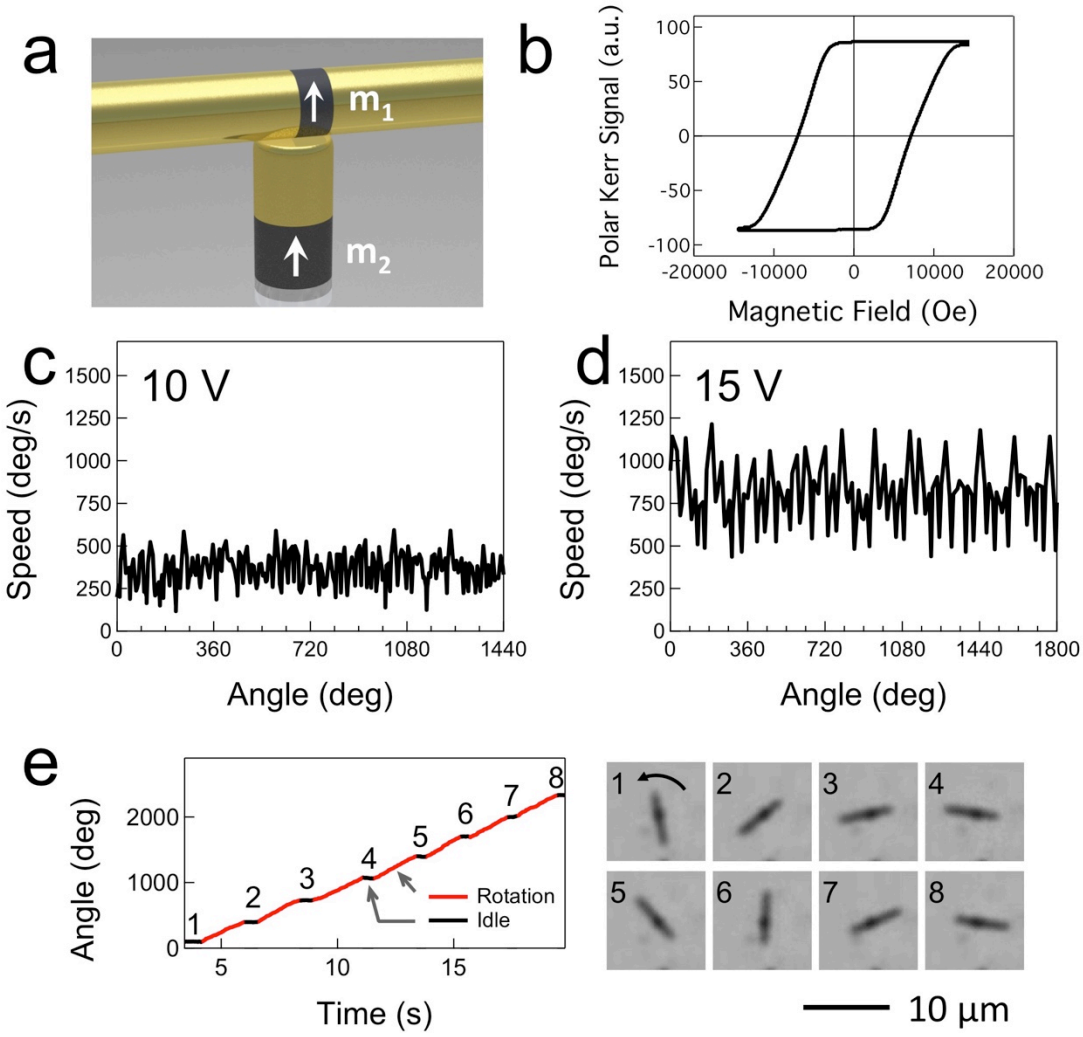

Figure 4.6: Characterization of a nanowire with the perpendicular magnetic configuration (100-nm-long Ni segment in the rotor and PMA bearing with 1 μm in diameter) (a) Schematic diagram of the magnetic configuration of the micromotor. (b) Polar Kerr measurement in the vertical direction showing the perpendicular magnetic anisotropy of the PMA alloy thin film. (c – d) Rotation speed as a function of angle at various voltages, e.g., (c) 10 V and (d) 15 V. (e) Rotation of a micromotor with controlled angular displacement *versus* time, resembling step motors, and snap shots of the micromotor at the designated angular displacement.

We also note that the angular step of the nanowire rotors has a relative standard deviation (%RSD) of 3.7% – 20.0%. The overall %RSD decreases with the increase of the designed angular step size in general [Table 4.3]. The standard deviation of the rotation angle remains largely the same when the preset angle is less than 190° and approximately doubled when the rotation angle is 260° and above. This variation in the angular displacement can be attributed to the imperfect synchronization of the four AC voltages applied to the electrodes. For the rotation with larger angular displacement, the non-uniform interface between a bearing and a rotor and the Brownian motion can also affect the rotation significantly, which makes the angular displacement more deviate. Therefore, the angular control precision of the motors is expected to be well improved by refining the control program and circuit, enhancing the surface smoothness of the bearings, and implementing mechanisms to counter the Brownian motions of the nanorotors.[8]

Micromotor		**1**	**2**	**3**	**4**	**5**	**6**	**7**	**8**	**9**
Angular displacement (°)	**AVG**	48.5	54.8	65.1	96	191.8	259.8	325.6	377.4	595.3
	SD (%RSD)	±9.7 (±20%)	±8.8 (±16%)	±9.2 (±14%)	±12.2 (±13%)	±9.6 (±5%)	±19.1 (±7.4%)	±18.5 (±5.7%)	±13.8 (±3.7%)	±22.4 (±3.8%)

Table 4.3: Average (AVG), standard deviation (SD), and relative standard deviation (%RSD) of the angular displacement of micromotors rotating at different AC voltages for different durations with a perpendicular magnetic configuration.

The last type of motor has a "T" shaped magnetic configuration [Fig. 4.7(a)]. The nanomotor is built from a nanowire rotor with a 1-μm-long Ni segment whose magnetic moment is parallel to the plane of rotation, and a PMA bearing with moment

perpendicular to the plane of rotation. The magnetic configuration is in a "T" shape. Under this condition, the magnetic torque and force can be calculated to be $F_M \propto (\mu_0 m_1 m_2)/(\pi x^4)$ and $\tau_M \propto (\mu_0 m_1 m_2)/(\pi x^3)$, respectively, both of which are independent of the angular position of the nanowire. As a result, this type of micromotor shows a similar rotation behavior with that of aforediscussed perpendicularly configured micromotors. The rotation speed is highly uniform [Fig. 4.7(b)] and the angular position of the rotor can be controlled with arbitrary angular steps [Fig. 4.7(c)].

Finally, the characteristic rotation speed spectra of all the different types of micromotors were processed with Fourier transformation. It can be found that all the parallel configured micromotors showed strong periodicity of 360° and/or 180°, agreeing with our conclusions [Fig. 4.8(a) – (c)]. In comparison, the typical Fourier transformation of the perpendicular- and T-configured micromotors is nearly a flat line, without any clear periodicity [Fig. 4.8(d) and (e)]. This corroborates the successful achievement of the micromotors with uniform rotating speeds by manipulating magnetic interactions between assembled components.

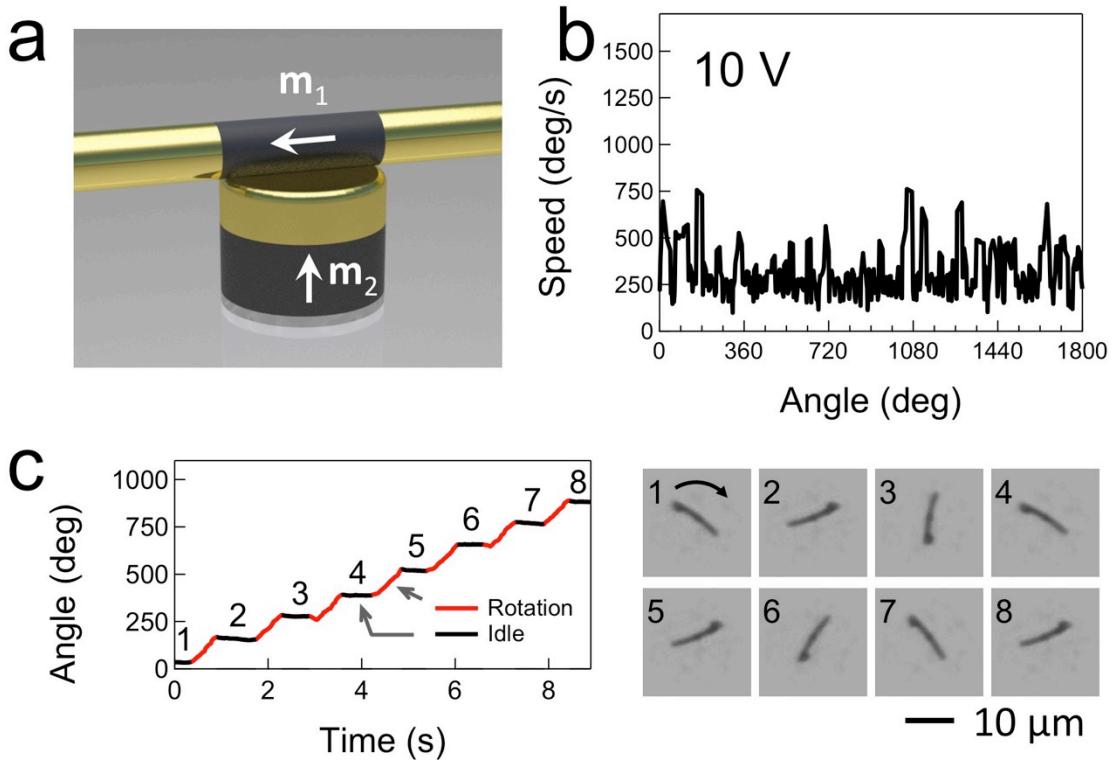

Figure 4.7: Characteristics of a micromotor with a "T" shaped magnetic configuration with a 1-µm-long Ni segment in the rotor assembled on a PMA bearing of 1 µm in diameter. (a) Schematic diagram of the motor. (b) Rotation speed as a function of angular position. (c) Angular position of a micromotor with controlled angular displacement as a function of time and the enhanced snapshots of the micromotor at the idle position indicated in the angle-time plot.

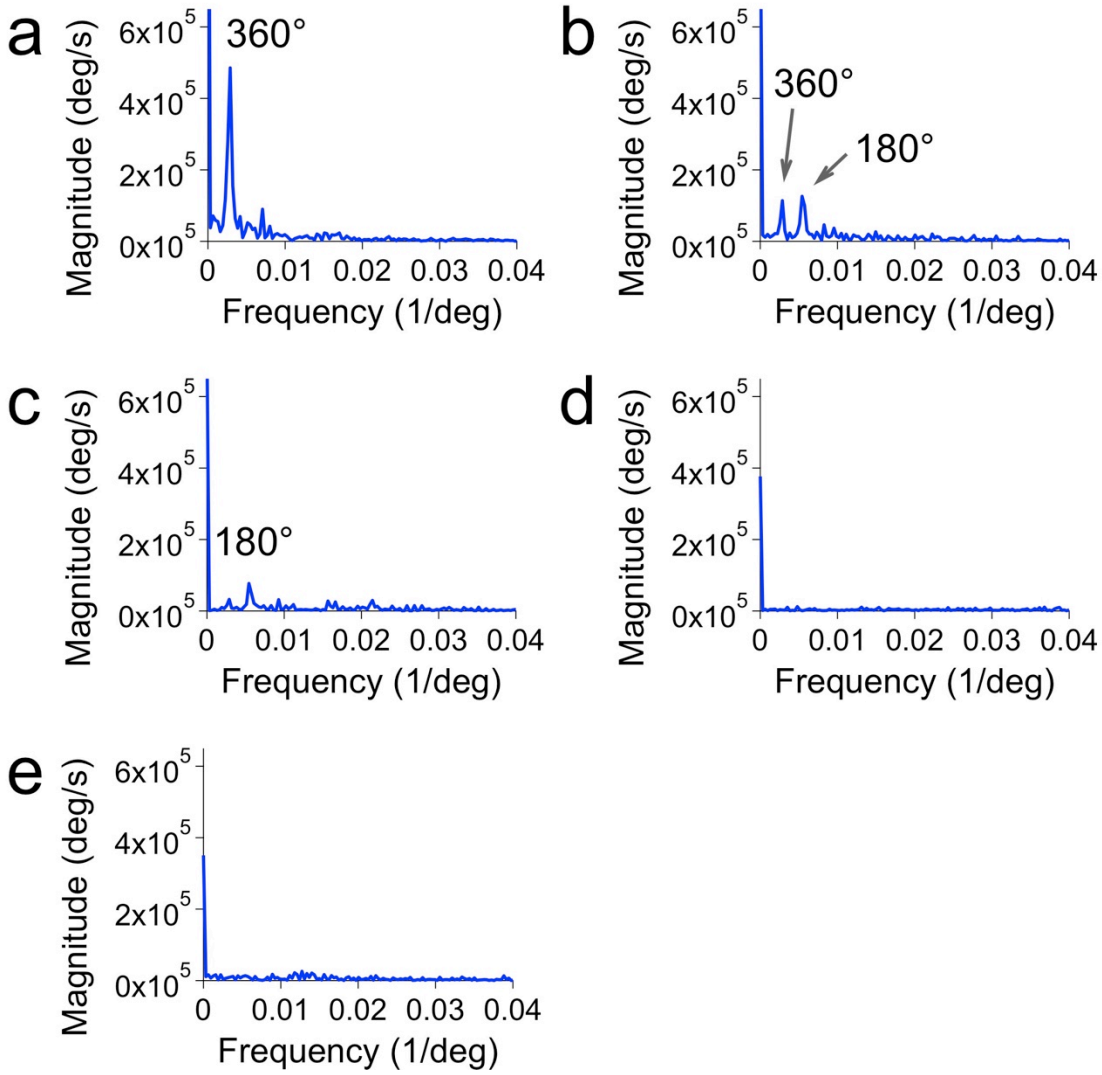

Figure 4.8: Fourier transforms of rotation speed *versus* time of micromotors with different magnetic configurations. (a) Chopstick configuration with a 1-μm-long Ni segment in the rotor on a Ni bearing of 1 μm in diameter. (b) Chopstick configuration with a 1-μm-long Ni segment in the rotor on a Ni bearing of 2 μm in diameter. (c) Chopstick configuration with a 100-nm-long Ni segment in the rotor on a Ni bearing of 1 μm in diameter. (d) Perpendicular configuration with a 100-nm-long Ni segment in the rotor on a PMA bearing of 1 μm in diameter. (e) T-shaped configuration with a 1-μm-long Ni segment in the rotor on a PMA bearing of 1 μm in diameter.

4.4. CONCLUSION

In summary, we investigated rotation dynamics of bottom-up assembled rotary micromotors by tuning the magnetic interactions among different assembled nanoentities. Various magnetic configurations were designed and successfully implemented with controlled strength, orientation, and dimensions, which resulted in distinct rotation behaviors including repeatable wobbling and self-rolling in addition to in-plane rotation. We understood the rotation behaviors by modeling the magnetic interactions. With these understanding, high-performance micromotors have been rationally designed and successfully achieved, where the micromotors rotate at uniform speeds and position at desired angles, resembling step motors. Our findings could assist the development of nanomotors with desirable performances for various applications and impact research areas including NEMS, microfluidics, and nanobiotechnology.

Chapter 5: Bioinspired Micromotors for Microfluidic Applications

5.1. INTRODUCTION

Equipped with rotors with different shape, size, and functionality, the micro/nanomachines can be used for many different applications. For instance, in the previous chapter, a nanomotor comprised of a plasmonically active rotor with its surface densely coated with Ag nanoparticles was used for tunable release and real time detection of biochemical substances.[14,110] The fabrication processes of nanoparticles and one-dimensional nanoentities have been well established and they can be facilely synthesized with controlled dimensions and chemical, mechanical, optical, and electromagnetic properties.[42] In contrast, it is arduous to obtain three-dimensional nano/microstructures with complex geometries, which usually requires significant efforts, cost, and sophisticated equipment.

In nature, biological systems have created delicate and refined three-dimensional nanostructures ranging from the superhydrophobic surfaces of lotus leaves[114] to the adhesive setae of geckos[115] and the iridescent wings of morpho butterflies,[116] which have inspired researchers to directly utilize or replicate those structures for various applications.[117-123] Diatoms, which are unicellular photosynthetic algae, are one of these examples. They have silica frustules with ordered micro/nanopores. Owing to the size and arrangement of the pores in silica structures, diatom frustules have been used for optical applications and biochemical detection with proper treatments and functionalization.[124-129]

In this chapter, we assembled micromotors using diatom frustules as rotors and demonstrated their rotation for microfluidic applications. Rotors were prepared with

porous cylindrical diatom frustules coated with ferromagnetic metal layers and magnetically assembled on patterned micromagnets with electric or magnetic manipulation techniques. We also investigated their dynamics in various circumstances and found such three-dimensional porous microstructures could stir and agitate the surrounding liquid medium more efficiently than simple nanowires, which indicates their great potential for applications as microfluidic actuators, e.g., microfluidic mixers.

5.2. METHODS

For this study, diatom frustules were obtained from commercially available diatomaceous earth powder. They have been widely used as health supplements for people and live stock, as well as insecticides for organic gardening. The small amount of diatom powder was mixed with deionized (DI) water. Since the as-obtained diatom powders contain impurities and have a wide range of size distribution, small particles as well as broken pieces of diatom frustules were removed through multistep filtration with filter papers with a nominal pore size ~50 μm. The remaining diatom frustules were collected and sequentially cleaned and rinsed with 2-propanol (IPA), acetone, and DI water with a vortex mixer more than three times [Fig. 5.1(a)]. Then, the suspension was spread and dried on a silicon wafer before it was loaded into an e-beam evaporator. Cr, Ni, and Au thin films were deposited to make the diatom frustules magnetically active so that they could be facilely manipulated with external magnetic fields and assembled for NEMS devices. Note that the Au thin film as a passivation layer prevents the magnetic Ni layer from directly contacting with the adjacent diatom frustules and the substrate. As a result, the aggregation of diatom frustules was minimized. The metal-coated diatoms on the Si wafer were sonicated, collected, and suspended in DI water and cleaned and rinsed

with IPA, acetone, and DI water [Fig. 5.1(b)]. Although not fully covered with the metal thin films, the frustules had ferromagnetization and responded well to the external magnetic field. Through the simple procedures mentioned above, either non-ferromagnetic or ferromagnetic diatoms with different sizes and shapes can be efficiently prepared for NEMS actuators. Owing to the natural abundance and low cost ($10 for 10 lb.), they could be readily scaled up for mass production.

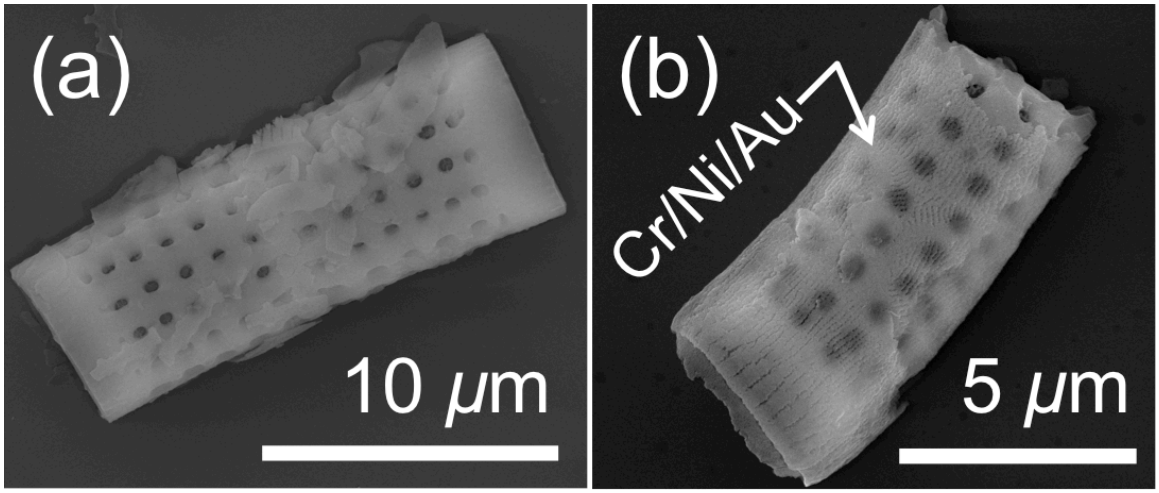

Figure 5.1. Scanning electron microscope (SEM) images of (a) an as-obtained diatom frustule and (b) a Cr/Ni/Au-deposited diatom frustule.

5.3. RESULTS AND DISCUSSION

Among various species of diatoms with different shapes and sizes in the mixture, we used cylindrical ones, e.g., *Aulacoseira ambigua* and *Aulacoseira lirata*, ranging 15 – 25 μm in length and 10 – 15 μm in diameter. Both magnetic and nonmagnetic frustules were precisely manipulated by the electric tweezers equipped with quadrupole microelectrodes, which generated either two orthogonal DC and AC **E**-fields or a rotating

AC **E**-field for translational or rotational motion of diatom frustules, respectively [Fig. 5.2(a)].[11,12,47] As previously reported, small particles suspended in a liquid medium move when **E**-fields are applied.[82] Under a uniform DC **E**-field $\mathbf{E}_{DC}$, particles with a charge q are transported along the field by the electrophoretic (EP) force, $\mathbf{F}_{EP} = q\mathbf{E}_{DC}$. On the other hand, in a uniform AC **E**-field $\mathbf{E}_{AC}$, dielectrophoresis (DEP) dominates motion of particles with dipole moment **p**. Although there is no net DEP force because the **E**-field gradient $\nabla\mathbf{E} = 0$, particles receive torque of $\boldsymbol{\tau}_e = \mathbf{p}\times\mathbf{E}_{AC}$ and are aligned parallel to the **E**-field. By the same token, in a rotating AC **E**-field created by four AC voltages applied to quadrupole microelectrodes with sequential 90° phase shift, nanoparticles can be rotated continuously.

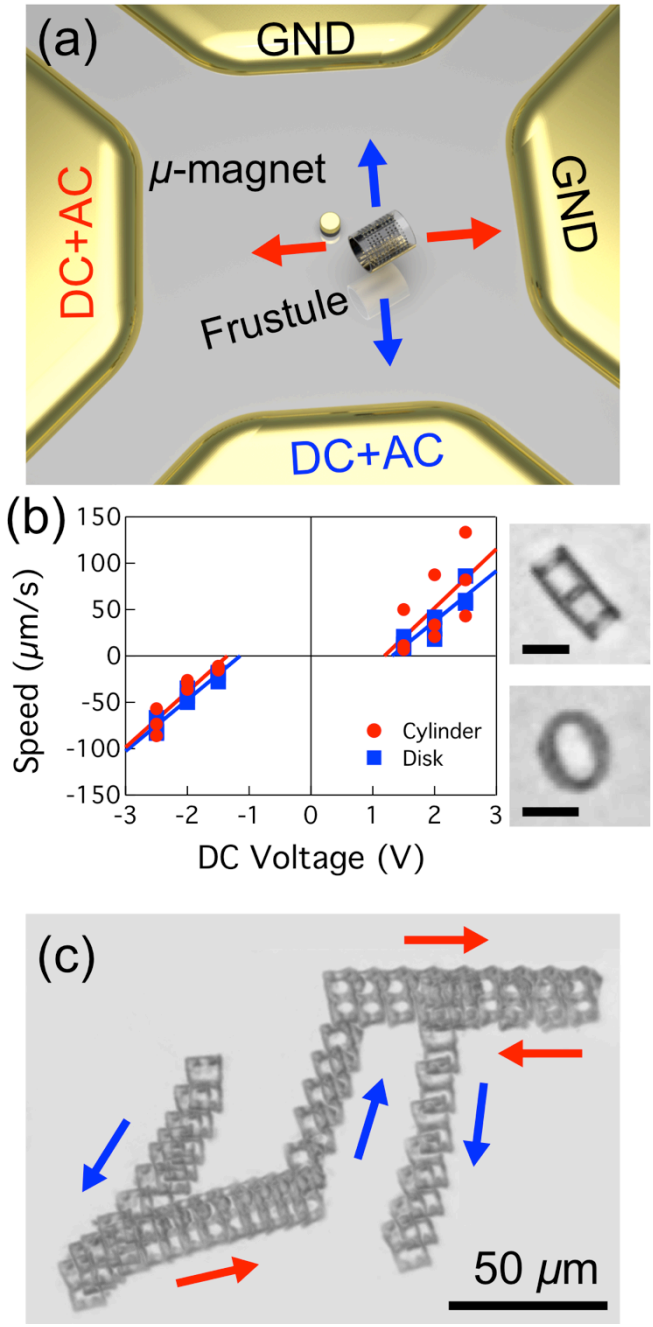

Figure 5.2. (a) Illustration of the electric tweezers with two orthogonal sets of parallel microelectrodes for the manipulation of diatom frustules. (b) Velocity of diatom frustules is proportional to DC voltages. Optical microscopy images of diatom frustules in cylindrical or disk shapes. Scale bars: 10 μm. (c) Trajectory of a diatom frustule manipulated by the electric tweezers to spell "UT."

Diatom frustules, either lying horizontally or standing vertically [Fig. 5.2(b)], were manipulated with the mechanisms discussed above. Assuming that EP force F_{EP} and drag force F_{η} affect their linear motion in a liquid medium, the terminal speed of a frustule v would be linearly proportional to E_{DC} as $F_{EP} = F_{\eta}$. As expected, diatom frustules moved faster with DC voltages applied to a set of parallel electrodes with fixed gap distance and the polarity of the DC voltages determined the moving direction. In this manner, the moving speed and direction could be precisely controlled with applied DC voltage V_{DC} regardless of their shapes, dimensions, and postures, although V_{DC} required for each frustules to get the same speed varied due to different surface charges and dimension of frustules influencing the drag force [Fig. 5.2(b)]. With two sets of parallel electrodes, **E**-fields could be applied in two orthogonal directions and the motion of the frustules was separately controlled in each direction. Sequentially applying **E**-fields in either direction for controlled duration, we could compel the frustules to move along the programmed path and even spell letters [Fig. 5.2(c)]. Although the motion of the diatom frustule could be precisely controlled, its trajectory was not perfect, possibly due to the spatially uneven sticking issue of the substrate, which could disturb the motion. Note that the diatom frustules of our interest were randomly oriented rather than aligned along AC **E**-fields while driven with DC **E**-fields. This could be due to the low electric polarizability of the SiO_2 diatom as well as the low aspect ratios, which resulted in the small dipole moment and thus low alignment electric torques.

Rotation of diatom frustules is critical for various MEMS and microfluidic applications and it is worth investigating their electrorotation characteristics. Diatom frustules in both cylindrical and disk shapes were tested and successfully driven to rotate in AC **E**-fields [Fig. 5.3(a) and (b)]. Rotation speed ω increased with the applied AC voltages and rotation direction, either clockwise (cw) or counterclockwise (ccw), swiftly

switched depending on the AC phase sequence [Fig. 5.3(c)]. As already revealed in NEMS devices using nanowires and nanotubes as components,[11,14,15,49,109] the rotation speed ω of diatom frustules, which were nonspherical particles, was proportional to the square of the AC voltage V [Fig. 5.3(d)]:

$$\omega \propto \frac{\varepsilon_m r^2 V^2}{\eta l^2} \mathrm{Im}(K) \tag{5.1}$$

where ε_m and η are the permittivity and the viscosity of the liquid medium, r and l are the diameter and length of the particle, and Im(K) is the imaginary part of the Clausius-Mossotti factor, respectively.

From Eq. (5.1), it could be inferred that the rotation speed also varies with AC frequency f_{AC} because of the frequency dependence of the Clausius-Mossotti factor:

$$\mathrm{Im}(K) = \frac{\varepsilon_p \sigma_m - \varepsilon_m \sigma_p}{(2\pi f_{AC})\left[\left(\varepsilon_m + L\varepsilon_p - L\varepsilon_m\right)^2 + \frac{1}{(2\pi f_{AC})^2}\left(\sigma_m + L\sigma_p - L\sigma_m\right)^2\right]} \tag{5.2}$$

where σ_i and ε_i denote the conductivity and the permittivity of the particle and the medium with the subscript $i = p$ or m, respectively, and L is the depolarization factor along the long axis of the particle.[49,82,109] It was experimentally found that the rotation speed of diatom frustules monotonically increased up to a certain frequency ~300 – 500 kHz and then decreased, although the rotation speed of the diatoms was different depending on their shape and dimension. These results are similar to those of SiO_2 nanowires and nanotubes reported previously, which is consistent with the composition of the diatom frustules considered.[127]

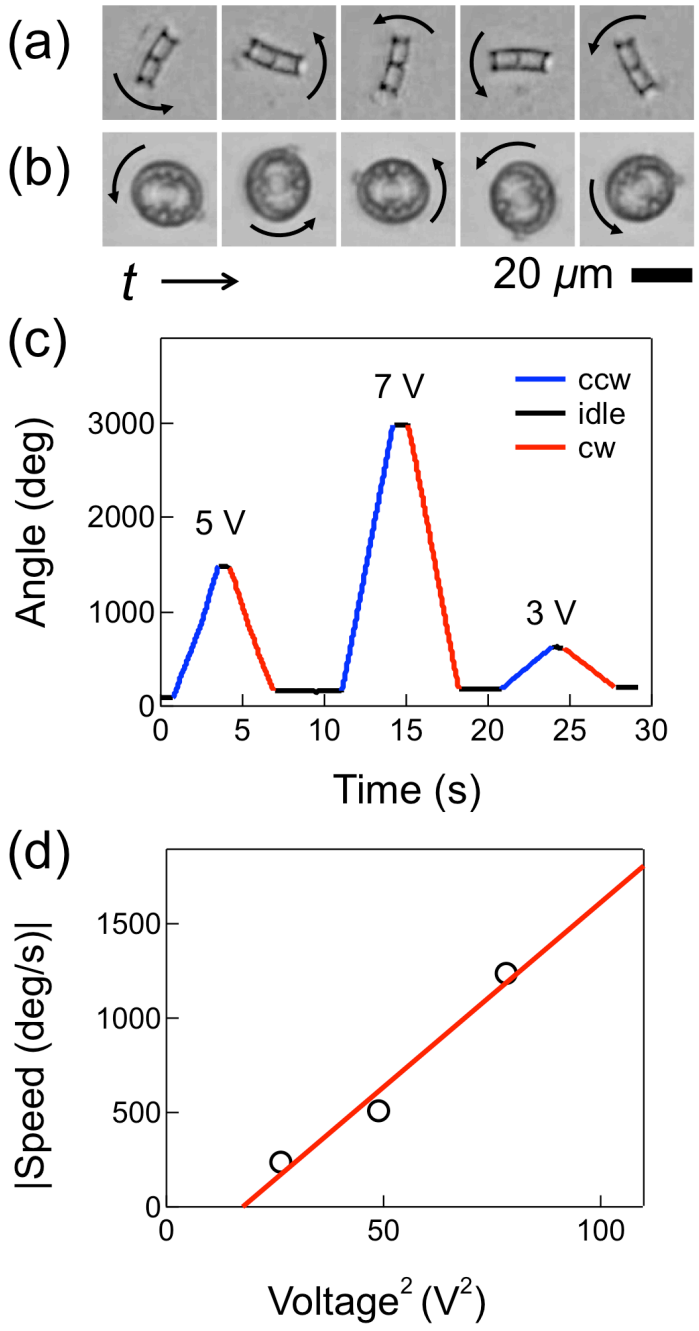

Figure 5.3. (a and b) Sequential optical microscopy images of rotating diatom frustules in (a) cylindrical and (b) disk shapes. (c) Accumulative angle of a diatom frustule rotating clockwise (cw) and counterclockwise (ccw) at different speeds depending on the applied AC voltage. (d) Rotation speed of a diatom frustule linearly increasing with the square of the applied AC voltage.

In order to rotate the diatoms at fixed locations, site-specific assembly and actuation is important. Using patterned micromagnets and diatom frustules with magnetic coating, we magnetically assembled the rotary micromotor. The 6/80/100-nm-thick Cr/Ni/Au micromagnets with different diameters ranging 1 – 5 μm were fabricated via either photolithography or E-beam lithography followed by E-beam evaporation on the glass substrate with predefined microelectrodes. The suspension of diatom frustules coated with 3/40/25-nm-thick Cr/Ni/Au thin films [Fig. 5.1(b)] was dispersed over the magnets and electrodes and manipulated by the electric tweezers. Responses of the metal-coated diatom frustules to uniform DC and AC **E**-fields were similar to those of the pure diatom frustules [Fig. 5.2(b)]. Their translation speed linearly increased with DC voltages and the moving direction was fully controllable with two orthogonal **E**-fields. Using the electric tweezers, we could deliver metal-coated diatom frustules to patterned micromagnets. When close to the micromagnets, the frustules were magnetically attracted and attached to the micromagnets [Fig. 5.4(a)].

Similar to the pure rotating diatom frustules [Fig. 5.3(c) and (d)], metal-coated diatoms rotated faster at high AC voltages with a quadratic dependence and switched their rotation direction upon reversing the phase sequence. However, unlike pure diatom frustules, metal-coated diatom frustules changed their rotation direction depending on the AC frequency [Fig. 5.4(b)]. While rotating in the same direction as the metallic nanowires at low frequencies up to ~100 kHz, the metal-coated diatom frustules reversed the rotation and followed the pure diatoms at high frequencies. Similar phenomena were previously reported with multiwall carbon nanotubes (MWCNT) and semiconducting nanowires, e.g., Si and ZnO nanowires, whose charge relaxation time ($\tau_p = \varepsilon/\sigma$) changes with the AC frequency due to conductivity change.[49] In comparison, the metallic

nanowires and the pure diatoms maintained their rotation direction, either cw or ccw, over the whole range of AC frequencies from 1 kHz to 2 MHz [Fig. 5.4(b)].

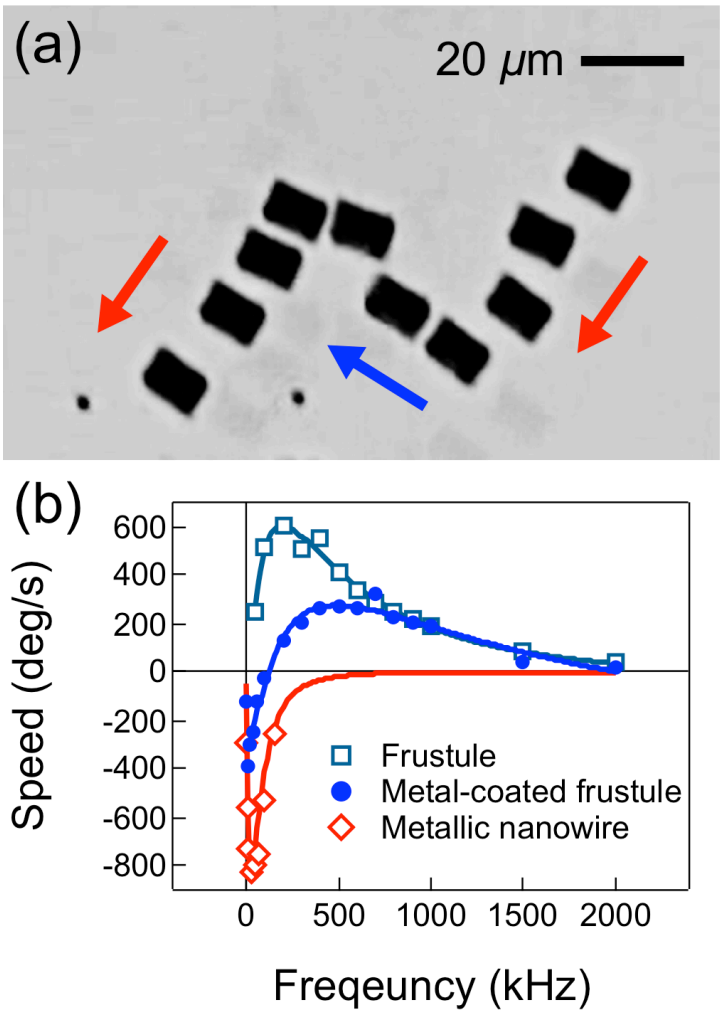

Figure 5.4. (a) Overlaid sequential micrographs of the assembly of a Cr/Ni/Au-coated diatom frustule and a patterned micromagnet using the electric tweezers. (b) Rotation speed of metallic nanowires (red, diamond), diatom frustules with (turquoise, squares) or without (blue, dots) Cr/Ni/Au layers. In the same rotating AC **E**-field, metallic nanowires and diatom frustules rotated in opposite directions, while metal-coated diatom frustules changed their rotation direction depending on the AC frequency.

An assembled diatom frustule on a micromagnet readily worked as a rotary MEMS actuator. It was even possible to assemble and simultaneously rotate multiple micromotors in an ordered array [Fig. 5.5(a)]. Arrays of micromotors could cover larger areas and generate more power than a single micromotor, which would be useful for practical applications. A micromotor had a top rotation speed over 2800 rpm at 17 V/ 20 kHz AC voltages applied to the electrodes with 150 μm gap distances [Fig. 5.5(b)] and continuously rotated for ~11.5 minutes until the diatom frustule rotor disassembled from the micromagnet [Fig. 5.5(c)]. The disassembling of the diatom could be due to unexpected perturbation in the liquid medium or electric fields and more investigations are required to enhance the stability and lifetime. All of these characteristics are critical for practical applications and make diatom frustule micromotors promising, although improvement is required.

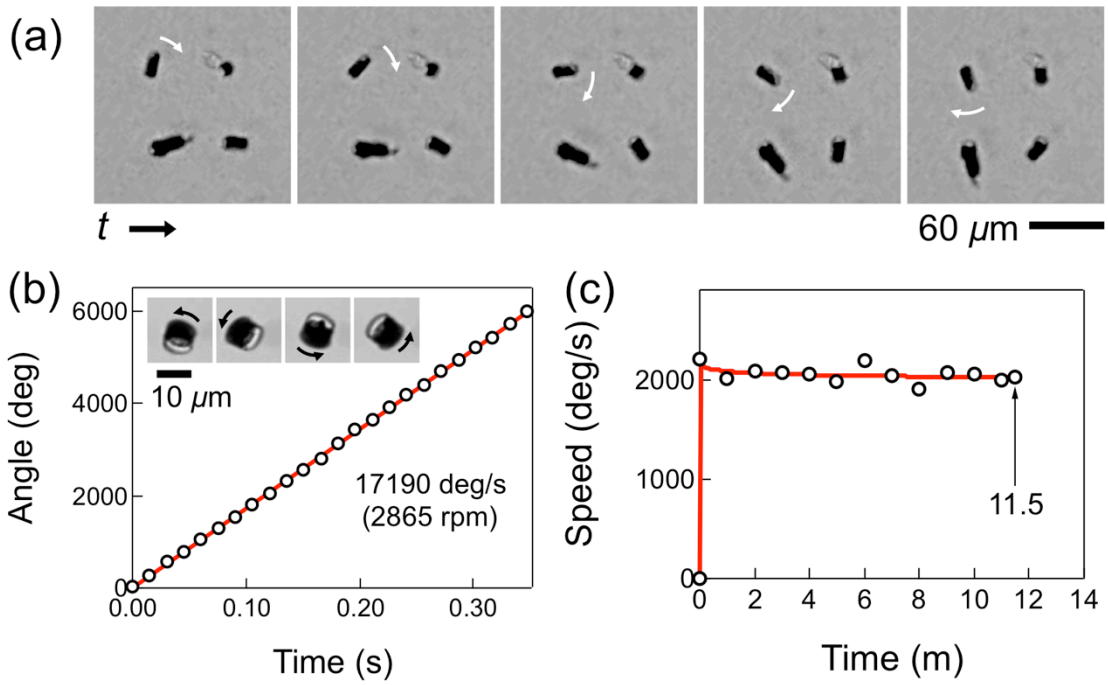

Figure 5.5. (a) Multiple diatom frustule motors rotating simultaneously in a 2×2 array. (b) Accumulative angle of the fastest diatom frustule motor we have ever achieved (inset: sequential micrographs of the motor). (c) Rotation speed of a diatom frustule motor continuously rotating for ~11.5 minutes before the motor disassembled.

Finally, we demonstrated the rotation of diatom frustule micromotors in a microfluidic channel. A SU-8 microchannel (~200 μm wide and ~50 μm deep) was patterned on a substrate with microelectrodes and 4-μm-diameter magnets via photolithography [Fig. 5.6(a) and (b)]. A chamber sealed with a PDMS well and a cover glass was formed atop of the microchannel and filled with the suspension containing Cr/Ni/Au-coated diatom frustules. Since the electric tweezers were effective only in a limited area surrounded by the microelectrodes, we used the magnetic field gradient generated by a neodymium magnet for the manipulation of the diatom frustules suspended in a liquid medium. When moved to the vicinity of a magnet, a Cr/Ni/Au-

coated diatom frustule was attracted and attached to the magnet and we could finally rotate an array of diatom frustule motors in a controlled manner [Fig. 5.6(a) – (c)].

In order to study the velocity distribution of the flow field, velocity contours and velocity vectors were generated from the two-dimensional simulations using ANSYS Fluent 15.0 (ANSYS, Inc., Canonsburg, PA). The velocity of the flow field in a microchannel (200 μm wide and 400 μm long) was calculated with the rotating nanowire (10 μm in length and 300 nm in diameter), solid cylinder (25 μm in length and 12 μm in diameter), or porous hollow cylinder (the same dimensions as the solid cylinder) emulating a diatom frustule [Fig. 5.6(d)]. The porous hollow cylinder had a shell thickness of 500 nm with nanopores 500 nm in diameter. To simplify the simulation, we used a two-dimensional cross sectional model with 16 nanopores. While the smallest mesh cells for the nanowire were 10 nm in length, those for the porous hollow cylinder were 20nm in length. The meshes were generated with the Sliding Meshed Method so that the meshes surrounding the rotors followed their rotation. The flow at the microchannel inlet was set 500 μm/s and the rotational speed in all three cases was 300 rad/s ≈ 2865 rpm. The Reynolds number in the systems was calculated to be around the magnitude of 0.1, four orders smaller than the critical Reynolds number. The solver was set to be transient (0.0004s each time step, 10 time steps in total) and pressure based and the Laminar model was applied. The solid and porous cylinders generated much stronger velocity fields than the nanowire due to their large dimensions [Fig. 5.6(d)]. The area of the high velocity region with the porous hollow cylinder was even larger than that with the solid cylinder, which indicates the porous structure of diatom frustules could drag the surrounding fluid more efficiently and have huge potential for microfluidics, e.g., active microfluidic mixers.

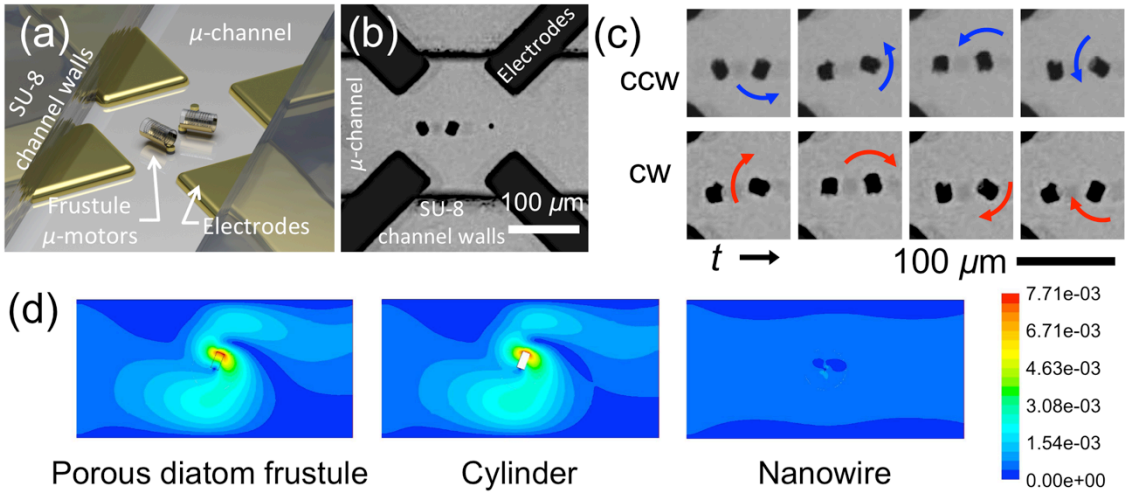

Figure 5.6. (a) An illustration and (b) a micrograph of an array of diatom frustule motors integrated into a microfluidic channel. (c) Simultaneous rotation of diatom frustule motors in a microfluidic channel ccw and cw. (d) Simulation results of the flow around a rotating diatom frustule motor, cylindrical microstructure, and nanowire in a microfluidic channel.

5.4. CONCLUSION

In summary, we reported assembly and actuation of bioinspired micromotors composed of diatom frustule rotors and patterned micromagnets for microfluidic applications. Both pure and metal-coated diatom frustules were successfully manipulated by the electric tweezers and they were precisely positioned and assembled on predefined micromagnets. A diatom frustule motor was rotated continuously for ~11.5 minutes and reached its maximum speed of ~2850 rpm. We explored the characteristics of diatom frustule motors and found metal-coated diatom frustules changed the rotation direction depending on the frequency of the AC **E**-field, unlike pure diatom frustules. Diatom frustule micromotors were integrated with microfluidic channels and multiple diatom motors were rotated in an ordered array. Simulation results showed that the diatom

frustules could stir the surrounding fluid more efficiently than nanowires due to the larger dimensions as well as the embedded porous three-dimensional nanostructures. This work is the first report of the diatom frustule motors to the best of our knowledge and could be promising for biochemical sensing and microfluidic mixing and pumping.

Chapter 6: Conclusions

6.1. SUMMARY

In this dissertation, we reported innovative designs and mechanisms for the fabrication and actuation of rotary MEMS/NEMS devices assembled from nanoscale components using the electric tweezers and magnetic interactions among micro/nanoentities. The dynamics of the devices including mechanical, electric, and magnetic interactions in nanoscale systems were investigated and their translational and rotational motions such as controllability, speed, and lifetime were characterized. Based on the findings and understandings of the devices, we could improve their performance and reliability and demonstrated their use for biomedical and microfluidic applications.

In chapter 2, arrays of nanowire NEMS devices were precisely assembled and synchronously oscillated between two designated angular positions for over 4000 cycles based on unique magnetic interactions between nanoentities with perpendicular magnetic anisotropy (PMA) and the electric tweezers. Quantitative analysis of the dynamics of torque involved in the nano-oscillators revealed that the induced electrostatic torque due to the external **E**-fields between metallic NEMS components play a significant role in the mechanical actuation.

In chapter 3, we described the design, assembly and rotation of ordered arrays of nanomotors. The nanomotors were bottom-up assembled from nanoscale building blocks with nanowires as rotors, patterned nanomagnets as bearings and quadrupole microelectrodes as stators. Arrays of nanomotors were rotated with controlled angle, speed (over 18,000 rpm), and chirality by **E**-fields. Using analytical modeling, we revealed the fundamental nanoscale electrical, mechanical and magnetic interactions in

the nanomotor system, which agreed to a large extent with experimental results and provided critical understanding for designing metallic nanoelectromechanical systems. The nanomotors continuously rotated for 15 hours, which equals over 240,000 cycles. They were applied to controlled biochemical release and demonstrated releasing rate of biochemical from the nanomotors could be precisely tuned by mechanical rotations.

In chapter 4, we investigated the rotation dynamics of the rotary micromotors by tuning the magnetic interactions among the assembled micro/nanoscale components in order to produce desired performance. It was found that the magnetic forces for anchoring the rotors on the bearings played an essential role in the rotation dynamics of the micromotors. By varying the moment, orientation, and dimension of the magnetic components, distinct rotation behaviors could be observed, including repeatable wobbling and rolling in addition to rotation. Through understanding of the rotation behaviors by analytical modeling, we designed and developed micromotors with step-motor characteristics.

In chapter 5, bioinspired micromotors composed of diatom frustule rotors and patterned micromagnets were magnetically assembled. Both pure and metal-coated diatom frustules were successfully manipulated by the electric tweezers and their linear and rotational motion under **E**-fields were characterized. Diatom frustule micromotors were integrated with microfluidic channels and multiple devices could be rotated simultaneously. Simulation results showed that diatom frustules could interact with the surrounding fluid more efficiently than nanowires because of the large dimensions and the porous three-dimensional structures, which indicate diatom frustule motors would be promising for microfluidic actuators such as micromixers.

The innovative concepts, device designs, assembling strategies, actuation mechanisms, and applications reported in this dissertation are relevant to MEMS/NEMS,

nanorobotics, biomedical applications, microfluidics and lab-on-a-chip architectures and would inspire and stimulate the development of high-performance nanomachines for applications in the aforementioned areas.

6.2. Future Perspectives

While in the early stage, miniaturized nanomachines were fabricated with top-down lithography approaches, recent technical advances in the synthesis and manipulation of nanoparticles have allowed bottom-up assembling and actuation of nanomachines, which is advantageous for cost-effective and high-rate production. Nanomachines based on diverse working mechanisms have been developed that convert various energy sources into the mechanical motions of synthesized nanoparticles, including optical, electric, magnetic, acoustic tweezers, chemical locomotion, and molecular motor hybridization. Excellent driving power, efficiency, controllability, and unique applications have been demonstrated in some types of nanomachines, suggesting the great potential of this research field in realizing dream nanorobots.

Despite all the progress, there are grand challenges in the further development of complex nanomachines and associated applications. First, most of the aforediscussed nanomachines are freely suspended in liquids and transport or rotate themselves in a 2-D plane without control in the third direction. It is pivotal to manipulate nanoparticles with high precision and controllability in 3-D for the assembling and operation of complex nanomachines.[130] Second, the efforts to assemble nanomachines consisting of multiple functional components just began.[14] It will be interesting to select and integrate various functional components to a nanomachine that can sense, evaluate, and actuate with intelligence. To achieve this, different transduction mechanisms that convert external

stimuli, e.g., presence of biochemicals of interest, into efficient mechanical actuation should be studied. The assembling principles that attach various components with selectivity and stereo-control are pivotal. Third, the issues of the biocompatibility and reliability of nanomachines operating *in vitro* and *in vivo* should be addressed, i.e., how to achieve high-power micro/nanomachines that can sense, move to infected tissues after passing through various barriers, operate, and leave without residual or side effects. Forth, the synchronous operation of a large number of nanomachines with the ability to control individual machines is extremely important for practical applications, i.e., it will be useful that billions of nanomotors can actively seek targets, separate them from the surroundings, and taking them to prescribed locations. This is a dire need for high throughput biochemical purification and environmental protections. It can be envisioned that the combination of the various tweezers with unique advantages could bring the success of nanomachines to the next level. Nanomachines could have a huge impact to people's lives with continuous successful progress.

References

(1) Feynman, R. P. There's Plenty of Room at the Bottom. *Engineering and science* **1960**, *23*, 22–36.

(2) Tsunoda, S. P.; Aggeler, R.; Yoshida, M.; Capaldi, R. A. Rotation of the C Subunit Oligomer in Fully Functional F1Fo ATP Synthase. *Proc. Natl. Acad. Sci. U.S.A.* **2001**, *98*, 898–902.

(3) Li, J. J.; Tan, W. A Single DNA Molecule Nanomotor. *Nano Lett.* **2002**, *2*, 315–318.

(4) Cha, T.-G.; Pan, J.; Chen, H.; Salgado, J.; Li, X.; Mao, C.; Choi, J. H. A Synthetic DNA Motor That Transportsnanoparticles Along Carbon Nanotubes. *Nat. Nanotechnol.* **2013**, *9*, 39–43.

(5) Davenport, R. J.; Wuite, G. J. L.; Landick, R.; Bustamante, C. Single-Molecule Study of Transcriptional Pausing and Arrest by E. Coli RNA Polymerase. *Science* **2000**, *287*, 2497–2500.

(6) Sambongi, Y.; Iko, Y.; Tanabe, M.; Omote, H.; Iwamoto-Kihara, A.; Ueda, I.; Yanagida, T.; Wada, Y.; Futai, M. Mechanical Rotation of the C Subunit Oligomer in ATP Synthase (F_0F_1): Direct Observation. *Science* **1999**, *286*, 1722–1724.

(7) Viasnoff, V.; Meller, A.; Isambert, H. DNA Nanomechanical Switches Under Folding Kinetics Control. *Nano Lett.* **2006**, *6*, 101–104.

(8) Cohen, A. E.; Moerner, W. E. Suppressing Brownian Motion of Individual Biomolecules in Solution. *Proc. Natl. Acad. Sci. U.S.A.* **2006**, *103*, 4362–4365.

(9) Soong, R. K.; Bachand, G. D.; Neves, H. P.; Olkhovets, A. G.; Craighead, H. G.; Montemagno, C. D. Powering an Inorganic Nanodevice with a Biomolecular Motor. *Science* **2000**, *290*, 1555–1558.

(10) Tanaka, Y.; Morishima, K.; Shimizu, T.; Kikuchi, A.; Yamato, M.; Okano, T.; Kitamori, T. An Actuated Pump on-Chip Powered by Cultured Cardiomyocytes. *Lab Chip* **2006**, *6*, 362.

(11) Fan, D.; Zhu, F.; Cammarata, R.; Chien, C. Controllable High-Speed Rotation of Nanowires. *Phys. Rev. Lett.* **2005**, *94*, 247208.

(12) Fan, D. L.; Cammarata, R. C.; Chien, C. L. Precision Transport and Assembling of Nanowires in Suspension by Electric Fields. *Appl. Phys. Lett.* **2008**, *92*, 093115.

(13) Fan, D.; Yin, Z.; Cheong, R.; Zhu, F. Q.; Cammarata, R. C.; Chien, C. L.; Levchenko, A. Subcellular-Resolution Delivery of a Cytokine Through Precisely Manipulated Nanowires. *Nat. Nanotechnol.* **2010**, *5*, 545–551.

(14) Kwanohh, K.; Xu, X.; Guo, J.; Fan, D. L. Ultrahigh-Speed Rotating Nanoelectromechanical System Devices Assembled From Nanoscale Building Blocks. *Nat. Commun.* **2014**, *5*, 3632.

(15) Kwanohh, K.; Guo, J.; Xu, X.; Fan, D. E. Micromotors with Step-Motor

Characteristics by Controlled Magnetic Interactions Among Assembled Components. *ACS Nano* **2015**, *9*, 548–554.
(16) Wang, W.; Li, S.; Mair, L.; Ahmed, S.; Huang, T. J.; Mallouk, T. E. Acoustic Propulsion of Nanorod Motors Inside Living Cells. *Angew. Chem. Int. Ed.* **2014**, *53*, 3201–3204.
(17) Ding, X.; Lin, S.-C. S.; Kiraly, B.; Yue, H.; Li, S.; Chiang, I.-K.; Shi, J.; Benkovic, S. J.; Huang, T. J. On-Chip Manipulation of Single Microparticles, Cells, and Organisms Using Surface Acoustic Waves. *Proc. Natl. Acad. Sci. U.S.A.* **2012**, *109*, 11105–11109.
(18) Gao, W.; Sattayasamitsathit, S.; Manesh, K. M.; Weihs, D.; Wang, J. Magnetically Powered Flexible Metal Nanowire Motors. *J. Am. Chem. Soc.* **2010**, *132*, 14403–14405.
(19) Vieira, G.; Henighan, T.; Chen, A.; Hauser, A.; Yang, F.; Chalmers, J.; Sooryakumar, R. Magnetic Wire Traps and Programmable Manipulation of Biological Cells. *Phys. Rev. Lett.* **2009**, *103*, 128101.
(20) Ghosh, A.; Fischer, P. Controlled Propulsion of Artificial Magnetic Nanostructured Propellers. *Nano Lett.* **2009**, *9*, 2243–2245.
(21) Gao, W.; Kagan, D.; Pak, O. S.; Clawson, C.; Campuzano, S.; Chuluun-Erdene, E.; Shipton, E.; Fullerton, E. E.; Zhang, L.; Lauga, E.; *et al*. Cargo-Towing Fuel-Free Magnetic Nanoswimmers for Targeted Drug Delivery. *Small* **2011**, *8*, 460–467.
(22) Ghosh, A.; Paria, D.; Singh, H. J.; Venugopalan, P. L.; Ghosh, A. Dynamical Configurations and Bistability of Helical Nanostructures Under External Torque. *Phys. Rev. E* **2012**, *86*, 031401.
(23) Paxton, W. F.; Kistler, K. C.; Olmeda, C. C.; Sen, A.; St Angelo, S. K.; Cao, Y.; Mallouk, T. E.; Lammert, P. E.; Crespi, V. H. Catalytic Nanomotors: Autonomous Movement of Striped Nanorods. *J. Am. Chem. Soc.* **2004**, *126*, 13424–13431.
(24) Fournier-Bidoz, S.; Arsenault, A. C.; Manners, I.; Ozin, G. A. Synthetic Self-Propelled Nanorotors. *Chem. Commun.* **2005**, 441–443.
(25) Sundararajan, S.; Lammert, P.; Zudans, A.; Crespi, V.; Sen, A. Catalytic Motors for Transport of Colloidal Cargo. *Nano Lett.* **2008**, *8*, 1271–1276.
(26) Kagan, D.; Calvo-Marzal, P.; Balasubramanian, S.; Sattayasamitsathit, S.; Manesh, K.; Flechsig, G.; Wang, J. Chemical Sensing Based on Catalytic Nanomotors: Motion-Based Detection of Trace Silver. *J. Am. Chem. Soc.* **2009**, *131*, 12082–12083.
(27) Valadares, L.; Tao, Y.; Zacharia, N.; Kitaev, V.; Galembeck, F.; Kapral, R.; Ozin, G. Catalytic Nanomotors: Self-Propelled Sphere Dimers. *Small* **2010**, *6*, 565–572.
(28) Gao, W.; Sattayasamitsathit, S.; Orozco, J.; Wang, J. Highly Efficient Catalytic Microengines: Template Electrosynthesis of Polyaniline/Platinum Microtubes. *J. Am. Chem. Soc.* **2011**, *133*, 11862–11864.
(29) Baraban, L.; Makarov, D.; Streubel, R.; Mönch, I.; Grimm, D.; Sanchez, S.;

Schmidt, O. G. Catalytic Janus Motors on Microfluidic Chip: Deterministic Motion for Targeted Cargo Delivery. *ACS Nano* **2012**, *6*, 3383–3389.
(30) Ozin, G. A.; Manners, I.; Fournier-Bidoz, S.; Arsenault, A. Dream Nanomachines. *Adv. Mater.* **2005**, *17*, 3011–3018.
(31) Tai, Y.-C.; Fan, L.-S.; Muller, R. S. IC-Processed Micro-Motors: Design, Technology, and Testing. In; 1989; pp. 1–6.
(32) Tai, Y.-C.; Muller, R. S. IC-Processed Electrostatic Synchronous Micromotors. *Sens. Actuators* **1989**, *20*, 49–55.
(33) Yu-Chong, T.; Muller, R. S. Frictional Study of IC-Processed Micromotors. *Sens. Actuators A* **1990**, *21*, 180–183.
(34) Garcia, E. J.; Sniegowski, J. J. Surface Micromachined Microengine. *Sens. Actuators A* **1995**, *48*, 203–214.
(35) Frechette, L. G.; Nagle, S. F.; Ghodssi, R.; Umans, S. D.; Schmidt, M. A.; Lang, J. H. An Electrostatic Induction Micromotor Supported on Gas-Lubricated Bearings. In; 2001; pp. 290–293.
(36) Frechette, L. G.; Jacobson, S. A.; Breuer, K. S.; Ehrich, F. F.; Ghodssi, R.; Khanna, R.; Wong, C. W.; Zhang, X.; Schmidt, M. A.; Epstein, A. H. High-Speed Microfabricated Silicon Turbomachinery and Fluid Film Bearings. *J. Microelectromech. Syst.* **2005**, *14*, 141–152.
(37) Ghalichechian, N.; Modafe, A.; Beyaz, M. I.; Ghodssi, R. Design, Fabrication, and Characterization of a Rotary Micromotor Supported on Microball Bearings. *J. Microelectromech. Syst.* **2008**, *17*, 632–642.
(38) Raiteri, R.; Grattarola, M.; Butt, H.-J.; Skládal, P. Micromechanical Cantilever-Based Biosensors. *Sens. Actuators B* **2001**, *79*, 115–126.
(39) Lemkin, M.; Boser, B. E. A Three-Axis Micromachined Accelerometer with a CMOS Position-Sense Interface and Digital Offset-Trim Electronics. *IEEE J. Solid-State Circuits* **1999**, *34*, 456–468.
(40) Seshia, A. A.; Palaniapan, M.; Roessig, T. A.; Howe, R. T.; Gooch, R. W.; Schimert, T. R.; Montague, S. A Vacuum Packaged Surface Micromachined Resonant Accelerometer. *J. Microelectromech. Syst.* **2002**, *11*, 784–793.
(41) Bhushan, B. Nanotribology and Nanomechanics of MEMS/NEMS and BioMEMS/BioNEMS Materials and Devices. *Microelectron. Eng.* **2007**, *84*, 387–412.
(42) Xia, Y.; Yang, P.; Sun, Y.; Wu, Y.; Mayers, B.; Gates, B.; Yin, Y.; Kim, F.; Yan, H. One-Dimensional Nanostructures: Synthesis, Characterization, and Applications. *Adv. Mater.* **2003**, *15*, 353–389.
(43) Whitney, T. M.; Searson, P. C.; Jiang, J. S.; Chien, C. L. Fabrication and Magnetic Properties of Arrays of Metallic Nanowires. *Science* **1993**, *261*, 1316–1319.
(44) Fan, D. L.; Zhu, F. Q.; Cammarata, R. C.; Chien, C. L. Manipulation of Nanowires in Suspension by Ac Electric Fields. *Appl. Phys. Lett.* **2004**, *85*, 4175–4177.
(45) Ning, J.; Xu, X.; Liu, C.; Fan, D. L. Three-Dimensional Multilevel Porous Thin

Graphite Nanosuperstructures for Ni(OH) 2-Based Energy Storage Devices. *J. Mater. Chem. A* **2014**, *2*, 15768–15773.
(46) Liu, B.; Zeng, H. C. Hydrothermal Synthesis of ZnO Nanorods in the Diameter Regime of 50 Nm. *J. Am. Chem. Soc.* **2003**, *125*, 4430–4431.
(47) Fan, D. L.; Zhu, F. Q.; Cammarata, R. C.; Chien, C. L. Electric Tweezers. *Nano Today* **2011**, *6*, 339–354.
(48) Cao, G.; Wang, Y. Nanostructures and Nanomaterials: Synthesis, Properties, and Applications; World Scientific: Singapore; London, 2011.
(49) Fan, D. L.; Zhu, F. Q.; Xu, X.; Cammarata, R. C.; Chien, C. L. Electronic Properties of Nanoentities Revealed by Electrically Driven Rotation. *Proc. Natl. Acad. Sci. U.S.A.* **2012**, *109*, 9309–9313.
(50) Ekinci, K. L.; Roukes, M. L. Nanoelectromechanical Systems. *Rev. Sci. Instrum.* **2005**, *76*, 061101.
(51) Roukes, M. Nanoelectromechanical Systems Face the Future. *Physics World* **2001**, *14*, 25–31.
(52) Dan, Y.; Evoy, S.; Johnson, A. T. C. Chemical Gas Sensors Based on Nanowires. *arXiv.org*, 2008, *cond-mat.mtrl-sci*.
(53) Cui, Y. Nanowire Nanosensors for Highly Sensitive and Selective Detection of Biological and Chemical Species. *Science* **2001**, *293*, 1289–1292.
(54) Ranzoni, A.; Schleipen, J. J. H. B.; van IJzendoorn, L. J.; Prins, M. W. J. Frequency-Selective Rotation of Two-Particle Nanoactuators for Rapid and Sensitive Detection of Biomolecules. *Nano Lett.* **2011**, *11*, 2017–2022.
(55) Guerra, D. N.; Bulsara, A. R.; Ditto, W. L.; Sinha, S.; Murali, K.; Mohanty, P. A Noise-Assisted Reprogrammable Nanomechanical Logic Gate. *Nano Lett.* **2010**, *10*, 1168–1171.
(56) Weldon, J. A.; Alemán, B.; Sussman, A.; Gannett, W.; Zettl, A. K. Sustained Mechanical Self-Oscillations in Carbon Nanotubes. *Nano Lett.* **2010**, *10*, 1728–1733.
(57) Feng, X. L.; Matheny, M. H.; Zorman, C. A.; Mehregany, M.; Roukes, M. L. Low Voltage Nanoelectromechanical Switches Based on Silicon Carbide Nanowires. *Nano Lett.* **2010**, *10*, 2891–2896.
(58) Chen, Z.; Tong, L.; Wu, Z.; Liu, Z. Fabrication of Electromechanical Switch Using Interconnected Single-Walled Carbon Nanotubes. *Appl. Phys. Lett.* **2008**, *92*, 103116.
(59) Lee, S. W.; Lee, D. S.; Morjan, R. E.; Jhang, S. H.; Sveningsson, M.; Nerushev, O. A.; Park, Y. W.; Campbell, E. E. B. A Three-Terminal Carbon Nanorelay. *Nano Lett.* **2004**, *4*, 2027–2030.
(60) Fennimore, A. M.; Yuzvinsky, T. D.; Han, W.-Q.; Fuhrer, M. S.; Cumings, J.; Zettl, A. Rotational Actuators Based on Carbon Nanotubes. *Nature* **2003**, *424*, 408–410.
(61) Marini, M.; Piantanida, L.; Musetti, R.; Bek, A.; Dong, M.; Besenbacher, F.; Lazzarino, M.; Firrao, G. A Revertible, Autonomous, Self-Assembled DNA-Origami Nanoactuator. *Nano Lett.* **2011**, *11*, 5449–5454.

(62) Fan, Z.; Ho, J. C.; Jacobson, Z. A.; Yerushalmi, R.; Alley, R. L.; Razavi, H.; Javey, A. Wafer-Scale Assembly of Highly Ordered Semiconductor Nanowire Arrays by Contact Printing. *Nano Lett.* **2008**, *8*, 20–25.
(63) Yu, G.; Cao, A.; Lieber, C. M. Large-Area Blown Bubble Films of Aligned Nanowires and Carbon Nanotubes. *Nat. Nanotechnol.* **2007**, *2*, 372–377.
(64) Huang, Y. Directed Assembly of One-Dimensional Nanostructures Into Functional Networks. *Science* **2001**, *291*, 630–633.
(65) Huang, Y.; Duan, X.; Lieber, C. M. Nanowires for Integrated Multicolor Nanophotonics. *Small* **2005**, *1*, 142–147.
(66) Freer, E. M.; Grachev, O.; Duan, X.; Martin, S.; Stumbo, D. P. High-Yield Self-Limiting Single-Nanowire Assembly with Dielectrophoresis. *Nat. Nanotechnol.* **2010**, *5*, 525–530.
(67) Raychaudhuri, S.; Dayeh, S. A.; Wang, D.; Yu, E. T. Precise Semiconductor Nanowire Placement Through Dielectrophoresis. *Nano Lett.* **2009**, *9*, 2260–2266.
(68) Li, M.; Bhiladvala, R. B.; Morrow, T. J.; Sioss, J. A.; Lew, K.-K.; Redwing, J. M.; Keating, C. D.; Mayer, T. S. Bottom-Up Assembly of Large-Area Nanowire Resonator Arrays. *Nat. Nanotechnol.* **2008**, *3*, 88–92.
(69) Vijayaraghavan, A.; Blatt, S.; Weissenberger, D.; Oron-Carl, M.; Hennrich, F.; Gerthsen, D.; Hahn, H.; Krupke, R. Ultra-Large-Scale Directed Assembly of Single-Walled Carbon Nanotube Devices. *Nano Lett.* **2007**, *7*, 1556–1560.
(70) Liu, Y.; Chung, J.-H.; Liu, W. K.; Ruoff, R. S. Dielectrophoretic Assembly of Nanowires. *J. Phys. Chem. B* **2006**, *110*, 14098–14106.
(71) Harnack, O.; Pacholski, C.; Weller, H.; Yasuda, A.; Wessels, J. M. Rectifying Behavior of Electrically Aligned ZnO Nanorods. *Nano Lett.* **2003**, *3*, 1097–1101.
(72) Smith, P. A.; Nordquist, C. D.; Jackson, T. N.; Mayer, T. S.; Martin, B. R.; Mbindyo, J.; Mallouk, T. E. Electric-Field Assisted Assembly and Alignment of Metallic Nanowires. *Appl. Phys. Lett.* **2000**, *77*, 1399–1401.
(73) Duan, X.; Huang, Y.; Cui, Y.; Wang, J.; Lieber, C. Indium Phosphide Nanowires as Building Blocks for Nanoscale Electronic and Optoelectronic Devices. *Nature* **2001**, *409*, 66–69.
(74) Liu, M.; Lagdani, J.; Imrane, H.; Pettiford, C.; Lou, J.; Yoon, S.; Harris, V. G.; Vittoria, C.; Sun, N. X. Self-Assembled Magnetic Nanowire Arrays. *Appl. Phys. Lett.* **2007**, *90*, 103105.
(75) Hangarter, C. M.; Myung, N. V. Magnetic Alignment of Nanowires. *Chem. Mater.* **2005**, *17*, 1320–1324.
(76) Bentley, A. K.; Trethewey, J. S.; Ellis, A. B.; Crone, W. C. Magnetic Manipulation of Copper−Tin Nanowires Capped with Nickel Ends. *Nano Lett.* **2004**, *4*, 487–490.
(77) Coey, J. M. D. Magnetism and Magnetic Materials; Cambridge University Press: Dublin, 2010.
(78) Xu, X.; Kwanohh, K.; Li, H.; Fan, D. L. Ordered Arrays of Raman

Nanosensors for Ultrasensitive and Location Predictable Biochemical Detection. *Adv. Mater.* **2012**, *24*, 5457–5463.
(79) Lee, S. H.; Zhu, F.; Chien, C.; Marković, N. Effect of Geometry on Magnetic Domain Structure in Ni Wires with Perpendicular Anisotropy: a Magnetic Force Microscopy Study. *Phys. Rev. B* **2008**, *77*, 132408.
(80) Zhu, L.; Chen, T.; Chien, C. Altering the Superconductor Transition Temperature by Domain-Wall Arrangements in Hybrid Ferromagnet-Superconductor Structures. *Phys. Rev. Lett.* **2008**, *101*, 017004.
(81) Keshoju, K.; Xing, H.; Sun, L. Magnetic Field Driven Nanowire Rotation in Suspension. *Appl. Phys. Lett.* **2007**, *91*, 123114.
(82) Jones, T. B. Electromechanics of Particles; Cambridge University Press: Cambridge; New York, 1995.
(83) Miller, R. D.; Jones, T. B. Electro-Orientation of Ellipsoidal Erythrocytes. Theory and Experiment. *Biophys. J.* **1993**, *64*, 1588–1595.
(84) Ibach, H.; Lüth, H. Solid-State Physics: an Introduction to Principles of Materials Science; 4 ed.; Springer, 2009.
(85) Douglas, S. M.; Bachelet, I.; Church, G. M. A Logic-Gated Nanorobot for Targeted Transport of Molecular Payloads. *Science* **2012**, *335*, 831–834.
(86) Lakowicz, J. R. Plasmonics in Biology and Plasmon-Controlled Fluorescence. *Plasmonics* **2006**, *1*, 5–33.
(87) Carrara, S. Nano-Bio-Technology and Sensing Chips: New Systems for Detection in Personalized Therapies and Cell Biology. *Sensors* **2010**, *10*, 526–543.
(88) Gao, J.; Gu, H.; Xu, B. Multifunctional Magnetic Nanoparticles: Design, Synthesis, and Biomedical Applications. *Acc. Chem. Res.* **2009**, *42*, 1097–1107.
(89) Razeghi, M.; Rogalski, A. Semiconductor Ultraviolet Detectors. *J. Appl. Phys.* **1996**, *79*, 7433–7473.
(90) Jin, Y.; Wang, J.; Sun, B.; Blakesley, J. C.; Greenham, N. C. Solution-Processed Ultraviolet Photodetectors Based on Colloidal ZnO Nanoparticles. *Nano Lett.* **2008**, *8*, 1649–1653.
(91) Judy, J. W. Microelectromechanical Systems (MEMS): Fabrication, Design and Applications. *Smart Mater. Struct.* **2001**, *10*, 1115–1134.
(92) Tribology Issues and Opportunities in MEMS; Bhushan, B., Ed.; Kluwer Academic Publishers: Dordrecht; Boston, 1998.
(93) Yuzvinsky, T. D.; Fennimore, A. M.; Kis, A.; Zettl, A. Controlled Placement of Highly Aligned Carbon Nanotubes for the Manufacture of Arrays of Nanoscale Torsional Actuators. *Nanotechnology* **2006**, *17*, 434–438.
(94) Kline, T. R.; Paxton, W. F.; Mallouk, T. E.; Sen, A. Catalytic Nanomotors: Remote-Controlled Autonomous Movement of Striped Metallic Nanorods. *Angew. Chem. Int. Ed.* **2005**, *44*, 744–746.
(95) Sundararajan, S.; Sengupta, S.; Ibele, M.; Sen, A. Drop-Off of Colloidal Cargo Transported by Catalytic Pt–Au Nanomotors via Photochemical Stimuli. *Small*

2010, *6*, 1479–1482.
(96) Wang, J. Cargo-Towing Synthetic Nanomachines: Towards Active Transport in Microchip Devices. *Lab Chip* **2012**, *12*, 1944–1950.
(97) He, Y.; Wu, J.; Zhao, Y. Designing Catalytic Nanomotors by Dynamic Shadowing Growth. *Nano Lett*. **2007**, *7*, 1369–1375.
(98) Purcell, E. M. Life at Low Reynolds Number. *Am. J. Phys*. **1977**, *45*, 3–11.
(99) De Mestre, N. J. Low-Reynolds-Number Fall of Slender Cylinders Near Boundaries. *J. Fluid Mech*. **1973**, *58*, 641–656.
(100) Xu, X.; Li, H.; Hasan, D.; Ruoff, R. S.; Wang, A. X.; Fan, D. L. Near-Field Enhanced Plasmonic-Magnetic Bifunctional Nanotubes for Single Cell Bioanalysis. *Adv. Funct. Mater*. **2013**, *23*, 4332–4338.
(101) Peiris, P. M.; Bauer, L.; Toy, R.; Tran, E.; Pansky, J.; Doolittle, E.; Schmidt, E.; Hayden, E.; Mayer, A.; Keri, R. A.; *et al*. Enhanced Delivery of Chemotherapy to Tumors Using a Multicomponent Nanochain with Radio-Frequency-Tunable Drug Release. *ACS Nano* **2012**, *6*, 4157–4168.
(102) Gao, X.; Cui, Y.; Levenson, R. M.; Chung, L. W. K.; Nie, S. In Vivo Cancer Targeting and Imaging with Semiconductor Quantum Dots. *Nat. Biotechnol*. **2004**, *22*, 969–976.
(103) Lee, J. O.; Song, Y.-H.; Kim, M.-W.; Kang, M.-H.; Oh, J.-S.; Yang, H.-H.; Yoon, J.-B. A Sub-1-Volt Nanoelectromechanical Switching Device. *Nat. Nanotechnol*. **2013**, *8*, 36–40.
(104) Li, M.; Tang, H. X.; Roukes, M. L. Ultra-Sensitive NEMS-Based Cantilevers for Sensing, Scanned Probe and Very High-Frequency Applications. *Nat. Nanotechnol*. **2007**, *2*, 114–120.
(105) Hanay, M. S.; Kelber, S.; Naik, A. K.; Chi, D.; Hentz, S.; Bullard, E. C.; Colinet, E.; Duraffourg, L.; Roukes, M. L. Single-Protein Nanomechanical Mass Spectrometry in Real Time. *Nat. Nanotechnol*. **2012**, *7*, 602–608.
(106) Campuzano, S.; Kagan, D.; Orozco, J.; Wang, J. Motion-Driven Sensing and Biosensing Using Electrochemically Propelled Nanomotors. *Analyst* **2011**, *136*, 4621–4630.
(107) Guix, M.; Mayorga-Martinez, C. C.; Merkoçi, A. Nano/Micromotors in (Bio)Chemical Science Applications. *Chem. Rev*. **2014**, *114*, 6285–6322.
(108) Wang, W.; Duan, W.; Ahmed, S.; Mallouk, T. E.; Sen, A. Small Power: Autonomous Nano- and Micromotors Propelled by Self-Generated Gradients. *Nano Today* **2013**, *8*, 531–554.
(109) Xu, X.; Liu, C.; Kwanohh, K.; Fan, D. L. Electric-Driven Rotation of Silicon Nanowires and Silicon Nanowire Motors. *Adv. Funct. Mater*. **2014**, *24*, 4843–4850.
(110) Xu, X.; Kwanohh, K.; Fan, D. Tunable Release of Multiplex Biochemicals by Plasmonically Active Rotary Nanomotors. *Angew. Chem. Int. Ed*. **2015**, *54*, 2525–2529.
(111) Fan, D. L.; Kim, K.; Guo, J. Electrode Design and Low-Cost Fabrication Method for Assembling and Actuation of Nanomotors with Ultrahigh and

Uniform Speed. Provisional International Patent Application 62047969, 2014.
(112) Kwanohh, K.; Zhu, F. Q.; Fan, D. Innovative Mechanisms for Precision Assembly and Actuation of Arrays of Nanowire Oscillators. *ACS Nano* **2013**, *7*, 3476–3483.
(113) Sun, L.; Hao, Y.; Chien, C. L.; Searson, P. C. Tuning the Properties of Magnetic Nanowires. *IBM J. Res. Dev.* **2005**, *49*, 79–102.
(114) Barthlott, W.; Neinhuis, C. Purity of the Sacred Lotus, or Escape From Contamination in Biological Surfaces. *Planta* **1997**, *202*, 1–8.
(115) Autumn, K.; Liang, Y. A.; Hsieh, S. T.; Zesch, W.; Chan, W. P.; Kenny, T. W.; Fearing, R.; Full, R. J. Adhesive Force of a Single Gecko Foot-Hair. *Nature* **2000**, *405*, 681–685.
(116) Huang, J.; Wang, X.; Wang, Z. L. Controlled Replication of Butterfly Wings for Achieving Tunable Photonic Properties. *Nano Lett.* **2006**, *6*, 2325–2331.
(117) Parker, A. R.; Townley, H. E. Biomimetics of Photonic Nanostructures. *Nat. Nanotechnol.* **2007**, *2*, 347–353.
(118) Gebeshuber, I. C. Biotribology Inspires New Technologies. *Nano Today* **2007**, *2*, 30–37.
(119) Hall, S. R.; Bolger, H.; Mann, S. Morphosynthesis of Complex Inorganic Forms Using Pollen Grain Templates. *Chem. Commun.* **2003**, 2784–2785.
(120) Bessekhouad, Y.; Robert, D.; Weber, J. V. Bi2S3/TiO2 and CdS/TiO2 Heterojunctions as an Available Configuration for Photocatalytic Degradation of Organic Pollutant. *Journal of Photochemistry and Photobiology A: Chemistry* **2004**, *163*, 569–580.
(121) Zhao, Y.; Wei, M.; Lu, J.; Wang, Z. L.; Duan, X. Biotemplated Hierarchical Nanostructure of Layered Double Hydroxides with Improved Photocatalysis Performance. *ACS Nano* **2009**, *3*, 4009–4016.
(122) Kamata, K.; Suzuki, S.; Ohtsuka, M.; Nakagawa, M.; Iyoda, T.; Yamada, A. Fabrication of Left-Handed Metal Microcoil From Spiral Vessel of Vascular Plant. *Adv. Mater.* **2011**, *23*, 5509–5513.
(123) Gao, W.; Feng, X.; Pei, A.; Kane, C. R.; Tam, R.; Hennessy, C.; Wang, J. Bioinspired Helical Microswimmers Based on Vascular Plants. *Nano Lett.* **2014**, *14*, 305–310.
(124) Bao, Z.; Weatherspoon, M. R.; Shian, S.; Cai, Y.; Graham, P. D.; Allan, S. M.; Ahmad, G.; Dickerson, M. B.; Church, B. C.; Kang, Z.; *et al*. Chemical Reduction of Three-Dimensional Silica Micro-Assemblies Into Microporous Silicon Replicas. *Nature* **2007**, *446*, 172–175.
(125) Yang, W.; Lopez, P. J.; Rosengarten, G. Diatoms: Self Assembled Silica Nanostructures, and Templates for Bio/Chemical Sensors and Biomimetic Membranes. *Analyst* **2011**, *136*, 42–53.
(126) Losic, D.; Mitchell, J. G.; Voelcker, N. H. Diatomaceous Lessons in Nanotechnology and Advanced Materials. *Adv. Mater.* **2009**, *21*, 2947–2958.
(127) Gordon, R.; Losic, D.; Tiffany, M. A.; Nagy, S. S.; Sterrenburg, F. A. S. The Glass Menagerie: Diatoms for Novel Applications in Nanotechnology. *Trends*

Biotechnol. **2009**, *27*, 116–127.
(128) Chandrasekaran, S.; Sweetman, M. J.; Kant, K.; Skinner, W.; Losic, D.; Nann, T.; Voelcker, N. H. Silicon Diatom Frustules as Nanostructured Photoelectrodes. *Chem*. *Commun*. **2014**, *50*, 10441–10444.
(129) Townley, H. E.; Parker, A. R.; White-Cooper, H. Exploitation of Diatom Frustules for Nanotechnology: Tethering Active Biomolecules. *Adv*. *Funct*. *Mater*. **2008**, *18*, 369–374.
(130) Pauzauskie, P. J.; Radenovic, A.; Trepagnier, E.; Shroff, H.; Yang, P.; Liphardt, J. Optical Trapping and Integration of Semiconductor Nanowire Assemblies in Water. *Nat*. *Mater*. **2006**, *5*, 97–101.

Vita

Kwanoh Kim was born in Seoul, South Korea. He received his B.S. and M.S. in Mechanical Engineering from Yonsei University, South Korea in 2007 and 2009, respectively. He worked on the synthesis of GaN nanowires and their applications in gas sensing and published 1 co-first authored and 2 co-authored papers during his Master's program. He joined Prof. Donglei Fan's group in the Department of Mechanical Engineering at the University of Texas at Austin for Ph.D. studies in 2010. His research includes design and fabrication of MEMS/NEMS, nanoactuators, nanomotors, microfluidics, and nanomaterials. He has 4 first/co-first authored and 6 co-authored papers published or accepted for publication in high impact journals including Nature Communications, ACS Nano, Advanced Materials, Angewandte Chemie International Edition, Advanced Functional Materials, Small, Nanoscale, and Applied Physics Letters; 2 first authored papers in preparation; 1 book chapter under review; and 1 patent pending since joining Prof. Fan's group. He received a number of awards on various levels including AFOSR Travel Awards for the MRS Meeting, Graduate Student Professional Development Awards (UT Austin), Nano Portfolio Program Travel Awards (UT Austin), Research Poster Contest Awards in the Department of Mechanical Engineering (UT Austin), and NSF Travel Award for the ASME IMECE 2012 Student Poster Symposium.